Probabilistic labelling for enhancement of vessel networks applied to retinal images

Daniel Alonso Paredes Soto

A thesis submitted for the degree of

Doctor of Philosophy

The University of Sheffield

Electronic and Electrical Engineering

March 2016

To my children

Pablo Nicolás & Freya Amandine

Declaration

Parts of this thesis has been included in the following published paper:

D. P. Soto, P. Chan, and P. Rockett. "Performance comparison of low-level vessel detection algorithms for segmentation of X-ray angiograms". In Xianghua Xie, editor, Proceedings of the 16th Conference on Medical Image Understanding and Analysis, pages 173–178, Swansea, United Kingdom, 2012.

Acknowledgements

I would like to express my sincere gratitude to my supervisor Dr Peter I Rockett for his excellent support, encouragement and guidance in both the research and writing of this thesis. I am grateful for his patience and support from the beginning to the completion of this journey. I would like to thank my examiners Dr Abhir Bhalerao and Dr Ali Gooya for their comments and recommendations.

Also, I would like to thank my sponsor the Mexican National Council for Science and Technology (CONACyT) for financial support to pursue my PhD at The University of Sheffield. Without this support this project would not have been possible.

Last finally, but by not means least, thanks go to my wife and children, parents and brothers who have demonstrated infinite support over the last few years; to my parents for their love and guidance through my life; to my wife for sharing and daring to follow my dreams; to my brothers and their families for their unending support. You were all always there in the highs and lows encouraging me to keep going. Very finally, special thanks go to my children for their patience, every little smile and sign of love helped me to carry on especially during difficult times.

Thanks to you all.

Abstract

Occlusive vascular disease affecting arterial circulations is the major and fastest growing health problem worldwide, and underlies common conditions such as heart attack, stroke and peripheral vascular disease. Although vascular diseases may be assessed according to clinical history, screening may be required to evaluate health conditions or courses of treatment. Vasculature in the retina and other organs such as the brain have similar anatomical properties and regulatory mechanisms. Changes in the morphology of retinal vasculature may be associated with vascular-related conditions such as hypertension and stroke. Owing to its high cost-effectiveness, eye fundus photography is often used to study changes in the retinal vasculature.

This research proposes a probabilistic pixel labelling method based on analysis of local and global features of the image to enhance the detail of vessel structures. Our approach produces a probability map that could be further used by contextual approaches (*e.g.* Markov Random Fields) for segmenting vessel networks as future application. We first correct contrast variation due to non-uniform illumination and reflections produced by eye tissue using statistical methods to locally estimate the contrast behind vasculature structures.

Our labelling method is based on the Hessian matrix to locally estimate the maximum probability of the principal local curvature—given by eigenvalues—matching an ideal vessel curvature. We defined a realistic model based on imaging physics to produce the ideal vessel curvature governed by the Beer-Lambert Law for estimating the absorption of energy as it is propagated through uniformly filled objects.

The local maximum posterior probability—based on Bayes' rule—was eventually estimated by combining the *prior* (using the proposed background estimation) and the *likelihood* produced by Monte Carlo simulations. The proposed method in this research was compared with one of the most popular vessel detectors due to Frangi showing similar results.

Contents

List of figures

List of tables

Notation

Greek Symbols

λ	Eigenvalue
σ	Standard deviation

Abbreviations and Acronyms

AMD	Age-related Macular Degeneration
ANN	Artificial Neural Network
AUC	Area Under the Curve
DRIVE	Digital Retinal Images for Vessel Extraction
FA	Fluorescein Angiography
FOV	Field of View
FPR	False Positive Rate
GMM	Gaussian Mixture Model
ICGA	Indocyanine Green Angiography
JPEG	Joint Photographic Experts Group
LLS	Linear Least Squares
LMS	Least Median Squares
LoG	Laplacian of Gaussian
LS	Least Squares
LTC	Long-Term Condition
MMSE	Minimum Median Squared Error
MRA	Magnetic Resonance Angiogram
MRI	Magnetic Resonance Imaging
NHS	National Health Service

NICE	National Institute of Health and Clinical Excellence
OCT	Optical Coherence Tomography
PDF	Probability Density Function
PET	Positron Emission Tomography
PVD	Peripheral Vascular Disease
RANSAC	RANdom SAmple Concensus
ROC	Receiver Operating Characteristic
RoI	Region of Interest
SNR	Signal to Noise Ratio
SSE	Sum of Squared Errors
SVD	Singular Value Decomposition
SVM	Support Vector Machines
TIFF	Tagged Image File Format
TPR	True Positive Rate

Chapter 1
Introduction

Occlusive vascular disease affecting arterial circulations is the major and fastest growing health problem worldwide, and remains as the most important causes of death in industrialised societies. Occlusive vascular disease underlies common conditions such as heart attack, stroke and peripheral vascular disease (PVD).

The World Health Organisation estimates that these diseases were responsible for 17.3 million deaths worldwide in 2008, forecast to rise to 23.6 million in 2030. The National Institute of Health and Clinical Excellence of the United Kingdom (NICE) estimates more than 5 million people in the UK are living with either heart attack or stroke disease. The British Heart Foundation estimates that around 111,000 people have a stroke for the first time every year (2010) [81].

According to the Department of Health, more than 20 million people in the UK suffer at least one Long-Term Condition (LTC) [22]. Due to an ageing population, it is estimated that by 2043 the number of people in England suffering at least one LTC will increase by 23%, particularly the number of those people with more than one condition at once [21]. The World Health Organisation defines a long-term condition as a health problem that cannot, at present, be cured but can be controlled by medication and other treatment or therapies. Long-term conditions include a wide range of health

problems including physical, mental or emotional. In the UK for instance, vascular-related diseases such as hypertension, coronary heart disease and stroke are among the ten main prevalent long-term conditions [21]. Besides, other long-term conditions such as Age-related Macular Degeneration (AMD), diabetic retinopathy and glaucoma are estimated to be among the main causes of partial sight loss and blindness in developed and industrialised countries as the UK [10, 11, 88] and set to rise in the forthcoming years [1, 13, 57, 80, 88].

Occlusion of arteries is naturally compensated, to some extent, by the development of minor channels to carry blood around the occlusion, termed collateral circulation [12, 50, 71, 98, 123]. Formation of new channels around occlusions, changes in calibre of vessels and anatomical changes in vessel networks can be used as markers of vascular diseases. Analysis of retinal vessels in the fundus of eye can provide signs of eye-related conditions, some of which are responsible for sight loss, and systemic diseases including arteriosclerosis, hypertension, diabetic retinopathy, leukemic retinopathy, macular degeneration and retinal vasculitis [1, 2, 24, 45, 92].

Currently the success of vascular condition-related treatments is judged on clinical endpoints like improved exercise ability or fewer amputations; such endpoints are massively confounded by other variables apart from blood flow changes. Moreover, access to supervised exercise programmes is variable and many are not provided by health systems.

The economic impact of long-term conditions including vascular and sight loss-related conditions play an important role for both health and social systems due to the high costs that primary and secondary care represents. Clinic appointments, imaging, therapy, surgery and benefits are some of these services where governments spend money every year. Informal care and productivity losses are another important aspect affecting the economies of countries. For instance, it is estimated that people with an LTC account for the 50% of all GP appointments every year in the UK [22] and to mention an economic impact, cardiovascular disease alone costs to the National Health Service (NHS) and UK economy £30 billion every year [74].

The Department of Health estimates the average cost of health and care for people with at least one LTC to be three times the cost of those people with no LTC [22].

Moreover, people with one LTC are prone to develop more LTC conditions increasing health and care costs [22].

Although assessment of vascular diseases may be carried out through clinical history, screening may be required for the identification and evaluation of vascular-related health conditions or evaluate courses of treatment. Treatment of vascular dementia and stroke for instance, may require an assessment of the cerebral vasculature. Positron Emission Tomography (PET) and Magnetic Resonance Imaging (MRI) are some of the imaging techniques actually used that produce an advanced understanding of the vasculature system. Nonetheless, these scan modalities are often expensive and not be available in all hospitals. The cost of a PET scan in the UK is estimated being around £1,000 (2007) [18].

The brain and retina have similar anatomical vasculature properties and vascular regulatory process. Hence, changes in the retinal vessel network may mirror similar changes in the brain vessel network [90]. Also, changes in the retinal vasculature has been shown to be associated with long-term conditions such as hypertension and stroke [5, 6, 47, 83, 99, 118].

Retinal photography—also known as eye fundus imaging—is a non-invasive technique that allow the visualisation of retinal vasculature *in vivo*. The use of retinal digital image analysis offers methods to analyse the appearance of the vessel network and other objects in the eye. Abnormalities in the retinal vasculature can be interpreted as markers of vascular pathologies while eye-related pathologies such as AMD and diabetic retinopathy can also be studied by analysing the fundus of the eye.

An eye fundus image can be described as a representation of the eye vessel network projected onto a plane. Due to the nature of tissue of the objects involved, images are usually obtained from reflected light beams from the back of the eye, where the intensity captured by a camera sensor represents the intensity of light beams which cross a set of layered soft tissues twice, producing a 2D image representation of the eye.

Eye fundus cameras, also known as ophthalmoscopes, are widely used to photograph the back of the eye since it is less invasive and a highly cost-effective method [1]. Other image representations can be obtained using other techniques, such as fluorescein angiography (FA) and Optical Coherence Tomography (OCT) [27, 117], involving

the injection of a contrast compound into the arterial system to increase the contrast of objects of interest, offering more reliable data. The nature of the fundus camera imaging technique may produce loss of data due to problems presented in the hardware such as noise added by the camera and problems in the photographed environment such as light reflection and scattering due to properties of ocular tissues. In addition, image compression methods used to digitise images plays an important role in preserving a good quality of images.

Screening is usually evaluated by anatomical measurements of a vessel network including collateral beds leading to diagnoses of some long term conditions and eye-related health problems. Quantifying the properties of the networks is difficult due to the tortuosity of affected vessels, complexity of the collateral bed, diameter of these vessels, and the imaging technique used. Usually, labelling and diagnosis of screening is carried ut manually, which is laborious and error prone.

In this thesis a vessel pixel labelling method based on a probabilistic approach is proposed. The method has four stages. Firstly, due to the uneven light intensity across a retinal image, the background of the image is estimated using statistical models. In the proposed model, vessel pixels are regarded as undesired objects while background pixels are the target. Approaches such as Xu *et al.* [119] estimate the background by using a mean filter with a kernel size large enough to remove the vasculature components; Wang *et al.* [114] locally estimate background intensities using a least-squares fitting model. The goal of this first approach is to provide a crude vessel segmentation allowing a prior vessel probability estimation and normalisation of the image.

Secondly, using the estimated intensity of the background, the image is normalised to compensate for changes in the contrast across the image. Feature extraction is carried out using the produced image. Methods such as line detectors and multi-scale representation were employed to cope with segmentation of vessels at a range of diameters.

Thirdly, a probabilistic method, based on Bayes' rule and Monte Carlo simulations—to estimate vessel and background likelihood information—were used to estimate the local maximum posterior probability of a pixel being a true vessel pixel. Here, a true vessel pixel was taken as a pixel with the maximum *vessel-ness* response that naturally occurs along the centreline of a vessel structure. Synthetic images were

used to model an ideal maximum *vessel-ness* response. Finally, the proposed method was evaluated and compared with one of most popular vessel segmentation algorithms (Frangi *et. al* [35]) using a Receiver Operating Characteristic (ROC) and Area Under Curve (AUC) plots.

1.1 Outline of thesis

In Chapter 2, a literature review is presented including topics related to feature extraction to enhance vessel pixels in medical images. Three of the most popular vessel-detection algorithms and their *vessel-ness* measures are described. In order to compare the performance of the selected segmentation algorithms, a method to construct synthetic vessel images is developed based on the physics of image formation. DRIVE [110] (*Digital Retinal Images for Vessel Extraction*), a public retinal-image database much used for the probabilistic labelling method proposed is described. In Chapter 3, an assessment of the selected vessel detection algorithms is presented using a set of synthetic data. This analysis was published in the MIUA 2012 Conference [109].

Chapter 4 and Chapter 5 describe the probabilistic pixel-labelling method proposed to enhance vessel pixels in retinal images. The proposed method comprises two stages: firstly, a background extraction approach is proposed in Chapter 4. The method is based on Least Median Squares (LMS) to estimate the intensity of pixels behind vessel structures producing a vessel segmentation approach. Secondly, a probabilistic labelling approach is proposed in Chapter 5. Estimation of the posterior probability of a pixel being a vessel object is based on Bayes' rule. Receiver Operating Characteristic (ROC) and its Area Under Curve (AUC) were used to measure the performance of the proposed approach.

Conclusions, discussion and future work are outlined in Chapter 6.

Chapter 2
Review of Literature

2.1 Introduction

Relevant material surrounding medical image analysis, especially those focused on vessel networks detection, is reviewed in this chapter. This research is focused on pixel-labelling based on enhancement of local features to distinguish blood-vessel-pixels from background in retinal images. In order to do so, vessel structures can be regarded as line-like objects contained in 2D retinal images, or tube-like objects in volumetric data such as Magnetic Resonance Imaging (MRI) dataset.

This chapter is composed of six areas covering topics related to the enhancement of vessel structures in 2D images for the proposed pixel-labelling method based on a probabilistic approach; the latter is developed in Chapter 5.

- **Eye fundus imaging modalities and image formation process.** Imaging modalities used in clinical practice for either the purpose of diagnosis or measuring drug-treatment improvements were studied. In addition, the image formation process in imaging devices is reviewed to develop synthetic images used in Chapter 3.

- **Challenges: illumination, unwanted and phantom objects.** Description of some—probably the most common—problems making vessel segmentation in eye fundus images difficult are reviewed. The aim of this study was understanding image processing algorithms that can deliver unexpected results due to the content of images. In that case, additional pre-processing work may need to be carried out to overcome those unwanted results.
- **Taxonomy of blood vessel presentations.** A classification of wanted objects—vessel structures—is outlined to study local features that can enhance better vessel-pixels from the background.
- **Scale-space theory.** Object detection can be associated with an image resolution. Nonetheless, vessel structures can appear at a range of diameters in retinal images. The scale-space theory—introduced by Lindeberg [64]—was studied to develop the proposed vessel-pixel labelling method capable of detecting vessel structures at a range of sizes using a defined set of local features.
- **Descriptors.** Vessel networks can be regarded as line-like structures in retinal images due to the difference in contrast between the interesting structures and background pixels. Line-detector algorithms were studied, allowing enhancement of local properties of pixels making vessel-pixels distinguishable from the background.
- **'Vesselness' measure.** Previously published vessel detector algorithms and their principles were studied to compare their performance with the proposed probabilistic labelling method.

2.2 Eye fundus imaging

Analysis of the eye fundus has been developed in the last two centuries with the invention of the ophthalmoscope in 1851 by von Helmholtz [51, 91]. In the 1920's, fundus photography was introduced and since then, it has been used to analyse structure of components at the back of the eye [42]. The technologies which emerged have allowed the use of digital photography to capture eye fundus images based on an optical system model making eye fundus analysis more efficient.

In the most basic form, an optical system is formed by a source of light, a subject, a lens and a sensor. Reflected light beams from the surface of an object are refracted by the lens and then captured by the sensor which eventually can represent signals as an image. Figure 2.1 shows the anatomy of the eye and the required elements when an object is observed.

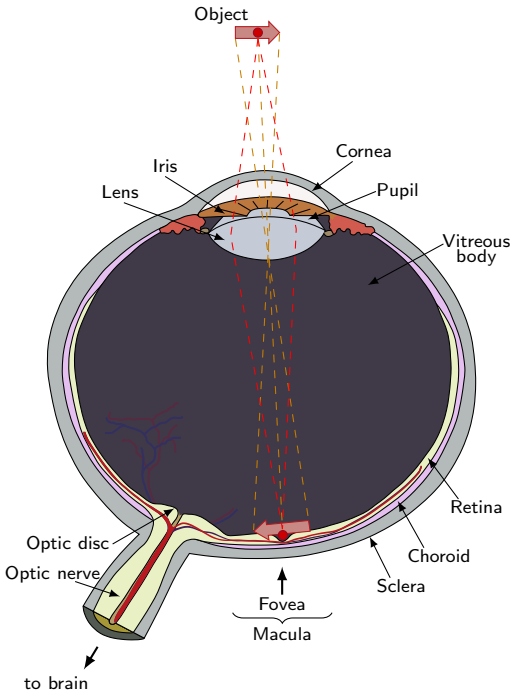

Figure 2.1: Anatomy of the human eye. Light reflected from the object being observed is projected onto the macula of the retina, where the sharpest vision—termed fovea—is found.

In order to photograph the fundus of the eye with a fundus camera, some light is projected onto the back of the eye using the natural eye lens as a gateway between the light source and the target. An amount of light is absorbed and scattered as it crosses the semi-transparent eye tissue. Due to the properties of the back of the eye, light is reflected and sent back through the eye lens. Hence, transmitted light beams can be captured by a sensor—an imaging device—that eventually can convert the beam intensity into an image.

Eye fundus imaging can be regarded as a two-dimensional representation of a three-dimensional phenomenon—retinal tissue and eye components—projected onto a plane. The intensities of pixels in the formed image represent the amount of light crossing the eye tissue twice—as it is reflected by the back wall of the eye—and captured by a sensor similar to X-ray image formation due to energy absorption by tissue.

In addition to the wavelength of light employed, compounds injected into the blood system can be used to enhance objects of interest. Some of the eye fundus imaging techniques currently used are listed below.

- **Colour.** White light is used to illuminate the back of the eye. Three wavelength (red, green and blue—RGB) are used producing a colour image. The image produced quantifies the amount of reflected light in each of the wavebands. The colour of the eye fundus image can be described as lying in the red end of the spectrum due to pigment of the choroid and retina [79] (see Figure 2.2(a)).
- **Red-free.** A filter—commonly green—can be used to suppress the red waveband allowing a better visualisation of details not easily identifiable with the use of white light. Haemoglobin, for instance, absorbs red light, hence haemorrhages can be seen as low-contrast regions [56]. This modality enhances the contrast producing a better resolution of small blood vessels. Enhancement of vessels can be observed in Figure 2.2(b), a photograph captured using a green filter [8].
- **Angiography.** Fluorescein Angiography (FA) and Indocyanine Green Angiography (ICGA) are two angiography imaging modalities used in recent years. The method involves a dye injected into the patient's circulation. Both methods rely on the fact that the compound employed fluoresces in a visible light waveband. In FA for instance, the sodium-based dye used absorbs blue light, the optimal excitation is at 490*nm* and the peak fluorescence occurs at 520*nm* (green colour space).

  In ICGA, activation and reflection of wavelengths takes place near the infrared segment in the spectrum—805*nm* and 835*nm* respectively—[89]. A fundus camera fitted with appropriate lenses can be used to capture the fluorescence of the dye employed as it circulates through the vessel network in the retina. Hence, the intensities of pixels in the formed image represent the number of emitted photons from the dye [1]. FA and ICGA image samples are shown in Figures 2.2(c)-(d) respectively.

Optical Coherence Tomography (OCT), a technique used as a cross-section imaging method, has been used for diagnosis purposes such as diabetic macular degeneration and retinopathy [1]. The principle of OCT is similar to an ultrasound technique

but OCT uses light near the infrared part of the electromagnetic spectrum rather than sound waves to collect information [46, 48]. The principle of OCT is based on low-coherence interferometry [46, 48]—a contactless way to measure reflected light from semi-transparent materials such as the retina. The image produced displays the amount of reflected light using a range of intensities. In coloured images, reflectance is measured at a range from red to green indicating the most and the least reflective tissues and white to black in greyscale imaging. OCT, however, cannot be regarded as eye fundus imaging since it is a cross-sectional view of the eye tissue using reflected light as it crosses layered tissue [1]. Figure 2.3 shows a cross sectional view of eye-tissue layers for analysis of the fovea.

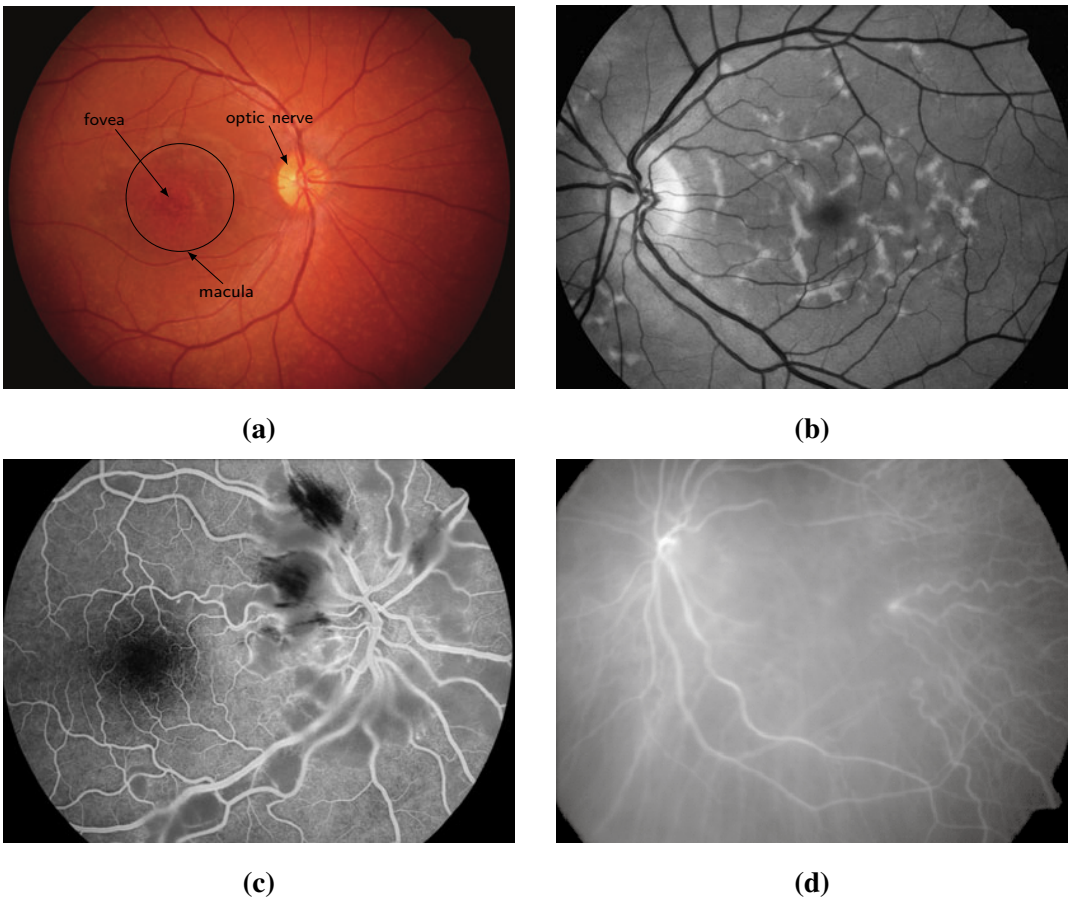

Figure 2.2: Eye fundus imaging samples [8]: (a) Colour eye fundus photography, wide-angle photograph showing the optic nerve, retina and choroid; (b) Red-free eye fundus photography, a green filter (peak transmission at 560*nm*) image illustrates characteristic lesions of Stargardts' disease; (c) Fluorescein Angiography (FA), illustrates vascular filling defects; (d) Indocyanine Green Angiography (ICGA), image captured using infrared illumination showing circulation patterns of the retinal and choroidal vessels.

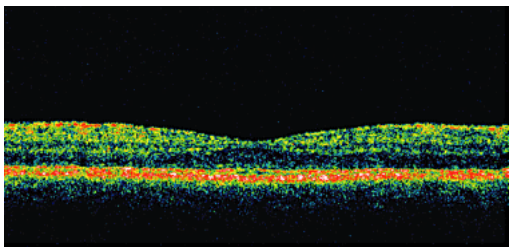

Figure 2.3: Optical Coherence Tomography (OCT) [8]. A cross-sectional view of the normal retinal architecture and foveal depression (colour code: red, high-; black, low-; and green, intermediate reflectivity).

2.2.1 Image formation process

As described in Section 2.2, a fundus camera is usually employed to photograph the back of the eye. This imaging device is formed by a set of lenses making the camera capable of illuminating the back of the eye through the natural eye's lens, and capturing the reflected light beams from the retina producing colour-images. As light beams cross the eye tissue, including the eye's vasculature, they are attenuated due to absorption and scattering properties of tissue. This can be seen as lower contrast in regions where light crosses more layers of tissue.

In Figure 2.4, an eye fundus imaging process is illustrated: the light beams are attenuated as they pass throughout eye tissue twice due to reflection from the back of the eye, and their intensities are captured by an imaging device.

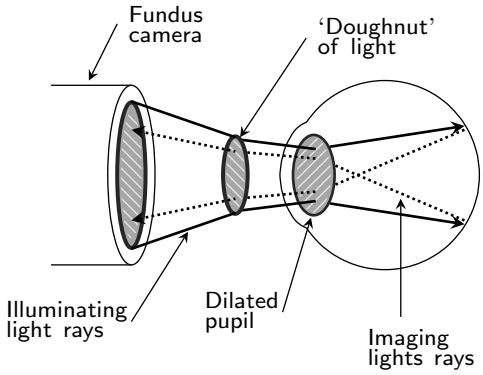

Figure 2.4: The fundus camera projects a 'doughnut' of light through the dilated pupil to illuminate the interior of the eye. These 'illuminating' rays reflect off the retina, and pass back through the centre of the 'doughnut' and into the optical system of the fundus camera. These 'rays' continue back through the fundus camera optics which focuses the image on a film plane [102].

Fundus cameras rely on the principle of indirect ophthalmoscopy. This is a technique where the image being photographed is a virtual image from the retina [93]. The

optics of a fundus camera is formed by two systems: in the first system, an ophthalmoscopic lens—also known as field lens—can be placed either in or out of contact with the cornea to form an image of the fundus, also termed an aerial image; the second system is the camera used to record the aerial image which is eventually converted into a digital format [93].

Prior to capturing a retinal image, the ophthalmoscopic lens is usually adjusted to obtain the best possible image of the eye fundus. The closer the lens to the cornea, the wider the field of view (FOV) of the fundus. Figure 2.5 shows a set up of a fundus camera, where a set of ophthalmoscopic lenses allow a wide FOV due to the arrangement and curvature of the lenses. This allow observation of a larger surface of the retina.

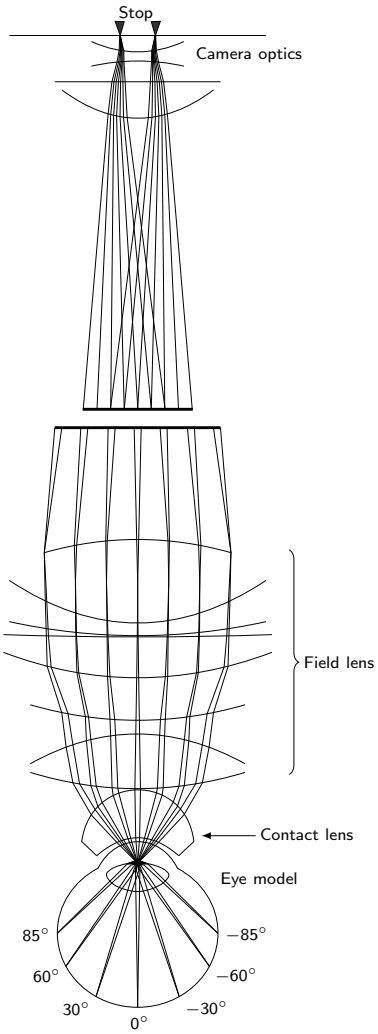

Figure 2.5: Optics of a fundus camera showing a contact lens, field lens and a camera optics system for a field of view (FOV) of 170° measured from the centre of the eye's globe [93]

A typical fundus camera can view between 30° and 50° of the retinal region. An angle of 30°allows a magnification 2.5 times larger than actual measurement. In wide-angle fundus cameras—capturing between 45°and 140°—magnification is reduced proportionately. Similarly, a close angle—typically 20° or less—provides a larger magnification [103]. Figure 2.6 shows a set of retinal images captured with distinct field of view measurements.

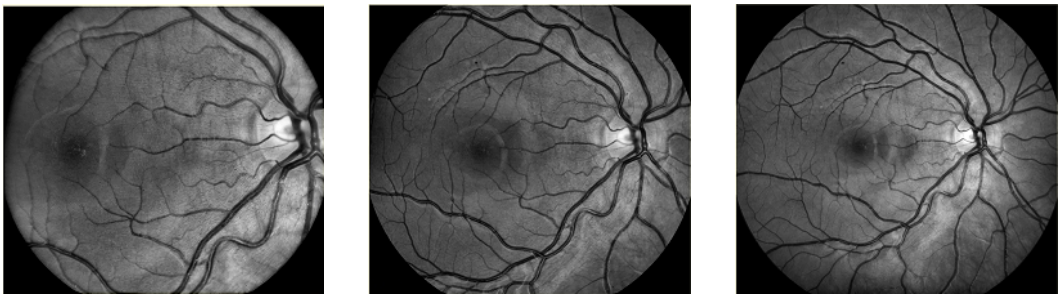

(a) **(b)** **(c)**

Figure 2.6: Image magnification due to the Field of View (FOV) settings in an eye fundus camera: (a) 20°; (b) 40°; and (c) 60° [103].

Since light beams are attenuated as they cross eye tissue, they hit the camera sensor with less intensity producing dark pixels as seen in Figure 2.6. The more tissue light crossings—*e.g.* large vessels and overlapping vessels, the lower the intensity. Conversely, regions with fewer tissue traversals produce brighter pixels. A synthetic image of a single straight vessel is shown in Figure 2.7(a). The surface representation is shown in 2.7(b), where the grey-level of pixels is mapped onto the z-axis to show the contrast attenuation across the vessel structure mimicking the light absorption process described above.

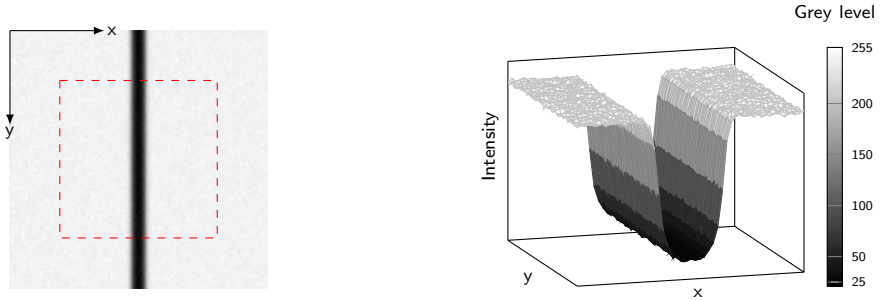

(a) **(b)**

Figure 2.7: Synthetic imaging of a single straight vessel. (a) 7-pixel diameter synthetic vessel corrupted by Gaussian noise with a standard deviation of two grey levels. (b) Surface representation of the section denoted by dashed lines in (a).

2.3 Challenges: illumination, unwanted and phantom objects

Uneven illumination, noise and poor contrast in images affect the accuracy of image analysis methods such as object segmentation. For that reason, enhancement algorithms can be applied as pre-processing work to improve the effectiveness of the image analysis algorithms.

In retinal images, a variety of reflexes is introduced by the optics of the fundus camera system. Some illumination effects can be reduced by changing the type of lamp or light filters used, which allows producing a more uniform illumination across the field of view in retinal imaging. Another factor to consider is the histology of the eye fundus that eventually reflects an amount of light [79]. Figure 2.8 shows a variety of common reflections present in retinal images. As can be seen, reflections can occur along vessel centrelines, in parallel to vessel structures, surrounding the optic disc and macula; other random reflections can be introduced due to abnormalities in the eye fundus. Some approaches have been developed to cope with light reflections. For instance, Wang *et al.* [114] modelled the central reflex along vessels using Hermite basis functions.

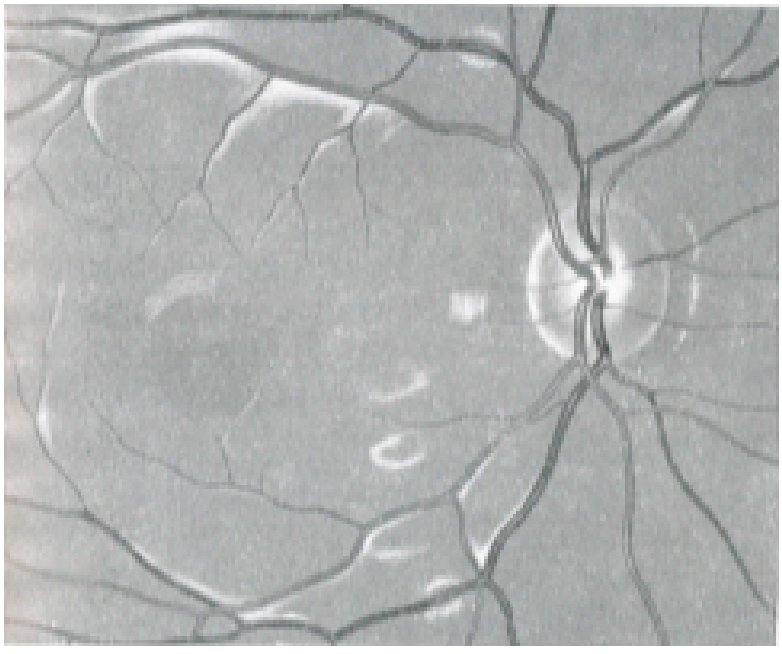

Figure 2.8: Variety of normal retinal reflex [79].

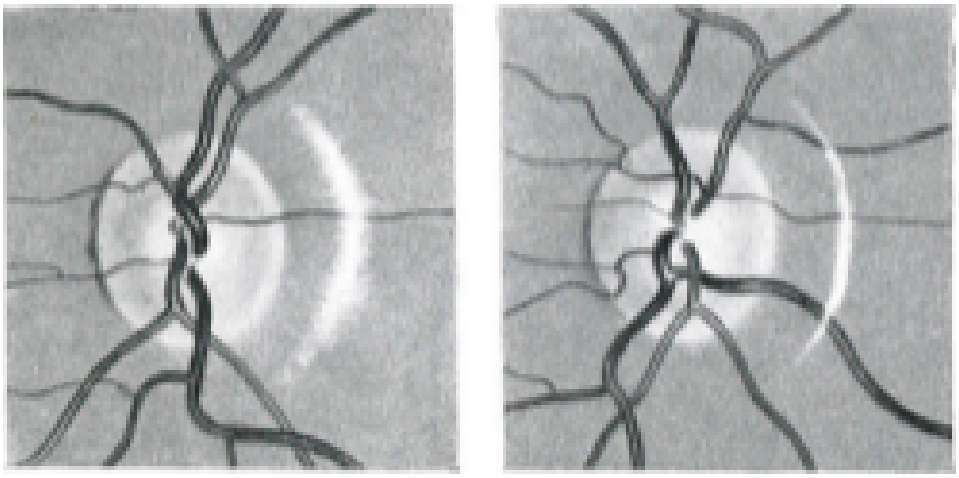

Figure 2.9: Weiss's reflexes [79].

Phantom objects—formed by light reflections—can be seen near the optic disc boundaries and macular region. The reflex near the optic disc is concentric to the optic disc border and is known as Weiss's reflex [79] (see Figure 2.9). Moreover, in some cases, reflections surrounding the macula and fovea centre can be observed as shown in Figure 2.10.

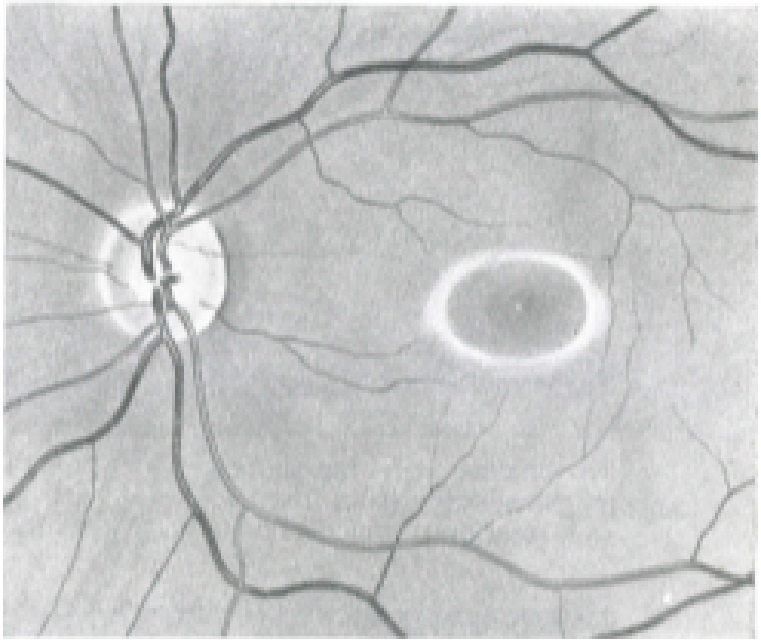

Figure 2.10: Perimacula reflex and reflex from the fovea pit [79].

Linear axial reflections running along the centreline of arteries and veins is another of common reflex observed in retinal images. In arteries, the reflection is sharp, with uniform width and occupies approximately the middle third of the vessel width. In veins, reflection is narrower in proportion to the vessel diameter and the intensity of

reflection is higher [79]. This type of reflection can be observed along the main vessels in Figure 2.8 (p. 14).

2.4 Taxonomy of blood vessel presentations

A morphology classification of vessel segments, which may appear in real screenings, can be defined. The idea behind this classification is the evaluation of existing vessel detectors to construct a robust method for vessel-network segmentation. Five types of presentations in which vessels can appear in retinal images were defined. Each of the classes is described below.

2.4.1 Straight and isolated vessel

Is defined as a single straight tube-like structure in a 3D space representation. For 2D images, the intensity profile across this structure is governed by the Beer-Lambert Law as a light absorption model. As the tube-like primitive tends to be infinite, the intensity along the object remains constant. For 3D images, this object can be computed as a filled cylinder in a 3D space. Definition of this type of vessel segment is essential for the construction of parallel and crossing vessels.

2.4.2 Parallel vessels

This classification corresponds to an image's region where two straight vessels (as described before) appear separated by a constant distance along their direction. This model can be produced by adding two straight vessels on a background patch, where the background intensity is also given by Beer-Lambert Law. The vessel radii may be different, and the separation between them may vary to simulate the close structures appearing in screenings. Parallel objects may appear in even 2D and 3D images. Proximity between objects plays an important role as Gaussian filters—discussed in Section 2.5—can modify the intensity of nearby objects when the distance between them is smaller than the size of the employed Gaussian kernel.

2.4.3 Crossing vessels

These are defined as an image with two straight vessels intersecting in a random angle. This image can be produced by adding two randomly-rotated straight vessels. Owing to the process of light beams crossing eye tissue, overlapping objects can appear as cross-junction-like structures in 2D images. Nonetheless, the intensities of pixels in the intersection area are attenuated due to the light beam having crossed more tissue layers. This effect can make vessel detection difficult if the detector is based on straight vessel models only.

2.4.4 Bifurcation

Is formed by a single straight vessel with two daughter vessel structures. The geometry (angles and radii) of the bifurcation is defined following the nature of arteries branching, which can be modelled using Murray's law that states that bifurcation angles of daughter vessels are equal ($\approx 37.5°$) when their radii are equal [59]. In order to produce 2D images, a 3D bifurcation model is constructed within a 3D space, where the bifurcation direction is along the z-axis and the branch and daughters are placed at the origin of the x-axis. Afterwards, a 2D image can be computed by integrating the cells contained in the 3D model along the y-axis and using the Beer-Lambert Law.

2.4.5 Corkscrew-like vessel

Is defined as a curved vessel segment. For 2D images, this structure is considered as a wave behaviour, whose diameter, wavelength and amplitude values are constant. In order to produce a 2D image sample, a 3D helical coil can be constructed within a 3D space. The radius of the coil is associated with the desired vessel radius; the curvature and length values remain constant. The helical path is then constructed along the z-axis and the curvature is fixed to the zero position for both x- and y-axis. Due to symmetry, the integration along either, x- or y-axis generates a 2D image with a wave-like structure of width given by the coil radius. In that case, the intensity across the

vessel takes into account the overlapping effect produced by the curvature and length of the coil. Finally, the Beer-Lambert Law is used to estimate the intensities of pixels.

Figure 2.11 summarises the taxonomy of vessel presentation used in this research, where the vessel centre line and a defined point of interest in the image are shown.

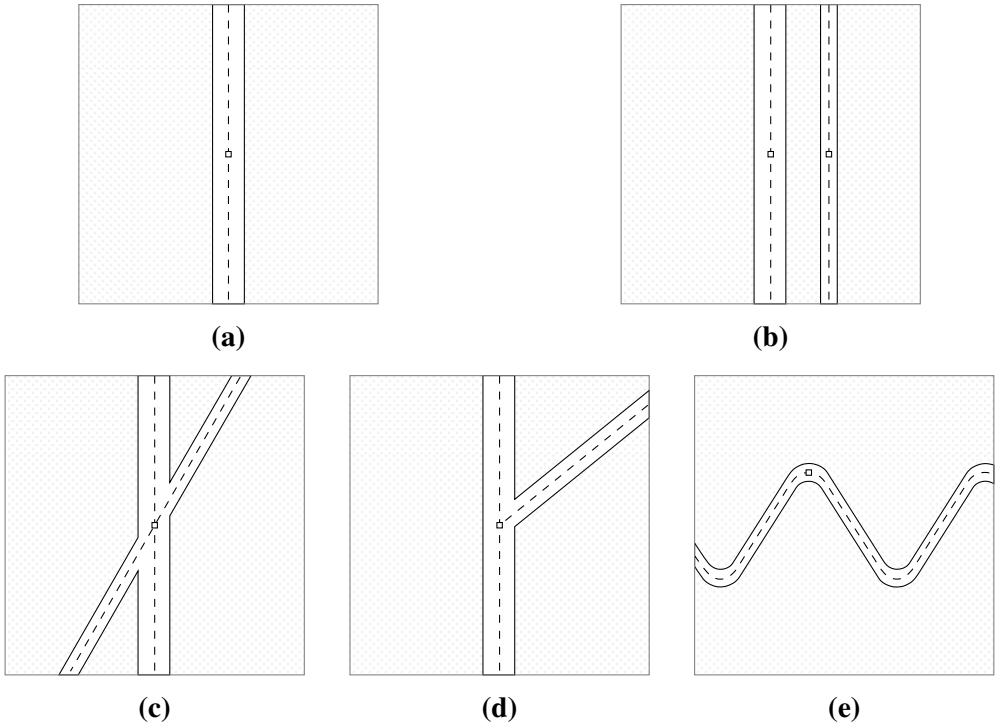

Figure 2.11: Taxonomy of vessel presentation in retinal images for the construction of synthetic images: (a) isolated-straight vessel; (b) parallel vessels; (c) crossing vessels; (d) bifurcation; and, (e) corkscrew-like vessel.

2.5 Scale-space theory

An intrinsic property of objects is that they only exist over a certain range of scales. A branch of a tree, for instance, can be defined from, say, few centimetres to few meters. It is insignificant to discuss the idea of a tree branch at nanometre or kilometric scales [70].

The idea behind the scale-space theory is to separate information across scales to cope with detection of objects at a range of sizes. In the present research, for instance, vessels over a range of sizes appear within an image and multi-scale representation can help to cope with feature extraction of narrow and wide vessel-like structures.

On the contrary, some approaches work at specific scales. For example, Orkisz *et al.* [85] apply a mean filter in the direction of the vessels but this, however, shows problems with detecting vessels over a large size range.

Lindeberg [67] introduced the idea of using a family of normalised derivatives based on Gaussian kernels to represent an image across scales, where the scale is a positive real value and the zero-scale corresponds to the original image [67] as it is described in Equation 2.1. Figure 2.12 shows different scale-space versions of a synthetic isolated and straight vessel for a set of linearly-spaced scales.

$$L(\cdot;\sigma) = \begin{cases} I, & \sigma = 0 \\ G(\cdot;\sigma) \otimes I, & \sigma > 0 \end{cases} \tag{2.1}$$

where I is the original image, $\sigma \in \mathbb{R}_+$ is the scale parameter, G is a Gaussian kernel of size σ with zero mean, and $\otimes$ is the convolution operator. The N-dimensional Gaussian kernel of size σ with zero mean can be defined as:

$$G(\vec{x};\sigma) = \frac{1}{(\sqrt{2\pi}\sigma)^N} e^{-\frac{x_1^2 + \ldots + x_N^2}{2\sigma^2}} \tag{2.2}$$

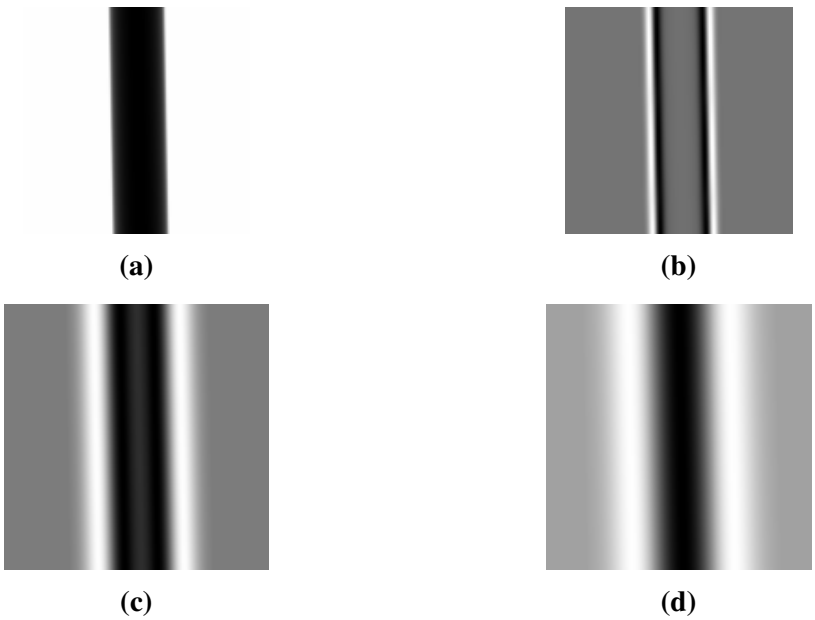

Figure 2.12: Scale-space representation of an isolated-straight vessel segment in synthetic X-ray angiogram: (a) $\sigma_N = 0$ (original image); (b) $\sigma_N = 2$; (c) $\sigma_N = 6$; and, (d) $\sigma_N = 10$.

Lindeberg introduced the γ parameter to compensate for the dispersion generated by the convolution of the original image with Gaussian kernels [67]. Therefore, the comparison of responses across all scales remains fair. Equation 2.3 shows an extended version of Equation 2.1 for implementation of the γ-parameter value.

$$L(\cdot;\sigma) = \sigma^{\gamma}\, G(\cdot;\sigma) \otimes I \tag{2.3}$$

2.5.1 Scale selection

Lindeberg [68] suggests using the local maximum as a way of selecting the best response across all scales. This scale-selection method allows extraction of features from an image when a family of scales is employed. The method has been used in [35, 53, 72, 73, 106, 116]—multi-scale vessel detection algorithms—and can be defined as:

$$L(\cdot) = \max_{\sigma}\, L(\cdot;\sigma) \tag{2.4}$$

where $L(\cdot;\sigma)$ is the local response at scale σ.

2.6 Local descriptors

Since vessels can be described as line-like objects in retinal images, line detector algorithms can be used to enhance those structures to be segmented. Rapid changes of intensity between vessel-like and background-like pixels suggests that algorithms to detect those changes can be employed. In eye fundus images, the background can be described as a brighter region than those pixels forming vascular structures. Other imaging modalities, such as angiography, present vessel pixels brighter than the background.

If the intensity of an ideal vessel segment—straight and uniformly filled—is analysed in its cross-section view, the profile can be described as a valley or ridge based on the imaging modality. Local valley and ridge descriptors [30, 44]—matching vascular structures due to their geometrical shape—can be used to enhance vessel-like pixels in a given image.

The Hessian matrix of an image can be used to estimate the local principal curvature map. The matrix can be computed by applying second-order derivatives to the image at a given scale. The Hessian matrix decomposition—eigenvectors and eigenvalues—can then be used to describe the local curvature at a given point in the image. In a 2D image, for instance, the first eigenvector—the one whose corresponding eigenvalue has the largest absolute value—represents the direction of the greatest curvature; and, the second eigenvector—whose corresponding eigenvalue has the smallest absolute value—gives the direction of the least curvature. Eigenvectors are always orthogonal, equivariant to rotation and real valued.

Description of the local curvature due to the Hessian matrix can be used to match pixels to line-like structures in an image. An analysis of the Hessian matrix and its use is developed in Section 2.6.1. The aim of the analysis is the use of the Hessian matrix to describe the local principal curvature for the enhancement of line-like structures in eye fundus images.

2.6.1 Hessian matrix analysis

Eigenvalue analysis of the Hessian matrix is widely used for vessel detection [35, 73, 106]. The Hessian matrix is the second-order derivative matrix of every pixel in an image, which provides information about the grey-level curvature around a pixel. The Hessian matrix can be computed by the convolution of an image with a second-order derivative of a Gaussian kernel, also known as Laplacian of Gaussian (LoG). For an N-Dimensional image I, the Hessian matrix at the point x is given by

$$H(x) = \begin{bmatrix} \frac{\partial^2 I}{\partial x_1 \partial x_1} & \frac{\partial^2 I}{\partial x_1 \partial x_2} & \cdots & \frac{\partial^2 I}{\partial x_1 \partial x_N} \\ \frac{\partial^2 I}{\partial x_2 \partial x_1} & \frac{\partial^2 I}{\partial x_2^2} & \cdots & \frac{\partial^2 I}{\partial x_2 \partial x_N} \\ \vdots & \vdots & \ddots & \vdots \\ \frac{\partial^2 I}{\partial x_N \partial x_1} & \frac{\partial^2 I}{\partial x_N \partial x_2} & \cdots & \frac{\partial^2 I}{\partial x_N \partial x_N} \end{bmatrix} \tag{2.5}$$

where $x_i, i \in \{1,2,\ldots,N\}$ are the dimensions of the image I. It is important to underline that the Hessian matrix is real and symmetric, with real eigenvalues and orthogonal-eigenvectors.

For simplicity, examples in this analysis are described for a 2D image. Hence, the Hessian matrix for a pixel is given by Equation 2.6.

$$H = \begin{bmatrix} I_{xx} & I_{xy} \\ I_{xy} & I_{yy} \end{bmatrix} \tag{2.6}$$

where I_{xx} , I_{xy} and I_{yy} are the second-order partial derivatives of the image I.

Eigenvalue signs and ratios are used for modelling topographical structures in images by regarding the intensity of pixels as a third dimension [44, 112]. Figure 2.13 shows some surface descriptions using eigenvalues and Hessian coefficients to compute the θ parameter, defined by Equation 2.7.

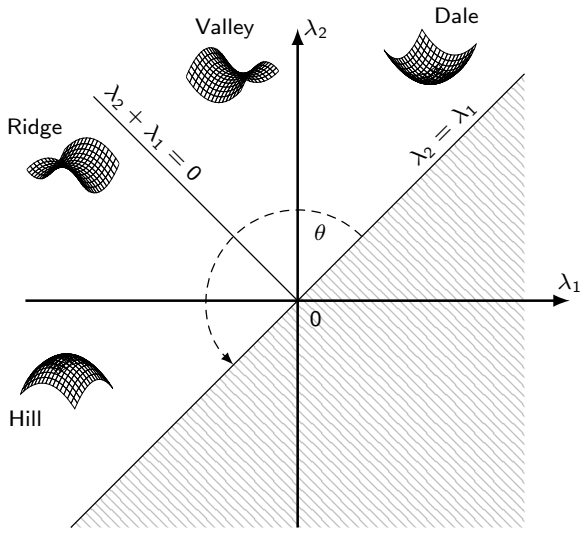

Figure 2.13: Surface shape description based on the Hessian matrix for a 2D image. Eigenvalues λ_1, λ_2 and orientation θ can be estimated using the second-order partial derivatives of an image and θ given by Equation 2.7 [112].

$$\theta(x,y) = \arctan\left(\frac{\sqrt{(I_{xx} - I_{yy})^2 + 4I_{xy}^2}}{I_{xx} + I_{yy}}\right) \tag{2.7}$$

where I_{xx} and I_{yy} are the second-order derivatives along the x- and y- direction respectively; and, I_{xy} the second-order derivative along the x- and y- direction of an image I.

Since the ideal intensity profile across a vessel can be described as a ridge-like structure, eigenvalue analysis and the Hessian matrix itself have been used for vessel detection. Krissian *et al.* [54] for instance, describe the ideal intensity profile across a vessel as a Gaussian distribution. In a 3D vessel structure, for instance, the profile in both *x*- and *y*-directions is Gaussian, so the intensities across a section view are given by the 2D Gaussian function (see in Figure 2.14). Yuan et al [121] use the same definition as do Drechsler and Laura [26] for a quantitative comparison of vessel detectors. Based on the physical process of absorption, in this analysis it cannot be assumed that the ideal intensity profile across a vessel is Gaussian.

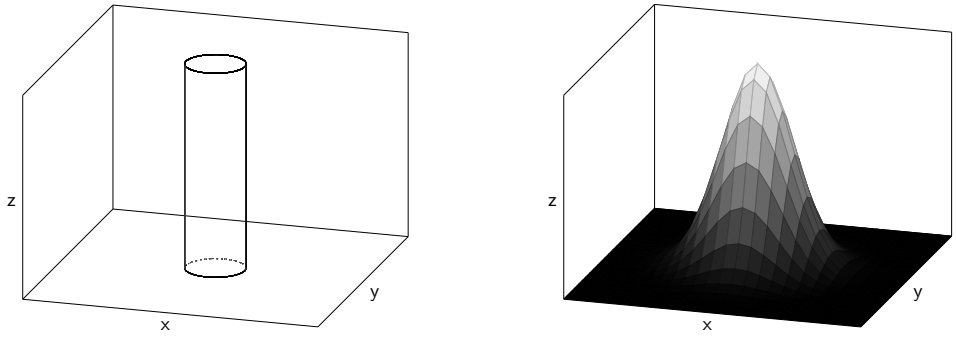

(a) **(b)**

Figure 2.14: Initial model of a vessel. (a) representation of the model; and (b) the Gaussian-like intensity profile of the cross-section view due to the sum of the Gaussian profiles along *x*- and *y*-direction, Krissian *et al.* [54].

Although the Hessian matrix provides information about the orientation (see Equation 2.7), there is not enough information for modelling shapes. Hence based on linear algebra, eigenvalues and eigenvectors are computed.

Let A be a square matrix of $n \times n$. A scalar λ is said to be an eigenvalue of A if

$$A\mathbf{u} = \lambda\mathbf{u} \; for\ some\ vector\ \mathbf{u} \neq 0 \tag{2.8}$$

The vector $\mathbf{u}$ is called an eigenvector corresponding to λ. In addition, λ is an eigenvalue of A if and only if

$$\det(A - I\lambda) = 0 \tag{2.9}$$

where I is the identity matrix. Finally, $\mathbf{u}$ is an eigenvector of A corresponding to λ if and only if $\mathbf{u}$ is a non-zero solution

$$(A - I\lambda)\,x = 0 \tag{2.10}$$

Equation 2.8 is known as characteristic equation. Regarding the Hessian matrix H as the value of A in Equation 2.8, and replacing subscripts in Equation 2.5 by index subscripts of H, then the characteristic equation for a 2D image can be defined as

$$\begin{bmatrix} h_{11} - \lambda & h_{12} \\ h_{21} & h_{22} - \lambda \end{bmatrix} = 0 \tag{2.11}$$

By taking the determinant of the matrix 2.11, the characteristic equation can be written as

$$(h_{11} - \lambda)\,(h_{22} - \lambda) - (h_{12})^2 = 0 \tag{2.12}$$

Solving the characteristic equation, of second-order in this case, the eigenvalues are given by Equations 2.13 and 2.14 respectively.

$$\lambda_1 = \frac{(h_{11} + h_{22}) + \sqrt{(h_{11} + h_{22})^2 + 4h_{12}^2}}{2} \tag{2.13}$$

$$\lambda_2 = \frac{(h_{11} + h_{22}) - \sqrt{(h_{11} + h_{22})^2 + 4h_{12}^2}}{2} \tag{2.14}$$

Eigenvalue signs and size can be used to describe shapes locally. The eigenvectors provide information to estimate the orientation along line-like structures and it is given by the eigenvector associated with the smallest eigenvalue. Figure 2.15 for instance, shows the eigenvector orientation for a bright vessel on dark background in a 2D image, where eigenvector e_1 is associated with eigenvalue λ_1, and $|\lambda_1| \leq |\lambda_2|$.

Imaging modalities provide diverse descriptions of the contents of images; for example, in X-ray angiograms and eye fundus images, objects appear dark on bright background, and the opposite occurs in MR and Fluorescein Angiograms. Nevertheless, this obstacle can be solved by negating the image. Some approaches use different eigenvalue ordering to describe shapes. In [35], for instance, eigenvalues are sorted by

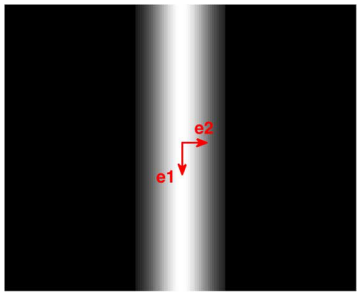

Figure 2.15: Synthetic vessel with Gaussian intensity profile, with the eigenvectors shown at the centre [121].

magnitude in increasing order, and in [106] they are sorted by value in increasing order (negative to positive). Following the work developed in [35], Table 2.1 summarises structure patterns for shapes in 2D and 3D images using eigenvalue signs and sizes.

Table 2.1: Possible local structures in 2D and 3D, depending on the value of the eigenvalues (H=high, L=low, N=noise, usually small; $+/-$ indicates the sign of eigenvalues). The eigenvalues are sorted as $|\lambda_1| \leq |\lambda_2| \leq |\lambda_3|$ [35].

2D		3D			
λ_1	λ_2	λ_1	λ_2	λ_3	Orientation pattern
N	N	N	N	N	Noisy, no preferred direction
		L	L	H-	Plate-like structure (bright)
		L	L	H+	Plate-like structure (dark)
L	H-	L	H-	H-	Tubular structure (bright)
L	H+	L	H-	H+	Tubular structure (dark)
H-	H-	H-	H-	H-	Blob-like structure (bright)
H+	H+	H+	H+	H+	Blob-like structure (dark)

2.7 Vessel-ness measures

In this section, the Lorenz *et al.* [72, 73], Sato *et al.* [106] and Frangi *et al.* [35] vessel detector approaches are described. All these approaches base their work on a very similar methodology: Hessian matrix analysis described in Section 2.6.1 and multi-scale representation described in Section 2.5. The substantive difference among these works is the way of using eigenvalues to describe shapes. In addition, Sato introduces a noise normalisation process which is described in Section 2.7.2.

2.7.1 Lorenz *et al.*

In [73] a multi-scale vesselness measure is proposed where all the eigenvalues are considered in the vesselness measurement. Eigenvalues are sorted by magnitude in decreasing order. This approach is the only one—of the three studied—that does not use parameters in the filter function. By considering the eigenvalue order as $|\lambda_1| > |\lambda_2| > |\lambda_3|$, structures described on Table 2.2 can be distinguished.

Table 2.2: Structures distinguished based on the eigenvalues sorted by magnitude in decreasing order. All eigenvalues in either 2D and 3D images are included in the shape models [73].

2D	3D	Structure
$\lambda_1 < 0$ $\lvert\lambda_1\rvert$ large $\lvert\lambda_2\rvert$ small	$\lambda_1, \lambda_2 < 0$ $\lvert\lambda_1\rvert, \lvert\lambda_2\rvert$ large $\lvert\lambda_3\rvert$ small	Bright line
$\lambda_1 > 0$ $\lvert\lambda_1\rvert$ large $\lvert\lambda_2\rvert$ small	$\lambda_1, \lambda_2 > 0$ $\lvert\lambda_1\rvert, \lvert\lambda_2\rvert$ large $\lvert\lambda_3\rvert$ small	Dark line
	$\lambda_1 < 0$ $\lvert\lambda_1\rvert$ large $\lvert\lambda_2\rvert, \lvert\lambda_3\rvert$ small	Bright plane
	$\lambda_1 > 0$ $\lvert\lambda_1\rvert$ large $\lvert\lambda_2\rvert, \lvert\lambda_3\rvert$ small	Dark plane

In 2D images, a dark line structure on a bright background is described by a large positive second-order derivative across the line and a small second-order derivative along the line. Thus, a large positive and a small eigenvalue of positive or negative sign are considered. It can be said that this approach bases the filter function on the eccentricity definition.

The local Lorenz vesselness function for a 2D or 3D image at scale σ is given by Equations 2.15 and 2.16 respectively.

$$V_L(\cdot;\sigma) = \frac{|\lambda_1|}{|\lambda_2|} \tag{2.15}$$

$$V_L(\cdot;\sigma) = \frac{|\lambda_1| + |\lambda_2|}{2|\lambda_3|} \tag{2.16}$$

2.7.2 Sato *et al.*

This approach describes a curvilinear structure detector in 3D images based on a multi-scale representation. Like Lorenz *et al.* [73], the Hessian matrix is computed to evaluate each point of a given image, and then, the highest response over all scales corresponds to the filter outcome. This work is focused on bright line detection on dark background images, hence the eigenvalues order contrasts to the Lorenz *et al.* [73] order. The eigenvalues of the Hessian matrix are denoted by λ_1, λ_2, λ_3 where $\lambda_1 > \lambda_2 > \lambda_3$, and their corresponding eigenvectors e_1, e_2, e_3. The eigenvector e_1 represents the direction along the highest second-order derivative; this is the z-axis which is also the direction of the line.

In the ideal case—a straight bright line-like(2D) or tube-like(3D) on a dark background—the profile across the structure is given by Equation 2.17 where x and y are the distances from the origin (central section of the structure) in the horizontal and vertical axes and are normal to the longitudinal direction of the structure; z is the cross-sectional view of the structure; and σ, is the standard deviation that defines the spread of the intensity profile. Furthermore, the eigenvalue λ_1 is regarded as close to zero and λ_2, λ_3 as similar but of high-negative values. Table 2.3 summarises the structures defined by Sato *et al.* [106] regarding eigenvalue ratios for analysis of 3D images.

$$I(x,y,z) = \exp\left(\frac{-\left(x^2+y^2\right)}{2\sigma^2}\right) \tag{2.17}$$

Table 2.3: Description of structures in 3D images determined by the size of eigenvalues. Eigenvalues are sorted in increasing order [106].

3D image	Structure
$\lambda_1 \approx 0$ $\lambda_2 \approx \lambda_3 \ll 0$	Line
$\lvert\lambda_3\rvert \gg 0$ $\lvert\lambda_3\rvert \gg \lvert\lambda_2\rvert$ $\lvert\lambda_2\rvert \approx 0$	Sheet
$\lambda_1 < 0$ $\lvert\lambda_1\rvert \approx \lvert\lambda_2\rvert$	Blob

Sato's vesselness function for a point in a 3D image at scale σ is given by

$$V_S(\cdot;\sigma) = f(\lambda_1;\lambda_c) \times \lambda_c \tag{2.18}$$

where

$$\lambda_c = \min(\lambda_2;\lambda_3) = -\lambda_2 \tag{2.19}$$

and

$$f(\lambda_1;\lambda_c) = \begin{cases} \exp\left(-\dfrac{\lambda_1^2}{2(\alpha_1\lambda_c)^2}\right), & \lambda_1 \leq 0, \lambda_c \neq 0 \\ \exp\left(-\dfrac{\lambda_1^2}{2(\alpha_2\lambda_c)^2}\right), & \lambda_1 > 0, \lambda_c \neq 0 \\ 0, & \lambda_c = 0 \end{cases} \tag{2.20}$$

where $\alpha_1 < \alpha_2$ and their values were fixed to 0.5 and 2.0 respectively based on experimentation. Furthermore, Sato *et al.* [106] pointed out that responses were high at small scales for both line structures and noise components. Therefore, scale selection in this approach is not given by selecting the highest response over all scales. Sato introduced the notion of multi-scale integration rather than the normalisation of scaled images using the γ-parameter as Lindeberg suggested in [67]. The multi-scale integration is given by

$$\max_i \frac{1}{n_i} L_i(x,y,z) \tag{2.21}$$

where n_i is the standard deviation of the noise amplitude at scale i, and L_i (see Equation 2.18) is the line filter response at scale i. n_i is calculated using a region of the image from which curvilinear structures are absent. In practice this process is not easy to compute for an automatic image processing tool.

2.7.3 Frangi *et al.*

A multi-scale vesselness measure is proposed in this approach based on the analysis of the Hessian matrix. Eigenvalues are used for modelling a vesselness function based on a geometrical design. Eigenvalues are sorted by magnitude in increasing order denoted as $|\lambda_1| \leq |\lambda_2| \leq |\lambda_3|$. Hence, λ_1 is in the plane with the lowest curvature,

and its eigenvector $\hat{u}_1$ indicates the orientation of the vessel. Figure 2.16 shows the geometrical model used, where the eigenvalues describe the shape of the object [35].

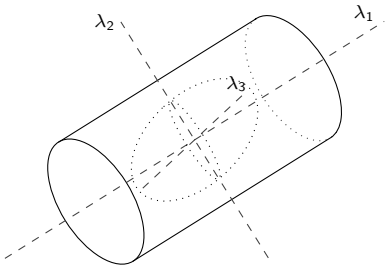

Figure 2.16: Orientation of local eigenvalues describing the principal direction of a 3D tube-like structure [35].

This approach uses all the three eigenvalues for modelling shape. Table 2.1 (p.25) summarises the structures defined by Frangi *et al.* regarding eigenvalues sorted by magnitude in increasing order. Frangi *et al.* defined two geometric ratios expressed by $\mathscr{R}_B$ and $\mathscr{R}_A$ in order to differentiate line- from blob-like structures. The Frangi's vesselness response for a given image at scale σ is given by

$$V_F(\cdot;\sigma) = \begin{cases} 0, & \lambda_1 > 0 \; or \; \lambda_3 > 0 \\ \left(1-\exp\left(-\frac{\mathscr{R}_A^2}{2\alpha^2}\right)\right)\exp\left(-\frac{\mathscr{R}_B^2}{2\beta^2}\right)\left(1-\exp\left(-\frac{\mathscr{S}^2}{2c^2}\right)\right), & otherwise \end{cases} \tag{2.22}$$

where

$$\mathscr{R}_B = \frac{|\lambda_1|}{\sqrt{|\lambda_2\lambda_3|}} \tag{2.23}$$

$$\mathscr{R}_A = \frac{|\lambda_2|}{|\lambda_3|} \tag{2.24}$$

and

$$\mathscr{S} = \sqrt{\sum_{j\leq D}\lambda_j^2} \tag{2.25}$$

The ratio $\mathscr{R}_B$ measures the deviation from a blob-like structure. $\mathscr{R}_A$ measures the eccentricity of the plane orthogonal to eigenvector $\hat{u}_1$, and $\mathscr{S}$ is a measure of the second-order structure. $\mathscr{S}$ becomes low in the background where no structure is present and the eigenvalues are small due to lack of contrast. In addition, Frangi *et*

al. defined three normalisation factors to control the sensitivity of the filter: α, β and c. The α and β values were fixed to 0.5 and the value of c depends on the grey-scale range of the image and was obtained by experimentation.

For 2D images, Frangi *et al.* proposed the Equation 2.26, where $\mathscr{R}_B = \lambda_1/\lambda_2$ is the blobness measure and accounts for the eccentricity of the second-order ellipse. The conditions in Equations 2.22 and 2.26 consider detection of bright curvilinear structures. Therefore, the conditions or images should be inverted for dark objects in bright background.

$$V_F(\cdot;\sigma) = \begin{cases} 0, & \lambda_2 > 0 \\ \exp\left(-\frac{\mathscr{R}_B^2}{2\beta^2}\right)\left(1-\exp\left(-\frac{\mathscr{S}^2}{2c^2}\right)\right), & otherwise \end{cases} \tag{2.26}$$

2.7.4 Vesselness response selection

The approaches studied in this section are based on the multi-scale representation introduced by [65, 67, 68, 69, 70] to cope with scale variation. Lindeberg suggested using the γ parameter to compensate for dispersion when scale increases (see Equation 2.3, p.20). This parameter works as a normalisation method to compare the response over all scales. Therefore, the local maximum response is the resultant vesselness measure given by the vessel detector employed.

Figure 2.17 shows the multi-scale and local maxima representation for the selection of best response in a 2D image analysis. In the figure, x and y axes represent the width and height of a given image; a set of stacked layers denoted by σ represent the scales; finally, for every cell in the image, the highest response across all scales is selected to form the resulting filtered image.

Lorenz, Sato and Frangi vesselness response, from a synthetic crossing-vessels patch, across a set of selected scales $\sigma = \{0,1,3,10\}$ are shown in Figure 2.19. The crossing-vessels sample is formed by two straight vessels of the same diameter (8.5 pixel-units) crossing at the central point of the image lattice. For simplicity, the angle between the two vessels was set to 90°. The image was corrupted by Gaussian noise of power $\sigma = 2.6$ and randomly rotated (26°) producing the image shown in Figure 2.18. The resulting filtered image for each vessel detector (see Figure 2.20) is formed

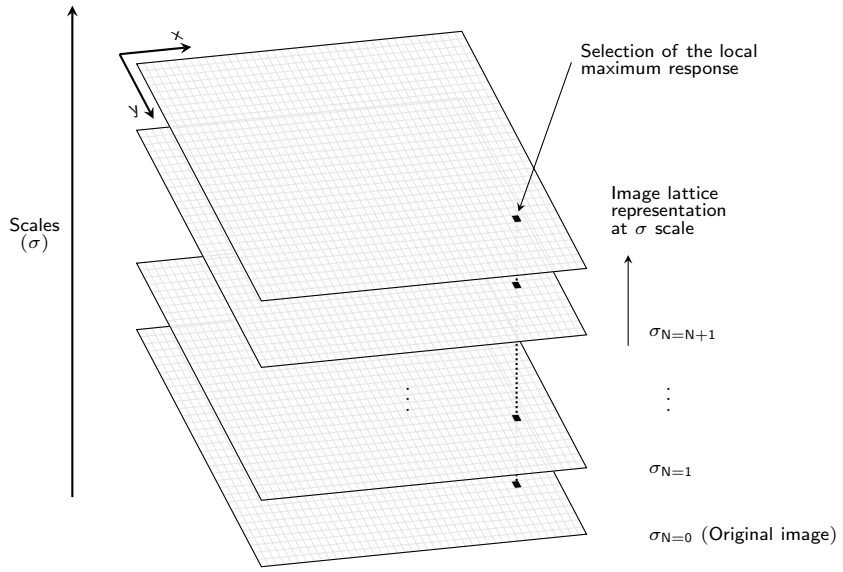

Figure 2.17: Searching the local maximum response in a scale-space representation [70].

by selecting the best local vesselness response across all scales; the brighter the pixel intensities, the higher the vesselness response.

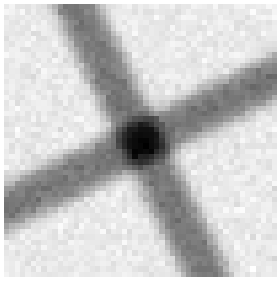

Figure 2.18: Synthetic crossing-vessels patch formed by two straight vessels crossing at the central point of the image lattice.

2.8 Conclusions

In this chapter, the image formation process in eye fundus cameras was studied. This type of device uses a lamp to illuminate the back of the eye. Due to properties of the eye tissue, light is reflected and beams are captured by the camera sensor. This allow production of an image where the intensities of pixels can be seen as the amount of light crossing eye tissue layers: the fewer the number of eye tissue crossed higher the intensities of pixels.

In the ideal case, uniform background and vascular structures should be shown in a retinal image. Nonetheless, there are some factors that introduce unwanted ob-

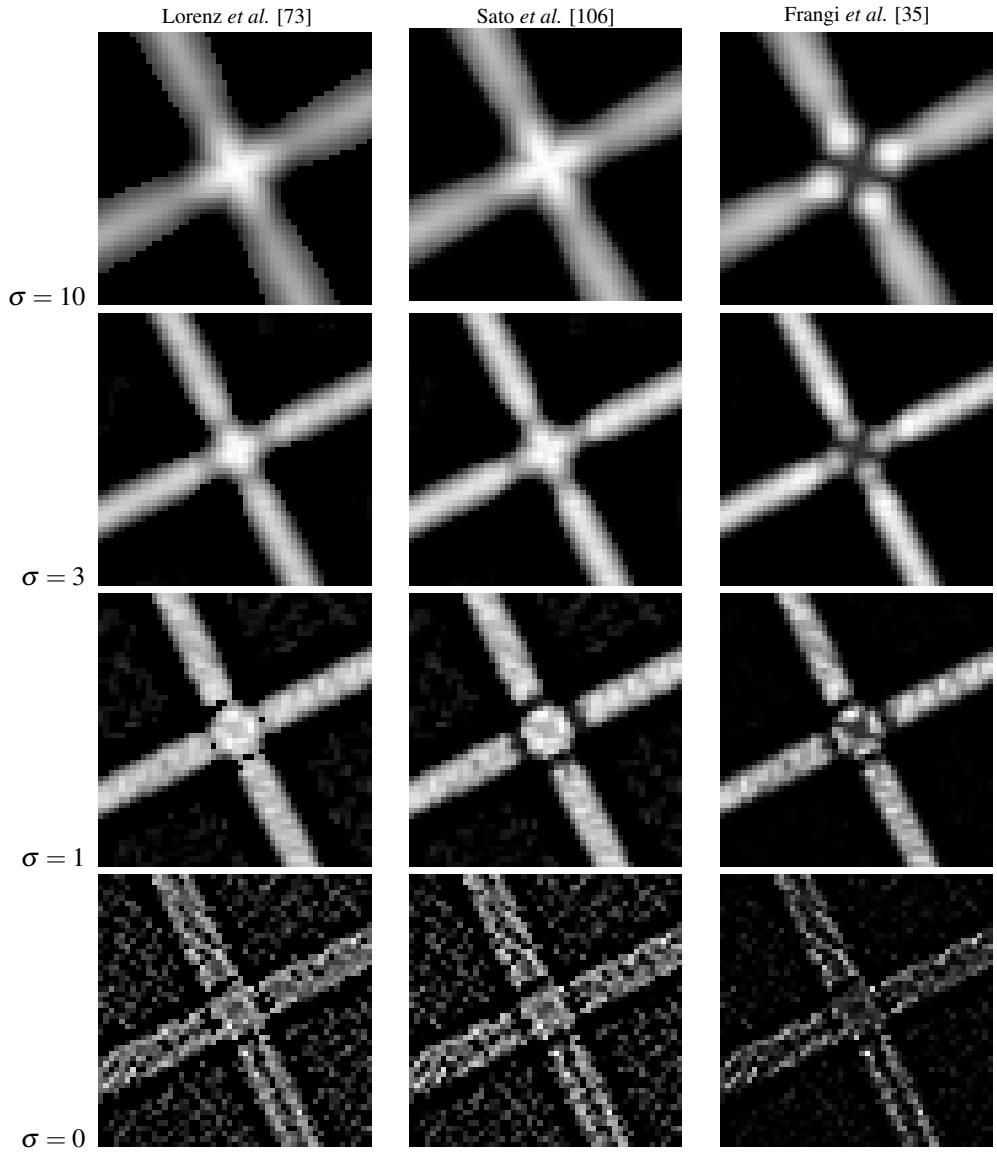

Figure 2.19: Lorenz, Sato and Frangi vesselness response from a crossing-vessels sample across a set of selected scales $\sigma = \{0, 1, 3, 10\}$.

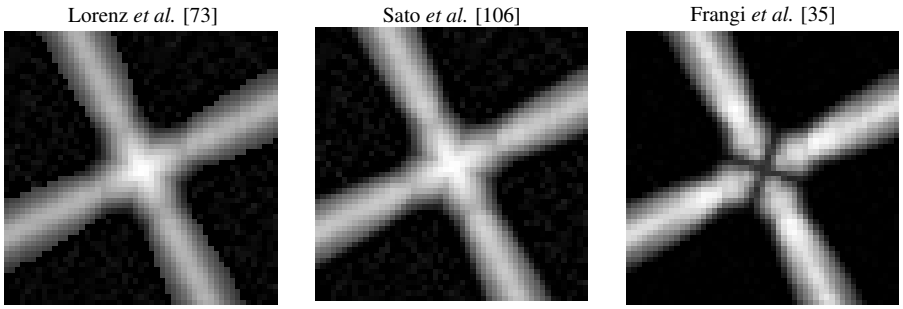

Figure 2.20: Lorenz, Sato and Frangi filtered image due to the local maximum response across all scales.

jects into the image formed. In the simplest form, noise is added to the image by the hardware when the signal is captured and converted into a digital representation. Other factors such as uneven lighting, eye tissue effects due to health conditions and reflexes due to the semi-transparent tissue properties, deterioration of the transmittance of light beams eventually produce unwanted shapes in the computed image.

A model described as line-like structures was defined to represent the desired objects—vessel segments—in retinal images. Therefore, line detector algorithms based on analysis of rapid changes in intensities of pixels were studied. In addition, local curvature analysis given by computing the Hessian matrix to estimate a vesselness measure was reviewed. Three of the most popular vessel detector algorithms were studied: Lorenz *et al.* [72, 73], Sato *et al.* [106] and Frangi *et al.* [35]. The studied algorithms are based on the analysis of the eigenvalues and eigenvectors of the computed Hessian matrix to define their vesselness functions. Those algorithms integrate the scale-space theory to cope with the segmentation of vessels of a range of calibres.

Integration of the reviewed topics can be used to develop a robust vessel detector method able to cope with the common problems that make vessel segmentation difficult. Further analysis of eigenvalue signs, ratios, and sizes used by vesselness functions can be used to estimate the local likelihood or membership function of a pixel belonging to a vessel-like structure.

Chapter 3

Vessel segmentation approaches

3.1 Introduction

In medical imaging, segmentation of vessel networks is essential for several medical applications such as diagnosis of vascular-related diseases or assessing a course of treatment over time. Advances in imaging modalities yield capturing images able to—at some extent—distinguish interesting objects based on the medical application domain. X-ray imaging, for instance, produces images where objects appear with larger contrast relative to the background. Other imaging modalities such as Magnetic Resonance Imaging (MRI) produces volumetric data that can be reconstructed for the analysis of scanned parts of the body.

A wide variety of imaging modalities exist producing images with varying features and medical applications. We cannot assume that a developed segmentation method can be applied to any of the images produced by the different current scanners. Images used for a particular medical purpose can be studied to develop segmentation methods based on either the principles of the imaging modality, features of target objects and variations that can make their segmentation difficult.

Previously published vessel segmentation approaches are reviewed in this chapter. Since the methods reviewed can use similar techniques in their process, their classification can be based on the features in contrast to other approaches. There are methods, for instance, focused on vessel centreline detection, others enhance the edges of vessel networks.

A performance comparison of three previously published vessel detectors is also described in this chapter. The comparison has been published in *Performance comparison of low-level vessel detection algorithms for segmentation of x-ray angiograms* [109] as part of this thesis. The comparison is based on Monte Carlo simulations to measure the performance of the tested algorithms by analysing local features in synthetic vessel images. A set of synthetic images were generated by varying features such as vessel radius, noise, focus and orientation. The formation process of synthetic vessels is based on an ideal vessel model defined as a uniformly-filled cylinder representing a straight vessel structure, where the intensities of vessel-pixels are governed by the Beer-Lambert Law [19] describing the absorption of light beams as they cross the cylindrical structure, mimicking X-ray angiography imaging.

By analysing the performance of the vessel detectors examined, the best rated algorithm was selected to compare the vessel-pixel labelling method proposed in this thesis.

3.2 Vessel segmentation approaches

Analysis of local features, connected components and tracking methods are some of the image processing algorithms much-used to enhance vessel structures in medical images. Pattern recognition, template matching [125] and classifiers such Artificial Neural Networks (ANN) [82, 95] and Support Vector Machines (SVM) [97] have also been employed for segmentation of vessel structures where vessel-pixels are commonly regarded as objects of interest and the rest of the pixels as unwanted objects or background. Other approaches use geometric models and active contour models for vasculature segmentation. Gooya *et al.* [41], for instance, use geometric models and theory of curve evolution of geometric flows for vessel segmentation in 2D retinal angiograms and MRA data sets.

Kirbas *et al.* [52], Abràmoff *et al.* [1] and Fraz *et al.* [37] surveyed methods for the vessel segmentation in medical images where the approaches studied are grouped based on the techniques used. The approaches surveyed follow two main phases: enhancement of vessel-like structures by analysing pixel features, and classification of pixels yielding a vessel-pixel segmentation approach. The material of interest for the vessel-pixel labelling method proposed in this thesis is the enhancement of vessel-like structures.

Analysis of local features of pixels, intensities for instance, can be used to estimate low-level features used to locally associate pixels to a defined vessel model. A prior analysis of the intensities of vessel pixels in retinal images suggests that the intensity profile across blood vessels may be approximated by a Gaussian curve [14, 26, 29, 60, 77, 94, 113]. Nonetheless, we cannot assume that the ideal profile across a vessel is Gaussian based only in the analysis of histogram of the studied images. The vessel model used in this thesis is discussed in Section 3.3.2 (p.39). Matched filtering methods has been developed using local curvature estimations to approximate low-level features to a Gaussian-like profile representing the cross-section of a vessel model. Some detectors based on vessel models with Gaussian-like profile across the model are described below.

Chaudhuri *et al.* [14] were the first to use a matched filter for vessel detection in retinal images [63]. Their approach is based on a set of Gaussian-like kernels applied to retinal images, where kernels are aligned along a discrete number of directions to cover all possible orientations of vessels. In addition, kernels are scaled to detect vessels at a range of diameters. The best response across the combined kernel-scale is selected as the local maximum response producing a filtered image.

Koller *et al.* [53] propose a curvilinear structure detector using derivatives to enhance edges in 2D and 3D data. A Gaussian-like filter is scaled and used to convolve the image producing a scale-space representation of the initial image. The applied filter is steerable in orientation to cope with the detection of vessels at a range of orientations. The Hessian matrix of the image—that can be estimated by convolving the image with second-order derivatives of a Gaussian function—is used to estimate the local direction in which the filter is applied, and is given by the largest negative

eigenvalue. Filter responses across a family of scales is integrated to select the best response for every pixel generating a filtered image.

Li *et al.* [61] use the Hessian matrix to detect aneurysms and micro calcifications in cerebral images. As targeted objects can be described as circular-like objects, the Hessian matrix can be used to enhance pixels where there is not a predominant local direction—contrary to the detection of line-like objects—based on the analysis of the eigenvectors. Ma *et al.* [76] use a blob detection in X-ray images based on the Hessian matrix.

Eigenvalue ratios is essential for shape modelling based on low-level descriptors. In [4, 43, 44], for instance, a set of surfaces is defined based on the eigenvalues of the Hessian matrix. As described above, the Hessian matrix has been used in medical applications to enhance blob-, line- or tubular-like structures in 2D and 3D data.

A comparison of three previously published and much-used vessel detector algorithms based on the Hessian matrix is discussed in Section 3.3. The aim of that comparison is to select a vessel detector as a base for the vessel-pixel labelling method proposed in this thesis. The work developed in Section 3.3 as part of this thesis has been published in [109].

3.3 Performance comparison of low-level vessel detection algorithms on synthetic images

A stochastic method was used to compare the performance of three much-used multi-scale vessel detectors: Frangi *et al.* [35], Sato *et al.* [106] and Lorenz *et al.* [73]. All the three algorithms calculate the eigen-decomposition of the Hessian matrix of the image at multiple scales based on the scale-space theory introduced by Lindeberg[66]. They compute some scalar measure of 'vessel-ness' at each scale and select as the final vessel-ness measure, the maximum response across all scales. Essentially, the analysed vessel detectors only differ in how the hand-crafted scalar measures are calculated from the eigenvalues of the Hessian matrix λ_1 and λ_2 in 2D data. The analysed vessel detectors are briefly described in Section 3.3.1.

Synthetic vessel images were used to measure the performance of the vessel detectors. A proposed method to generate synthetic images is detailed in Section 3.3.2. A Monte Carlo simulation was carried out to gather the eigen-decomposition of the Hessian matrix from the synthetic images that eventually allow the performance measurement of the vessel detectors. The Monte Carlo simulation is described in Section 3.3.3. Obtained results are described in Section 3.3.4.

3.3.1 Vessel-ness measure

The Frangi detector [35] computes as a measure of eccentricity $\mathscr{R}_B = \lambda_1/\lambda_2$, where $|\lambda_1| \leq |\lambda_2|$. For some scale σ, the measure of vessel-ness L_F is given by Equation 2.26 (p. 30). We used Frangi's suggestions of taking $\beta = 0.5$ and adjusting c for best results. Frangi vessel detector is detailed in Section 2.7.3 (p. 28).

Sato *et al.* [106] also sort eigenvalue by magnitude in ascending order $|\lambda_1| \leq |\lambda_2|$. The vessel-ness due to Sato [106] is defined by:

$$L_S(\sigma) = \begin{cases} -\lambda_2 \exp\left(-\dfrac{\lambda_1^2}{2(\alpha_1\lambda_c)^2}\right), & (\lambda_2 < 0) \wedge (\lambda_1 < 0) \\ -\lambda_2 \exp\left(-\dfrac{\lambda_1^2}{2(\alpha_2\lambda_c)^2}\right), & (\lambda_2 < 0) \wedge (\lambda_1 > 0) \end{cases} \tag{3.1}$$

where $\alpha_1 < \alpha_2$. We have used Sato's suggested values of $\alpha_1 = 0.5$ and $\alpha_2 = 2$. Sato's vessel detector is detailed in Section 2.7.2 (p. 27). 2.15

Lorenz *et al.* [73] defined a parameter-less vessel-ness equation. For some scale σ, the vessel-ness due to Lorenz [73] is given by $L_L(\sigma) = |\lambda_1|/|\lambda_2|$, where $|\lambda_1| \leq |\lambda_2|$.

As suggested in the analysed vessel detectors, we compute the Hessian matrix over ten linearly-spaced scales of σ=1 to 10 pixel units and take the overall vessel-ness measure as the maximum detector response across all scales. We then threshold this measure to decide a label (vessel of non-vessel).

3.3.2 Synthetic vessel images

Obtaining ground-truth data in medical image processing is an enduring problem due to the uncertainties of inter- and intra-expert hand labelling. Here we adopt the well-established procedure of using synthetic data based on a physically-realistic model of the image formation process.

Starting with an assumption of an isolated, straight vessel of infinite extent and circular cross-section irradiated with a uniform light beam normal to the longitudinal vessel direction. We assume the vessel is uniformly filled with contrast agent. As the light passes through the vessel, the intensity of the light will be reduced based on the physics of energy transmittance through objects. The intensity of the light projection—based on a monochromatic X-ray and its attenuation model—decreases exponentially as the light propagates through objects considering objects of uniform material [15]. It is, the number of photons removed (attenuation) from a light beam of N photons depends directly on N. This leads to the concept of exponential absorption: if the thickness of the object is Δt then the number of photons removed is defined by:

$$\Delta N = -\mu \Delta t \tag{3.2}$$

where μ is the absorption coefficient. Integration of Equation 3.2 produces

$$N = N_0 exp(-\mu t) \tag{3.3}$$

where N is the number of transmitted photons and N_0 is the number incident [3]. An illustration of the attenuation of a light beam as it is propagated through an object of uniform material is shown in Figure 3.1.

In terms of radiation intensity, Equation 3.3 can be written as

$$I = I_0 exp(-\alpha \ell) \tag{3.4}$$

where I is the transmitted intensity, I_0 is the incident intensity, α is the absorption coefficient and ℓ is the path length through the material (vessel)—also termed the Beer-Lambert Law.

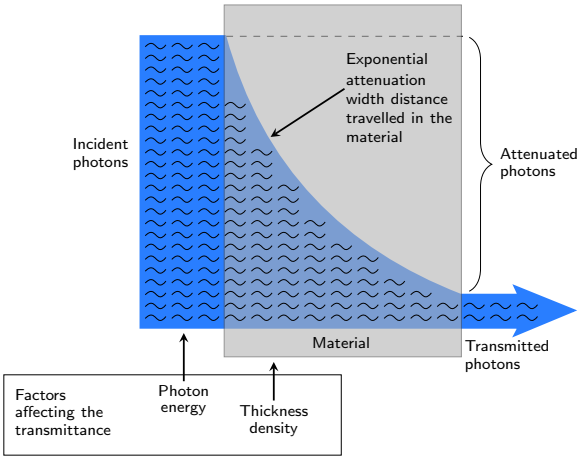

Figure 3.1: Light beam attenuation as it passes through an object of uniform material [15].

Therefore we assume the intensity profile across the vessel object is governed by the Beer-Lambert Law. Figure 3.2 illustrates the light intensity attenuation as the beams cross a uniformly filled cylindrical object, and the lower section shows the resulting intensity profile projected onto the camera's focal plane. In Equation 3.4, $\ell = \ell(x)$ where x is the spatial dimension of the vessel.

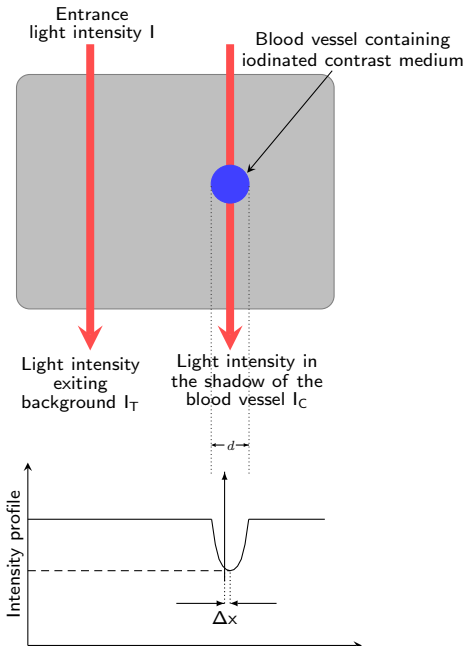

Figure 3.2: Formation of the vessel intensity model for a vessel of diameter d based on the Beer-Lambert Law [19]. The lower figure shows the projected intensity profile.

The value for α was selected to give maximum contrast at the largest vessel diameter considered while allowing $\pm 3\sigma$ 'headroom', where σ is the standard deviation of the added noised to the image, for the largest noise perturbations of the pixel values in the output image.

A distinguishing feature of the proposed work is the realistic image formation based on an illumination absorption process: previous work, for example Krissian *et al.* [55], has usually assumed the projected vessel intensity profile is Gaussian with a physically-implausible infinite region of support. Drechsler and Laura [26] used the data of Krissian *et al.* in a qualitative comparison of vessel detectors.

We have no a priori reason to suppose that a vessel will present at any particular orientation to, or displacement from the image lattice so we select a uniformly-random orientation $\theta \in [0...45°]$ and a displacement $\Delta x \in [-0.5 \text{ pixel} ... + 0.5 \text{ pixel}]$ from the notional origin in Figure 3.2. In practice, these are applied by an affine transformation of the projected intensity image above.

To account for the limitations of the imaging optics, we convolve the affine-transformed image with a Gaussian of $\sigma_{PSF} = 1$ and then add Gaussian-distributed noise of some σ_N which assumes that the dominant noise process is due to thermal noise in the camera/electronics. Finally, we quantise the pixel intensities into the range $[0...255]$ to mimic analogue-to-digital conversion in the camera. This final image containing a single vessel, as shown in Figure 3.3, is passed to one of the analysed vessel detectors.

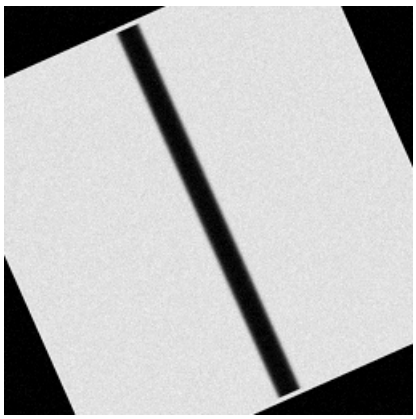

Figure 3.3: Synthetic vessel image, true Monte Carlo trial: diameter = 14.6 pixel-units; x-displacement=-0.1 pixel-units; power noise σ=2.6; and, rotation=24° from vertical direction.

In assessing a detector, we consider only the label of the central pixel of the image through which the centreline of the vessel passes. Our rationale here is that the signal-to-noise ratio is maximised at the centre of the vessel—if the vessel cannot be detected at its centre, it cannot probably be detected anywhere else across its diameter. We thus implicitly investigate the upper bound of the detectors' performance.

3.3.3 Monte Carlo simulation

Each synthetic image containing a vessel represents an independent Monte Carlo trial. To form counter-example images (*i.e.* genuine absence of a vessel) we form an image of uniform background intensity but with each pixel corrupted by noise of the same variance as the positive vessel examples.

We have repeated the above steps of generating positive and negative vessel examples in a Monte Carlo experiment with 1000 trials. Every trial has been labelled with each of the vessel detectors using various thresholds to construct receiver operating characteristic (ROC) plots. We also use the area-under-the-curve (AUC) as a summary statistic for the ROC plot.

3.3.4 Results

We have considered a range of vessel diameters ($D \in [1,3,5,7...,15]$ pixel units) and noise powers ($\sigma_N \in [5,10,15,20,25]$). Due to the large number of parameter permutations, the most representative values were selected describing the parameters as categories as follow. For vessel diameter, 1 and 3 pixel-units of diameter are regarded as narrow vessels; 5 pixel-units as medium-range; and, 15 pixel-units as big vessels. Power of noise was classified as no-noise, low- and high-noise for $\sigma_N = \{0,5,$ and $25\}$ although in practice, absence of noise is a physically unrealistic case. The selected parameters are the most representative in the detectors' performance and between which there is a more-or-less smooth variation.

For the (physically unrealistic) absence of noise (σ_N = 0) all three detectors perform 'perfectly' (AUC = 1.0) apart from the case of unit vessel width ($D = 1$) where the Frangi and Lorenz detectors are tied (AUC = 0.95) and perform slightly worse than Sato (AUC = 0.97).

Figure 3.4(a) shows the ROC plot for $D = 1$ and low noise ($\sigma = 5$) where all three vessel detectors perform to some degree although the Sato and Frangi detectors (with similar behaviour) are better than Lorenz. The straight line segments of the ROC plots are due to the discontinuities introduced by the case $\lambda_2 = 0$ in Equation 2.26 (p.

30). The detectors' behaviour is quite complex with the ROC plots crossing although there is generally little to choose between Frangi and Sato.

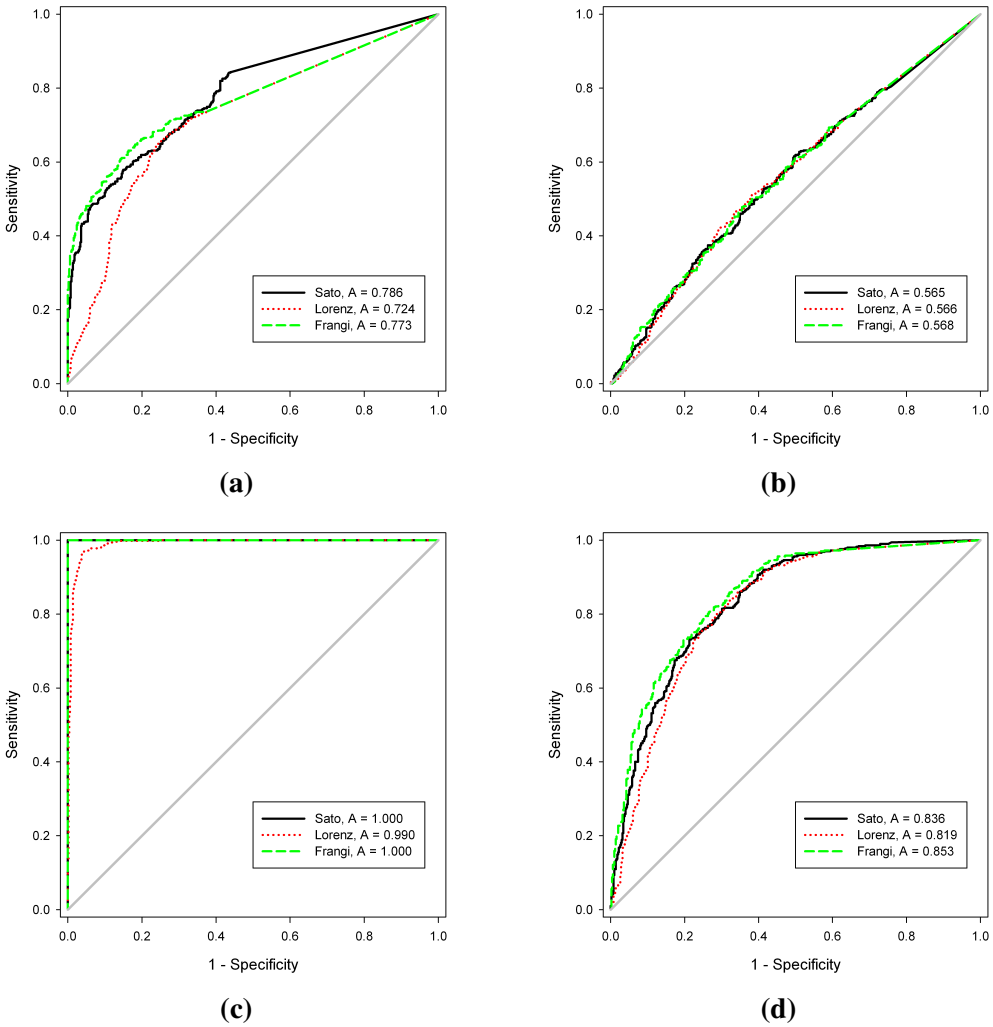

Figure 3.4: Vessel detectors' performance for small isolated and straight vessels: D=1 and (a) low-noise ($\sigma_N = 5$) and (b) high-noise ($\sigma_N = 25$). D=3 and (c) low-noise ($\sigma_N = 5$) and (d) high-noise ($\sigma_N = 25$).

For the case of high noise (Figure 3.4(b)), the performance of all three detectors reduces to little better than random guessing (the 45° line) might be expected since the signal-to-noise (SNR) ratio becomes very low for this case. Since we have use a fixed value of attenuation coefficient (α), the SNR reduces as a function of reducing vessel diameter, hence small vessels are intrinsically harder to label.

For $D = 1$ and 3, and $\sigma_N = 25$ (high noise) shown in Figures 3.4(b), (d), there is little to choose between the performances of all three detectors. There is, however, an interesting transition between $D = 3$ and $D = 5$ (see Figure 3.4(d) and 3.5(b)) where the Frangi and Sato algorithms begin to out-perform Lorenz, with Frangi slightly ahead

of Sato, a trend which continues up to large diameters. Figures 3.5(c) and 3.5(d) show

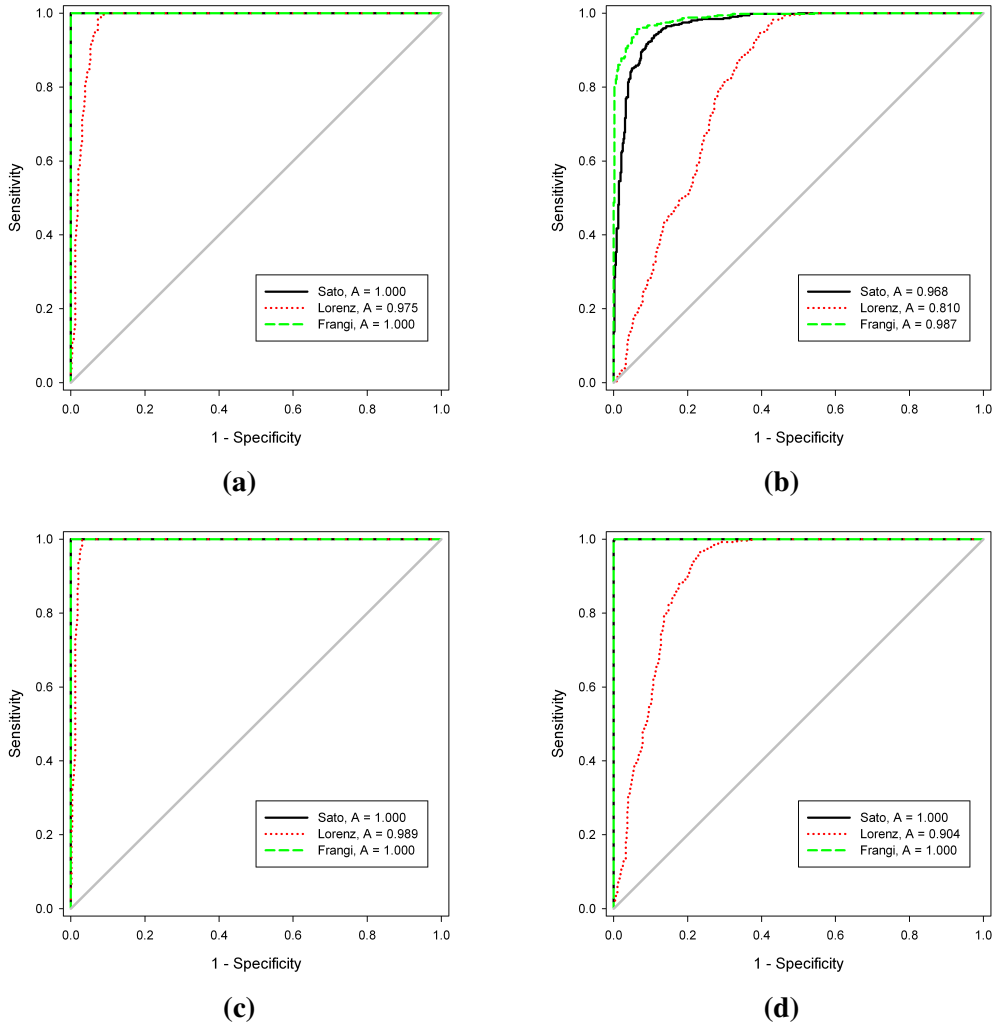

Figure 3.5: Vessel detectors' performance for medium-range and big isolated and straight vessels: D=5 and (a) low-noise ($\sigma_N = 5$) and (b) high-noise ($\sigma_N = 25$). D=15 and (c) low-noise ($\sigma_N = 5$) and (d) high-noise ($\sigma_N = 25$).

the corresponding plots for $D = 15$. At this stage, the Sato and Frangi algorithms both perform 'perfectly' (AUC = 1) regardless of noise power. The Lorenz detector, however, is clearly inferior, even for low noise powers.

As a summary, Figure 3.6 shows the AUC statistic vs. vessel diameter D. The region between these two pairs of curves (low noise and high noise) delineates the useful operating envelope of the two detectors.

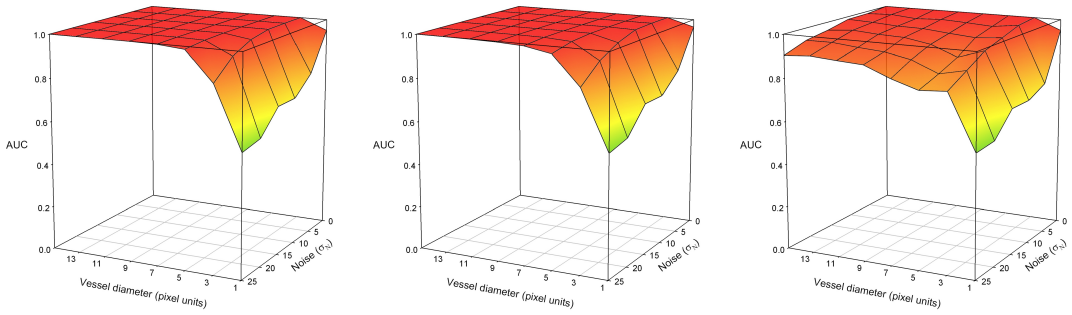

(a) **(b)** **(c)**

Figure 3.6: AUC summary plots for vessel diameter D vs. noise $\sigma_N = \{5, 10, 15, 20, 25\}$: (a) Frangi, (b) Sato, and (c) Lorenz.

3.4 Discussion

Vessel segmentation methods rely on the imaging modality as images can be analysed due to features such as intensities of pixels. In the reviewed approaches, there are two main phases: enhancement of vessel-like structures and segmentation. The first phase is usually taken as analysis of the local-features to—at some extent—label pixels as vessel and non-vessel. In the enhancement process—based on the analysis of local curvature, the studied approaches regard the cross-section curvature profile of an ideal vessel model being Gaussian based on the histogram distribution of images used as calibration.

We propose a vessel intensity-profile model based on an illumination absorption-based imaging process where the intensity of pixels is reduced exponentially as light beams pass through a uniformly filled cylindrical object representing a vessel structure. Three vessel detectors, Frangi *et al.* [35], Sato *et al.* [106] and Lorenz *et al.* [73]—all of them based on the analysis of the Hessian matrix and scale-space representation—were tested using Monte Carlo simulations and generated synthetic images. The performances of Frangi and Sato detectors are clearly better. These methods seem to offer some promise for segmenting fine vessels if combined with a contextual approach (*e.g.* Markov random fields).

The results obtained are limited to straight, isolated vessels. Qualitative observations suggest the Frangi detector does not perform well at vessel bifurcations and junctions since there is not a clearly dominant local primary curvature [26].

3.5 Conclusions

In this chapter, some of the much-used vessel segmentation approaches were reviewed. The approaches are based on the analysis of low-level features to locally match every visited pixel into a vessel model.

From constructing a physics-based model of the process by which the image of a vessel is formed in digital-subtraction X-ray angiography, we have compared the performances of the vessel detectors devised by: Frangi *et al.* [35], Sato *et al.* [106] and Lorenz *et al.* [73]. On the basis of the obtained results, the Lorenz detector is clearly inferior to the Frangi and Sato detectors between which there is little to choose for anything other than the smallest vessel diameters. Whether Frangi or Sato is better for vessels on the 1 pixel scale would seem to depend on the exact operating point.

Chapter 4

Background extraction

4.1 Introduction

Retinal images usually have large changes in illumination producing a non uniform background. This makes it difficult for vessel segmentation based on global features. Another problem is that vessel networks and the optic disc are not always located in a fixed place. In this case, segmentation over fixed-size regions does not guarantee a uniform intensity background. Figure 4.1 shows the use of the Otsu [87] thresholding method based on global features and using fixed-size regions in a greyscale retinal image. Changes in illumination across the image are evident suggesting it would be difficult to perform vascular network segmentation.

The label of a given pixel belonging to the vessel networks can be estimated using a probabilistic approach. This membership value—also termed *posterior probability* in a Bayesian framework—is based, among other parameters, on prior knowledge: proportion of vessel pixels to non-vessel (background) pixels. The prior probability

(a) **(b)** **(c)**

Figure 4.1: Thresholding with Otsu's method [87]: (a) Greyscale retinal image. Thresholding using (b) global histogram and (c) based on fixed-size regions of 20×20 pixels.

involves the estimation of the number of vessel pixels in the image. In order to accurately estimate this probability, a method to remove background pixels and enhance vessel networks is proposed in this chapter.

In retinal images, vessel pixels have lower contrast than the background. Enhancement of the intensities of vessel pixels can be used to estimate the background behind those structures. Thus, the background behind vessel pixels can be estimated by analysing a region surrounding a treated pixel. This method yields a vessel network segmentation by subtracting the estimated background from the input image. Post-processing algorithms can be used to compute the density of the enhanced pixels as a statistical analysis to estimate the prior probability to be used in a Bayesian approach. As mentioned above, the prior probability is essential to estimate the posterior probability of a given pixel belonging to the vessel network in an image. The proposed probability labelling method based on a Bayesian approach is detailed in Chapter 5.

A local background estimation motivated by the Savitzky-Golay filter [107] for smoothing of signals is proposed in this chapter. Savitzky-Golay used statistical methods to smooth data to reduce the effect of noise. The fundamental notion is to fit a polynomial function to a local data set and select the one giving the best fit based on a defined metric. The proposed novel insight here is to treat the foreground as undesired objects. Background pixels in the image are regarded as inliers and those in the vessel networks and other objects as outliers. Here, the proposed method aims to remove the vessel pixels allowing a smooth background estimation.

The estimated background is given by replacing the initial value of a pixel with a polynomial function based on the statistical method used. Least Squares (LS), for instance, aims to fit a polynomial to a set of data points by minimising the Sum of Squared Errors (SSE) [58]. The error or residual value is defined as the difference between the data point and the estimated value given by the selected polynomial. For Linear Least Squares (LLS), the residual formulation is described in Equation 4.1 where $i = 1, \ldots, m$ data points; y_i is the data point response; and, β_0 and β_1 the coefficients of a linear polynomial.

$$r_i(x) = y_i - (\beta_0 - \beta_1 x_i) \tag{4.1}$$

The optimisation problem is given by Equation 4.2, where β_0 and β_1 are the coefficients of the polynomial giving the best fit. This method is efficient when data points are normally distributed without outliers. Nonetheless, the performance is readily affected by the presence of aberrant data points or outliers. In Figure 4.2(a) a set of 1D data points is plotted, and the LLS fitting is severely affected by the two outliers marked by the open bullets. Hence, other methods are used for better results.

$$min\ SSE = \sum_{i=1}^{n} ((y_i - (\beta_0 - \beta_1 x_i))^2 \tag{4.2}$$

RANdom SAmple Concensus (RANSAC) [34] and Least Median Squares (LMS) [100] are used for robust regression analysis and outlier detection [78]. The idea is simple: in 1D, for instance, two elements from a dataset are randomly selected defining a line that is *ranked* using a metric. RANSAC, for instance, ranks the line by the number of data points falling within a distance threshold—inliers. If the number of inliers satisfies a condition, RANSAC returns the tested line as a good model. The process can be repeated on a number of iterations to select the best ranked model. In Figure 4.2(b) the line formed by the data points a and b is ranked by the number of data points falling within the distance marked by the dotted lines. A disadvantage of RANSAC is that it requires *a priori* knowledge to define the threshold for inliers.

An alternative method is the Least Median Squares (LMS), which ranks a line (the same line used for the RANSAC example) with the median of residual values between a set of data source points and the equation corresponding to the tested line in the example. In LMS, a number of samples or iterations (lines in the example) are

used to select the best fit based on the selected type of score, for LMS is the smallest median residual value across all the testes lines.

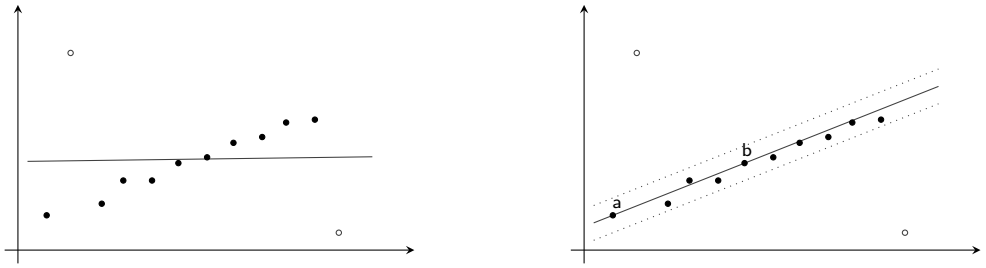

Figure 4.2: Robust line estimation. The filled points are inliers and open bullets outliers. (a) Least Squares is severely affected by the two outliers. (b) In the RANSAC algorithm, the line from **a** to **b** is supported by the number of points within the threshold distance denoted by dotted lines [58].

Owing to the poor performance of LS and the prior information required to determine settings for RANSAC, LMS was used as an optimisation method to estimate the background behind the vessel networks. This background estimation conveys essential information used in Chapter 5 for vessel network segmentation using a probabilistic approach.

4.2 Fitting Least Median Squares (LMS)

Least Median Squares was introduced by Rousseeuw [100] and is mathematically simple but is a robust outlier detector. The idea of this algorithm is to select a subset of data points—also called a sample—with a random method, and fit a polynomial to this subset. The polynomial is fitted by minimising the mean of squared residual values (see Equation 4.1 for residual computation). The optimisation is to select the smallest median residual squared value using a number of samples i as shown in Equation 4.3. A limitation of LMS is its deficient performance when more than fifty percent of observations in the sample are outliers. Retinal images typically satisfy this.

$$\min_{i} \text{median}\, r_i^2 \tag{4.3}$$

A polynomial can be obtained by solving a system of linear equations that are formed by the data points. A *system* can be expressed as shown in Equation 4.4.

$$Ax \cong b \tag{4.4}$$

where A is an known $m \times n$ matrix, x is a n-vector and b an m-vector. The solution of the system is the vector x that minimises the distance between the left and right side of the system of the equation.

A system of equations is *overdetermined* when there are more equations than unknowns. That is, the dimension of matrix A is $m > n$. In that case, the solution x can be found using the $n \times n$ symmetric linear system also termed the *normal equation*, shown in Equation 4.5.

$$A^T Ax = A^T b \tag{4.5}$$

The vector x is a unique solution when the columns of matrix A are linearly independent, which makes $A^T A$ invertible. Thus,

$$x = (A^T A)^{-1} A^T b \tag{4.6}$$

If A is a non-square matrix, it does not have an inverse. In that case, the pseudo-inverse of A can be estimated using Singular Value Decomposition (SVD). The singular value decomposition of a general $m \times n$ matrix A has the form:

$$A = U \Sigma V^T \tag{4.7}$$

where U is an $m \times m$ orthogonal matrix, Σ is an $m \times n$ diagonal matrix—where the diagonal elements contain the singular values of A, and V is an $n \times n$ orthogonal matrix. The SVD of the pseudo inverse for a general matrix A is defined by Equation 4.8.

$$A^+ = V \Sigma^+ U^T \tag{4.8}$$

where Σ^+ is estimated by transposing and inverting all non-zero entries.

Since A in Equation 4.6 may be a non-square matrix, its inverse can be estimated using the SVD method by solving the Equations 4.7 and 4.8, where the matrix $A^T A$ is

taken as the definition of general matrix A in Equation 4.7. Therefore, the solution x (Equation 4.6) giving the minimum least squares is found by

$$x = (V\Sigma^{+}U^{T})A^{T}b \tag{4.9}$$

where V, Σ and U are the SVD elements of the square matrix $A^{T}A$.

Eventually, the residual value for each element in the LMS sample is given by the difference between the sample's observations and the estimated value from the solution x.

4.2.1 Number of samples

The number of samples to select the best polynomial can be estimated from the probability that a chosen sample is free of outliers. That is, the pixels forming an outlier-free sample makes the fitted plane return small residual values. This can improve the smoothness because the selected polynomial is based on the median of those residual values. The data space from where the LMS samples are formed and the sample size are discussed in Section 4.2.2.

If the data points are uniformly distributed, the probability p, that at least one of the random samples is free of outliers can be taken as 0.99. Furthermore, if the distribution of the outliers is known, the probability ε that a data point is an outlier can be defined as $1-\omega$, where ω is the probability that a data point is an inlier. Therefore, the least number of samples required to select a sample free of outliers is given by Equation 4.10 if the outlier distribution is known. For the problem in Figure 4.2 on page 50, the sample size $s = 2$ as only two data points are randomly selected to fit the finite collection of data points to a straight line. The probability $\varepsilon = 2/12 = 1/6$ as two of the data points are outliers. Thus, the estimated minimum number of samples in the discussed LMS line-fitting problem is four.

$$N = \frac{log(1-p)}{log(1-(1-\varepsilon)^{s})} \tag{4.10}$$

Some examples of N number of samples for $p = 0.99$ and a given s and ε are presented in Table 4.1.

Table 4.1: The number of samples required to ensure, with a probability p=0.99, that at least one sample is outlier free for a given sample size s and a proportion of outliers ε [58].

Sample size	Proportion of outliers ε						
s	5%	10%	20%	25%	30%	40%	50%
2	2	3	5	6	7	11	17
3	3	4	7	9	11	19	35
4	3	5	9	13	17	34	72
5	4	6	12	17	26	57	146
6	4	7	16	24	37	97	293
7	4	8	20	33	54	163	588
8	5	9	26	44	78	272	1,177

4.2.2 Selection of sample space

An LMS sample is formed by a subset of data points—also called observations—within a defined space. Since LMS aims to estimate the background based on neighbours, the sample space can be defined as a region encompassing the pixel being tested. If data points are uniformly distributed in the space, the observations can be chosen with a random function to form an LMS sample. The aim of this method is to have a representation of the data distribution. Nonetheless, due to similarities between data points, a sample may be useless if the selected observations cover a small region in the sample space. In order to avoid this, data points are grouped in blocks, which can be randomly selected.

This technique of clustering data points is also called bucketing [16, 49, 122]. The idea is to divide the sample space into non-overlapping blocks to spread the observations across the space [49]. A bucket size can be defined in several ways. The sample space can be arbitrarily divided along one or several dimensions [16]; however, fixed-size buckets are suggested in [122] as shown in Figure 4.3. Since buckets or blocks are regarded as uniformly distributed, Equation 4.10 remains valid. As an optimisation method, an LMS sample can be formed by non-repeated blocks.

To smooth 1D signals, for instance, the sample space can be defined as a set of data points before and after the location being tested as shown in Figure 4.4. This

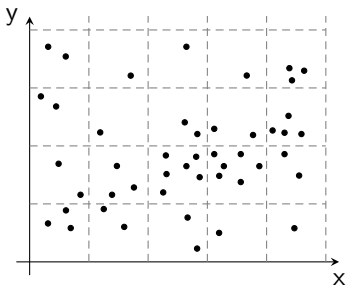

Figure 4.3: Buckets dividing data space and gathering data points. [16]

principle can be extended to 2D signals, where the sample space can be defined by a region of $m \times m$ pixels enclosing the pixel being tested. In the bucketing for a 1D signal, the sample space is divided into blocks of n-pixels and into $n \times n$ pixels for a 2D signal.

The method to construct an LMS sample for a 1D signal linear-fitting problem is shown in Figure 4.4. The image illustrates a cross-section view of the ideal intensity profile in a retinal image, where the intensity is governed by light-beams passing through a single and straight vessel. The signal profile can be described as Gaussian-like function as suggested in [62, 121]. Notice that the signal is not corrupted in this example. The location being tested correspond to the lowest value in the continuous signal. The data points forming the constant horizontal—background intensity—are regarded inliers and those in the Gaussian profile as outliers. Thus, the aim of the LMS is to enhance the intensity of the tested location to make the whole signal more uniform. The sample space is defined as a set of locations delimited by the two pairs of vertical dashed lines. A number of non-overlapping blocks of n-data points are distributed covering the space. The signal has been sampled for this fitting example: Eventually, a set of non-duplicated blocks is randomly selected to form an LMS sample.

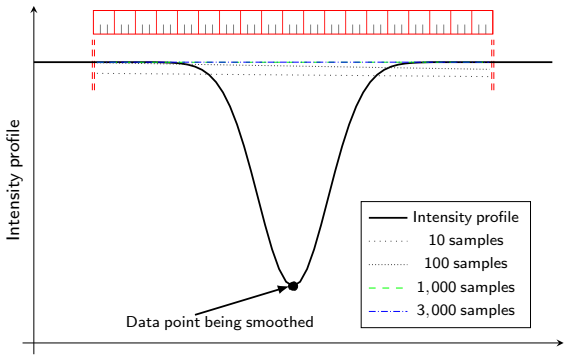

Figure 4.4: Least Median Squares sample formation to smooth 1D signals.

The method described above can be extended in order to smooth 2D signals. The sample formation process is shown in Figure 4.5 from bottom to top in three key stages: First, the pixel at which the background estimate is sought is defined. Then, the sample space is defined as a $m \times m$ region enclosing the pixel and the space is divided into blocks of $n \times n$ pixels. Finally, the contents of every randomly selected block—$n \times n$ pixels—become the LMS sample.

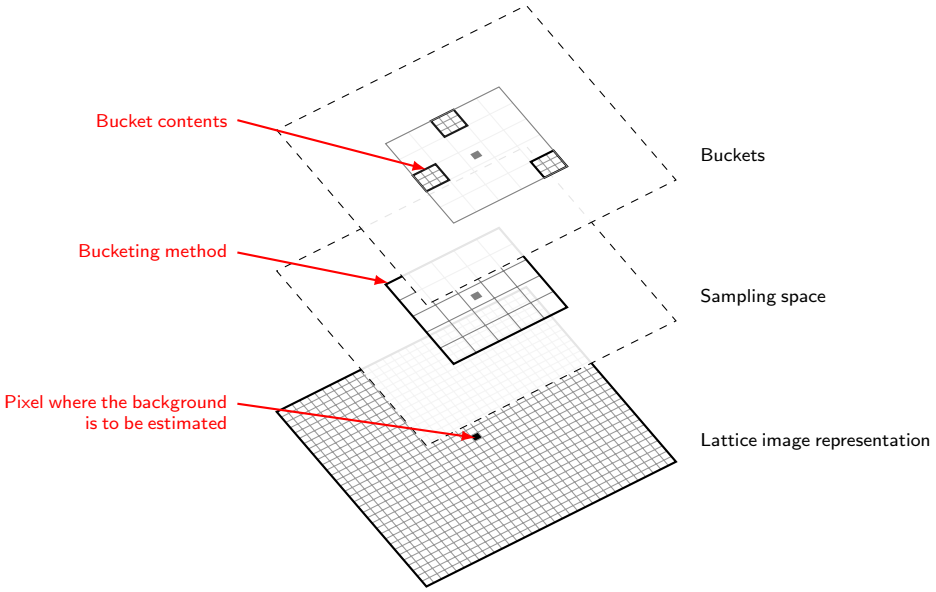

Figure 4.5: Least Median Squares sample formation to smooth 2D signals.

For the example of Figure 4.4, the LMS method was carried out to estimate the background at the indicated location. An LMS sample was defined as a set of three buckets of three data points. The proportion of outliers was regarded as an unknown parameter. The line-fitting results for a set number of LMS samples were compared based on the estimated Minimum Median Squared Error (MMSE) (see Table 4.2).

Table 4.2: LMS to smooth a 1D signal with a Gaussian-like intensity profile of Figure 4.4

LMS samples	MMSE	Abs(Estimated - Expected)
10	0.995	1.141
100	0.017	0.345
1,000	0.000	0.006
3,000	0.000	0.000

As the number of samples increases, the Minimum Median Squared Error (MMSE) and the difference between the estimated and the expected value or *ground truth* are reduced. If the data points in the Gaussian are regarded as outliers (29 from

the 57 data points), the minimum N number of samples required to find an outlier-free sample is near 3000 (see Equation 4.10, p. 52). The best fitted polynomials for the LMS samples listed in Table 4.2 are shown in Figure 4.4. It can be seen as the tested polynomials approach the background intensity as the number of samples increases. The estimated background value at the required location is given by replacing the measured image intensity with the estimated value from the fitted polynomial. The above process is then repeated for every pixel in the image. This procedure is similar to the Savitzky-Golay procedure.

As described in Section 2.2 (p. 7), red-free imaging modalities increase the contrast between vessel structures and the background. The DRIVE database [110], however, contains JPEG (Joint Photographic Experts Group) compressed colour images. JPEG compression is one of the most common image format used for medical imaging [31, 120] since it compresses images in size without compromising—at some extent—the quality of images.

Using a monochromatic version of the original eye fundus image can enhance vasculature structures due to suppression of other colours. Approaches such as [36, 84, 97, 101, 104, 119] suggest using the green component of the RGB colour space since it presents the largest contrast between vessels and the background in the mentioned database. Figure 4.6 shows the decomposition of an original image into the R, G and B components of the RGB colour space, and a greyscale version given by the I component of HSI colour space. The effect of using a monochromatic version can be seen in the image, where various vessel structures become more or less visible.

Since the green component presents the largest contrast between vessel structures and the background, the background estimation and subsequent processes are based on that version of the original eye fundus image.

The estimated background of some retinal images from the DRIVE database [110] are shown in Figure 4.7. In order to describe the local fitted behaviour, the estimated background was subtracted from the input image (see Figure 4.7(e), (f)). A negative difference between the input and the fitted values is obtained when the fitted values exceed the input image. Conversely, a positive difference is computed when the estimated background values remain below the input image. Hence, large negative

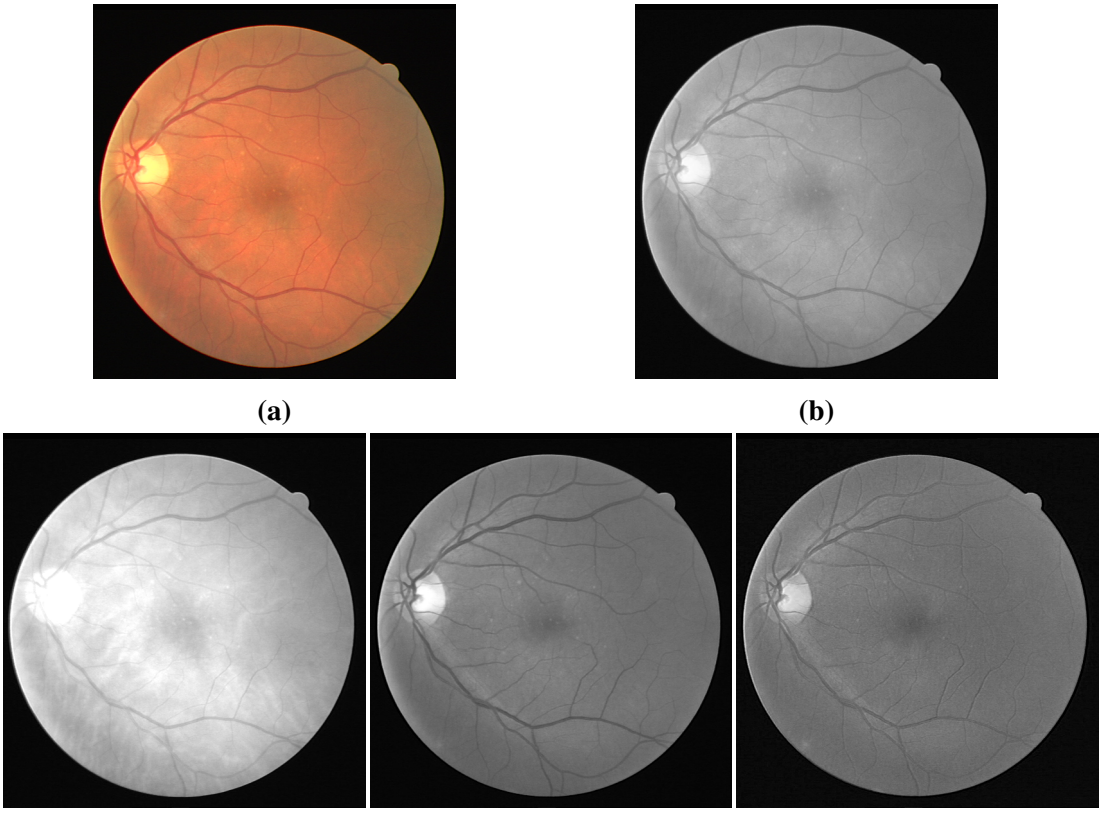

Figure 4.6: RGB decomposition of an eye fundus image from the DRIVE database [110]: (a) Original image; (b) Greyscale I=(R+G+B)/3 (RGB-to-HSI conversion); (c) Red, (d) Green, and (e) Blue component.

values are shown as dark and large positive as a bright intensity (see Figures 4.7(e), (f)).

In the contrasted images shown in Figures 4.7(e), (f), the transition from inside the optic disc to the background shows an effect: large positive values inside and large negative out the optic disc. It is important to mention that this unwanted behaviour is described in Section 2.3 (p. 14). When the image is processed, our LMS-based fitting method implicitly assumes that the background intensity is locally a smooth function. Nonetheless, the reflex of the eye tissue (as described in Section 2.3) makes the changes of intensity rapid, forming an edge-like behaviour. The discontinuity of the optic disc edge affects the plane-fitting. For the pixels inside the optic disc, fitted values are below the intensity in the input image and the opposite effect occurs with pixels from the background. An enhancement method described in Section 4.3 was developed to improve the background estimation in the region on the optic disc edge.

The Minimum Median Squared Error maps are shown in Figures 4.7(g), (h). A

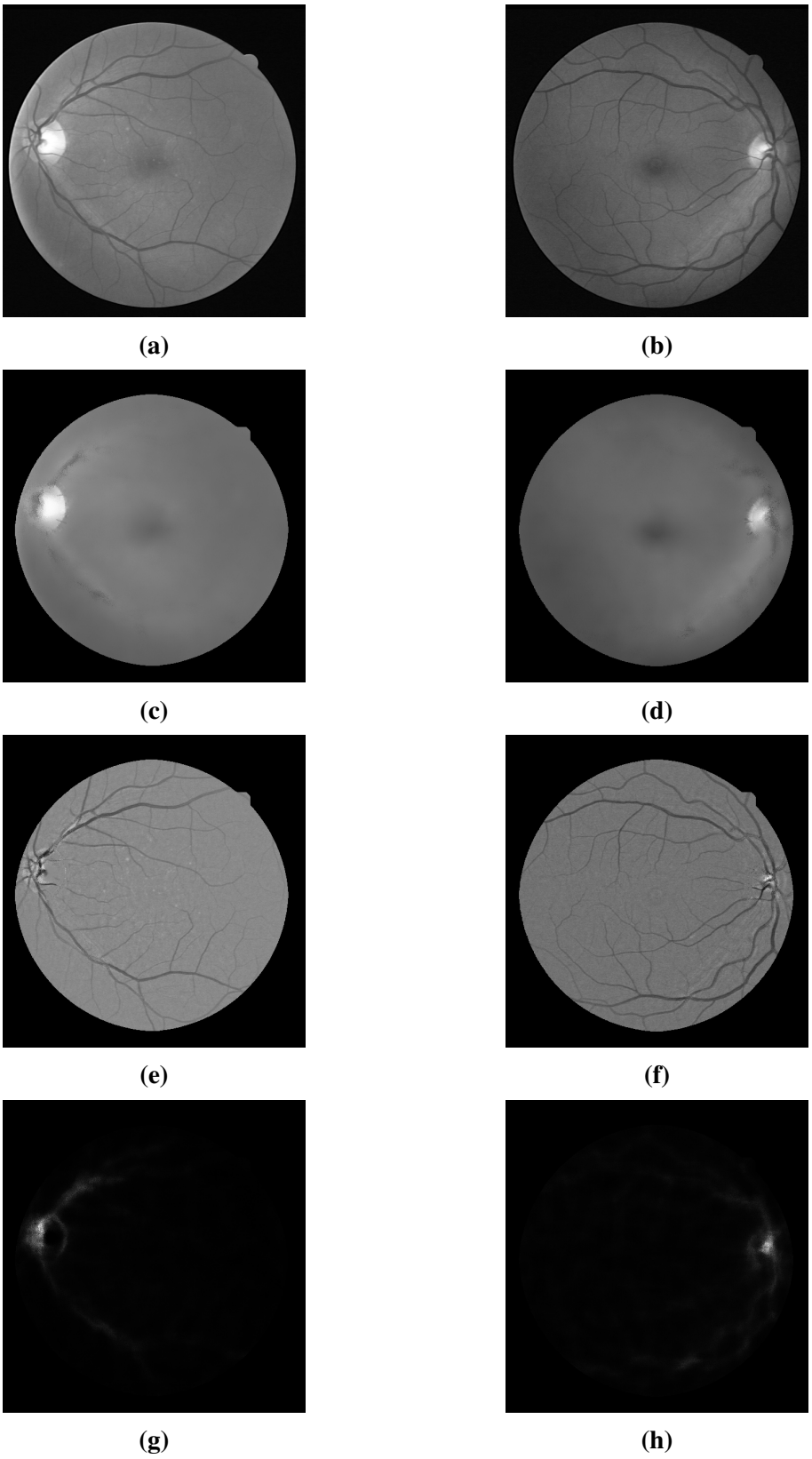

Figure 4.7: Background estimation for retinal images from the DRIVE database [110]: (a), (b) input images (Green component of the original image); (c), (d) locally estimated background; (e), (f) background subtraction; and, (g), (h) Minimum Median Squared Error (MMSE).

large residual suggests that the best fitting polynomial was affected by the proportion of outliers. Regions surrounding large vessels and the optic disc show a considerable residual values. Increasing the sample space to incorporate more blocks of pixels from the background may reduce the effect; however, the plane-fitting performance relies on the background being locally representable as a linear function. There is thus a trade-off between patch size and outlier rejection.

4.3 Optic disc refinement

The performance of the proposed background estimation method is affected when the sample space contains a large proportion of outliers. Hence, a background enhancement method was developed to improve the estimated background in regions with a large MMSE. At the optic disc boundaries, for instance, the sample space covers a region with pixels from each side of the optic disc edge. The intensity of those pixels produce a step-like function that makes the linear function difficult to fit. Since the LMS plane-fitting is linear, it compresses upper values and enhances the lower ones. Figure 4.8 shows a comparison between the input data and the estimated background. The data plotted belong to a given row crossing the optic disc region. The data were taken from the images in Figure 4.7(a) and the row set to 255.

The plot in black depicts the intensity profile in the input image and the plot in green the estimated background. The signal rises rapidly after column 50, remains above 200 in intensity and falls quickly before column 130 on the x-axis. Pixels in the mentioned region are those falling in the optic disc.

As shown in the plot of Figure 4.8, in general, the LMS plane-fitting compressed the intensity of pixels in the optic disc and enhanced those in the background. The influence of this effect on further analysis of the retinal image is described in Section 4.4. In order to reduce the effect, a fitting refinement method was implemented and applied to enhance the background estimation in the optic disc edge region. Like the LMS plane-fitting, the proposed refinement is based on an LMS linear fitting approach. In that case, a piecewise function was used to re-estimate the background inside and outside the optic disc separately. The condition of the piecewise function is outlined by the optic disc edge.

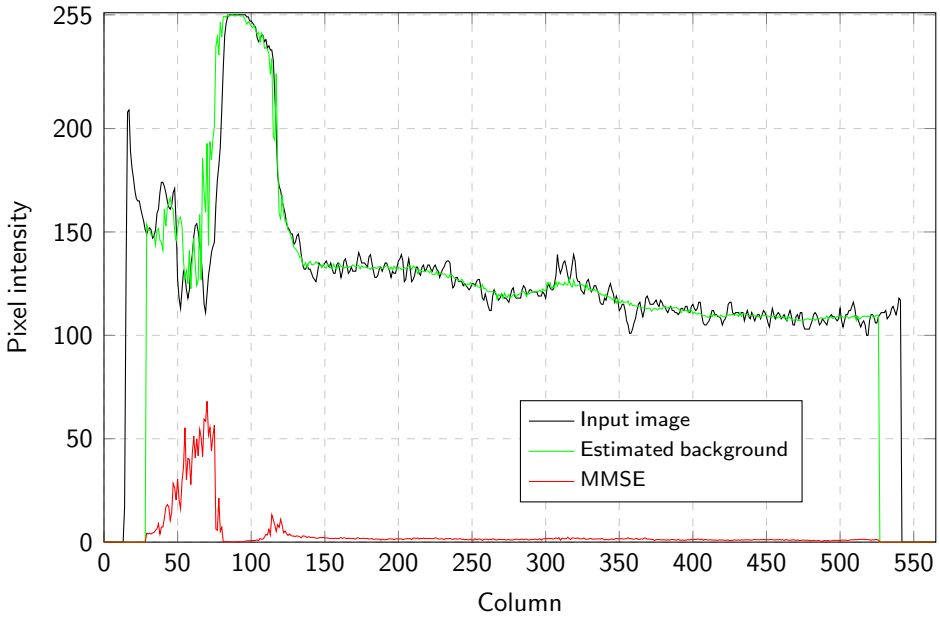

Figure 4.8: Input and estimated-background intensity profile along row 255 crossing the optic disc region from Figure 4.7(a).

Other approaches have been developed to automate the location and segmentation of the optic disc based on its shape, colour and size. Welfer *et al.* [115], for instance, propose a method based on the vascular tree as reference to initiate an adaptive method that eventually reaches the optic disc boundaries. Giachetti *et al.* [39] propose an ellipse-fitting method using a snake-based contour refinement method. The method proposed by Chrástek *et al.* [17] is based on active contours and the Hough transform to converge into an ellipse-like shape. Fiorini *et al.* [33] suggest that the optic disc has a more relevant information in the *red* component for retinal images in the RGB colour space, which allows the optic disc detection by analysing this component. Bhalerao *et al.* [9] suggest a mixture of Gaussians model to locate the optic disc on the *green* component—RGB colour space—on colour fundus images. A pre-processing stage involves a low-pass filter (to blur the components in the image) and normalisation of the image. Osareh *et al.* [86] propose a snake-based contour converging into the desired optic disc shape using retinal images in the Lab colour space.

Since the refinement region only covers a section of the optic disc boundaries, the to-be treated region was, for simplicity, outlined by manually drawing an arc segment along the optic disc edge as shown in Figure 4.9(a). The automated location of the refinement area is discussed in the future work section of Chapter 6.

For every pixel forming the drawn arc segment, the background estimation was carried out using an LMS fitting method using a piecewise function. Since the refinement method aims to smooth pixels near the optic disc edge, the sample space covered a region containing pixels from inside and outside the optic disc. The orientation of each pixel in the arc segment was used as a reference to define the 1D sample space as follows: when the orientation from the y-direction is $\pm 30°$, the sample space covers a set of locations along a vertical line crossing the pixel on the arc; when orientation is $\pm 30°$ from the x-direction, the sample space is along the horizontal; and in any other case, follows a $\pm 45°$ direction. Figure 4.9(b) shows the sample space for each pixel forming the arc segment shown in 4.9(a). The orientation of the sample space (90°, 45° or 0°) is given by the orientation of the pixel on the arc segment.

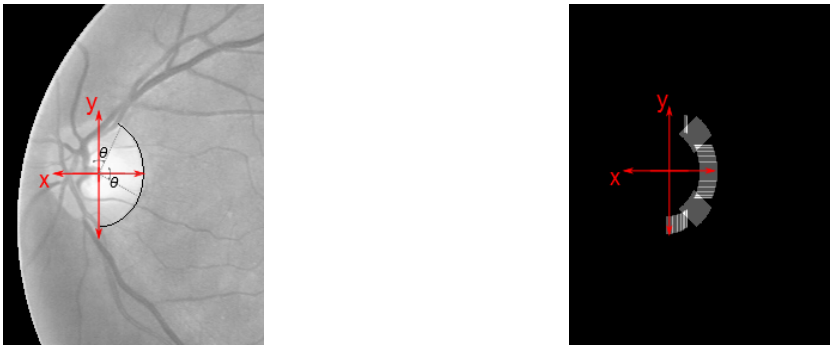

(a) **(b)**

Figure 4.9: Optic disc refinement region and LMS linear-fitting sampling space. (a) Arc segment manually defined along the interior section of the optic disc edge; (b) sample space for every data point forming the arc segment to re-estimate the background near by the optic disc's edge.

As described above, a piecewise function was used for the background refinement in the optic disc edge. The function was formed by two intervals where each interval was a quadratic polynomial outlining the inside and the outside section of the optic disc using the defined sample space. The two intervals of the piecewise function are separated by the optic disc's edge as follows: pixels in the sample space falling within the optic disc are fitted to a negative parabola and those outside the optic disc (falling in the background region) to a positive curve.

Some changes in the LMS method were adapted for this refinement. The LMS sample size for instance, was reduced to the minimum number of data points needed to build a parabola—three pixels from the sample space on each side of the optic disc

edge. The LMS linear-fitting for each interval of the piecewise function were carried out separately. Finally, the estimated background of pixels on the optic disc's edge is given by the average of the two selected quadratic polynomials—fitting the inside and outside the optic disc's edge.

The refinement method for the signal plotted in Figure 4.8 (p. 60) is shown in Figure 4.10. Since the plotted data belongs to a row-pixels crossing the optic disc in a retinal image, there is only one location marked as optic disc's edge. In the Figure 4.10, the solid black point is the to-be treated pixel on the optic disc edge. The sample space—following 0° due to the "edge pixel orientation"—is delimited by the grey dashed boxes containing pixels from inside and outside the optic disc region; and, the best fitting polynomials are shown in red and green plots for their corresponding inside and outside LMS fitting process. The re-estimated background on the optic disc edge—solid blue point—is given by the average of the two polynomials at that point. Results of the refinement method for the input image in Figure 4.9(a) is shown in Figure 4.11.

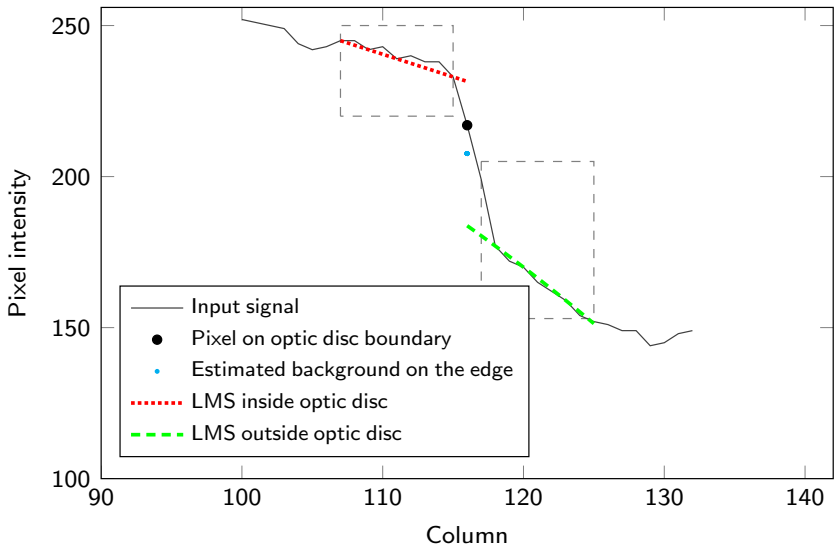

Figure 4.10: LMS linear fitting using a piecewise function to smooth the sharpness of the transition from one side to the other of the optic disc edge. The estimated value on the edge is given by the average of the two polynomials.

In order to show the results of the refinement method, the MMSE before and after the enhancement method were compared. The MMSE of the 142 pixels forming the arc segment are shown in Figure 4.12. As shown in the figure, the residual values

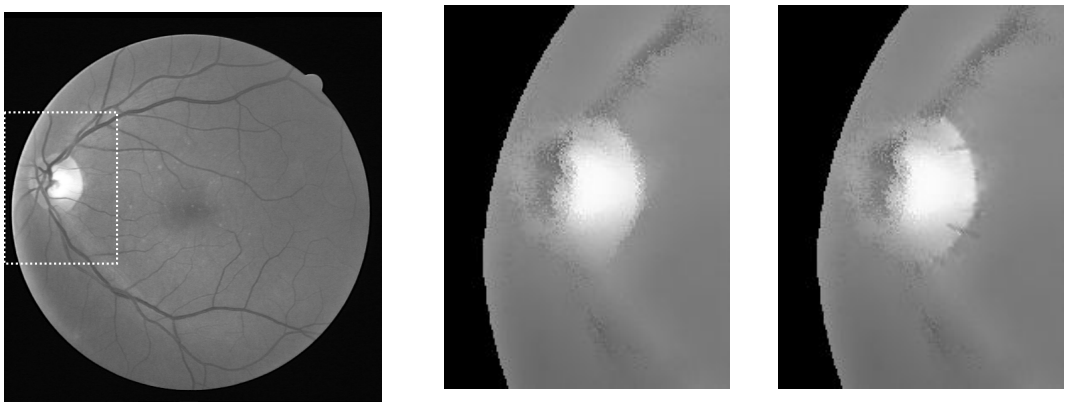

(a) (b) (c)

Figure 4.11: Background re-estimation along the optic disc edge band. (a) Input image. (b) Image before the optic disc refinement. (c) Optic disc boundaries enhanced.

given by the first LMS plane-fitting approach were reduced to near zero using the proposed refinement method.

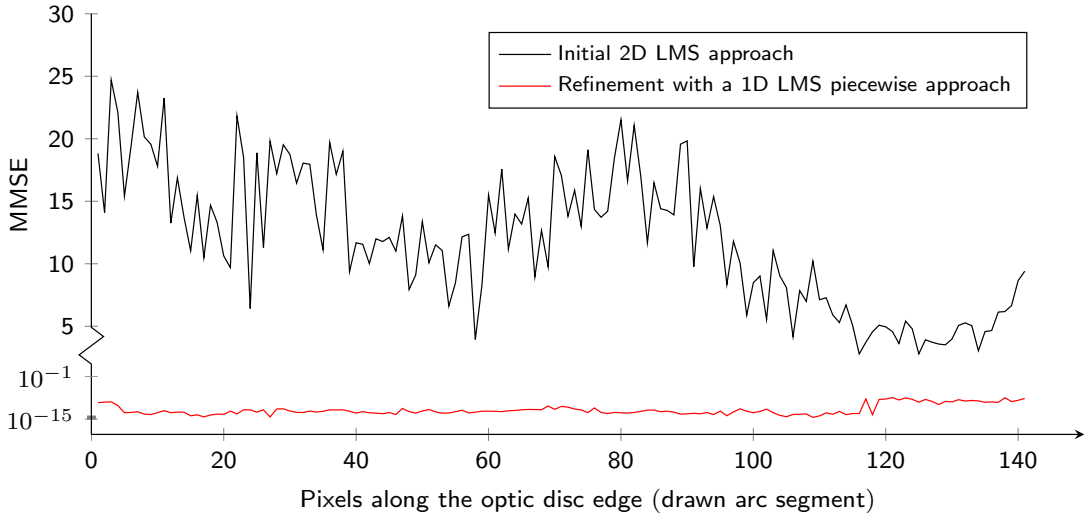

Figure 4.12: Minimum Median Squared Error comparison before and after the optic disc refinement.

4.4 Post-processing

The proposed background estimation method allows the vessel structure enhancement by subtracting the estimated background from the input image as shown on Figure 4.7(e), (f) (p. 58). Segmentation methods can be used to cluster pixels in either vessel or background to estimate the area covered by vessel networks as a statistical analysis of the image. Thresholding, for example, is used to separate object pixels from the

background pixels based on intensity. Since pixels can take only one of two labels {background, vessel}, their classification can be based on the distribution of the intensity values across the image to find the threshold. An unsupervised thresholding method can be used for the automatic threshold selection for any given image.

In the next section, the Otsu [87] method is described as it was used to separate the vessel pixels from the background. In some cases, the estimated threshold misclassified background as vessel pixels and conversely. In order to reduce this effect, small groups of pixels were removed as they were regarded as noise in the segmentation process. The latter process is described in Section 4.4.2

4.4.1 Thresholding

The Otsu [87] method analyses the histogram of image intensities to find, in the ideal case, a deep and sharp valley separating two peaks representing objects and background in a two-class image. The global optimum threshold is found in the region where both peaks are separated as shown in Figure 4.13(a). Thresholding can be extended to work with more than two clusters of pixels as illustrated in Figure 4.13(b) where two thresholds are used to cluster pixels in three groups. Nonetheless, a single threshold is adequate for the vessel network segmentation in this work.

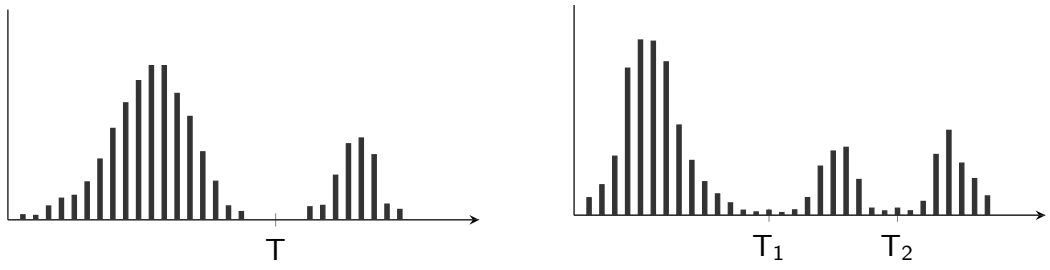

Figure 4.13: Grey-level histograms that can be partitioned by (a) a single threshold, and (b) multiple thresholds [40].

On the grounds that Otsu is based on a histogram distribution, the contrast image—estimated background subtracted from input image—is quantised into the

range $[0\ldots255]$ greylevels. A thresholded image $g(x,y)$ is a binary image defined by applying Equation 4.11 at every grey-level pixel.

$$g(x,y) = \begin{cases} 1 & : f(x,y) > \mathsf{T} \\ 0 & : f(x,y) \leq \mathsf{T} \end{cases} \tag{4.11}$$

where $f(x,y)$ is the grey level at point (x,y) of the processed image and T is the threshold. Objects are usually defined as 1 and background as 0.

The segmentation method using the Otsu threshold was applied to the contrast images before and after the optic disc refinement to show the enhancement gained. Before the optic disc refinement, the Otsu method classified pixels near the optic disc edge as objects as shown in Figure 4.14(a). This labelling suggests that the difference between the input image and the estimated background was large in size and with a negative sign as it occurs. The 'halo' effect was reduced with the optic disc refinement discussed in the previous section and results are shown in Figure 4.14(b).

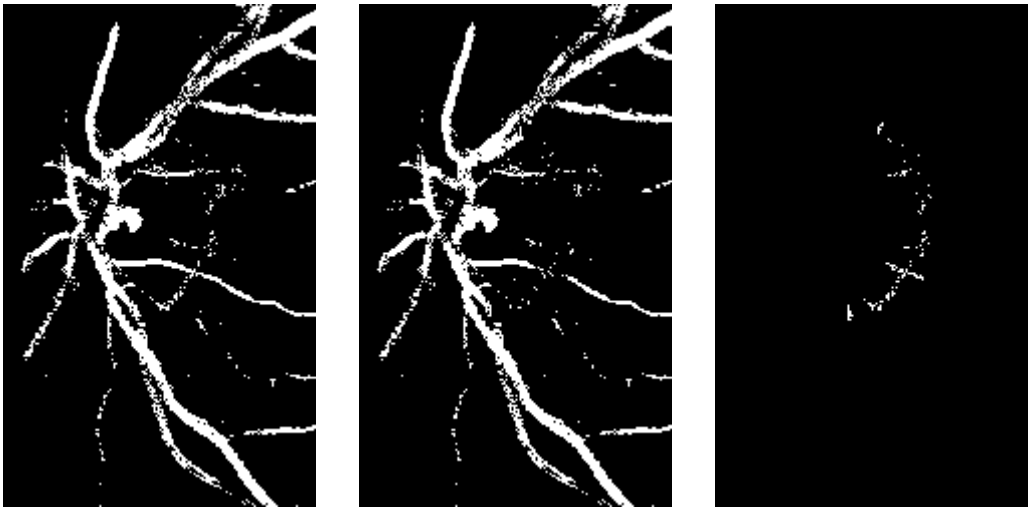

(a) **(b)** **(c)**

Figure 4.14: Global threshold Otsu in the optic disc edge band: (a) using the LMS plane-fitting approach; (b) after the optic disc refinement with an LMS linear fitting, and (c) pixels removed ((a) - (b)).

Small unwanted 'blobs' can appear after the thresholding due to variations in the difference between the input image and the estimated background. Analysis and operations over binary images can be used to remove those blobs, regarded as noise. In the next section, the method used to remove those blobs is detailed.

4.4.2 Detection and removal of blobs

Algorithms for analysis of binary images are used to perform many tasks, such as recognition, localization and inspection [108]. Morphological operators can be used to remove small blobs as these operators erode a defined number of pixels from the contour of the white components in an image. Vessel networks, however, can be affected and in some cases, small structures disappear. Connected-components labelling, for instance, can be used to detect and remove blobs of a given size, where the size is defined as the number of connected pixels.

A flood-fill algorithm with an eight-neighbourhood scan was used to detect blobs greater than a defined size. This algorithm aims to find all the connected pixels from a given starting pixel. Connectivity can be defined as the similarity between the reference pixel and those in the defined neighbourhood. If connectivity is found by following the direction shown in Figure 4.15(a), the process is carried out recursively until there are no more connected pixels. Eventually, the component is removed—set to zero—if its size satisfies a defined condition. In Figure 4.15(b) for instance, only the object *A* remains when removing blobs with less than four pixels in size. The steps followed by the flood-fill algorithm are illustrated in red lines.

Removing large-sized connected components, can also remove significant pixels from vessel networks. This effect can occur when branches are fragmented in the thresholding process. In order to reduce the loss of vessel pixels, blobs less than three pixels in size were removed as they were considered noise. Figure 4.16 shows a comparison of the binary images before and after removing small connected groups of pixels with a flood-fill algorithm.

4	3	2
5	*	1
6	7	8

(a)

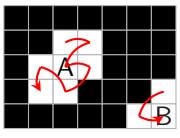

(b)

Figure 4.15: Flood-fill algorithm for analysis of connected components. (a) Scan order for a eight-neighbour pixel; (b) Detection of two connected components (seven and three pixels in size) with a flood-fill algorithm.

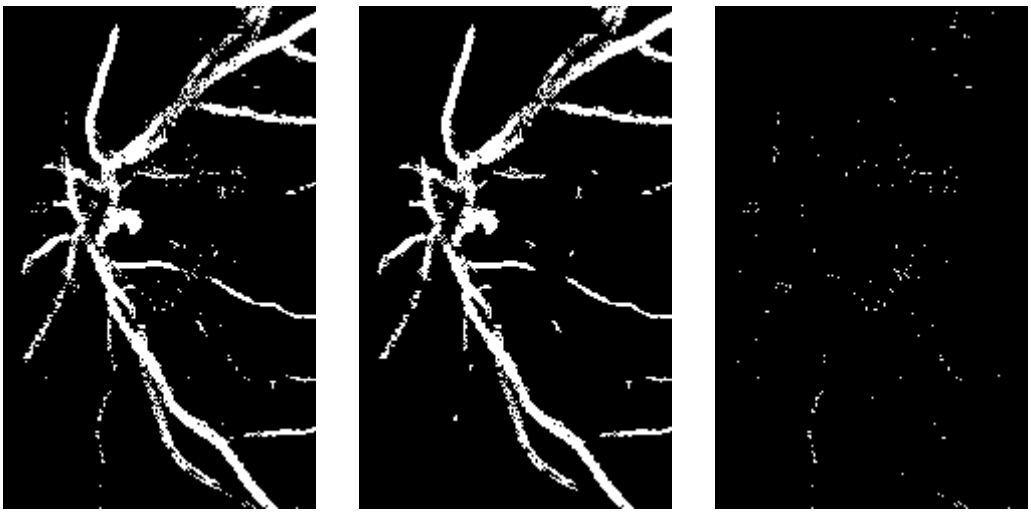

(a) **(b)** **(c)**

Figure 4.16: Removal of small connected groups of pixels from the segmented vessel networks. (a) Vessel segmentation using Otsu [87] thresholding method; (b) Processed binary image after blobs of three-pixel in size were removed with a flood-fill algorithm, and (c) small blobs removed ((a) - (b)).

4.5 Results

The proposed background extraction method is based on a low-level analysis of pixels for the local estimation of the background behind vessel networks. Consequently the estimated background can be extracted from the input image to enhance the vessel pixels. The histogram distribution from the resulting image was used to estimate the optimum threshold value to cluster the pixels into two groups: vessel- and background-pixels. With the resulting binary image, the density of vessel pixels was estimated to give the *prior probability* that a pixel lies in the vessel networks.

The proposed method was applied to retinal images from the DRIVE database [110]. For the background estimation, a Least Median Squares (LMS) method was used to locally estimate the background by fitting a set of polynomials. 1000 LMS samples were used to select the best polynomial giving the smallest median residual. Each of the samples was formed by a set of 10 blocks of pixels from a region of 9×9 blocks enclosing every pixel visited. Each block was defined as a 3×3 region of pixels. Therefore, every LMS plane-fitting sample was formed by a set of 90 pixels from a 27×27-pixels region, approximately 12% of the total pixels in the sample space.

The refinement region along the optic disc boundaries was outlined by hand, superimposing an arc segment. Adaptations to the LMS fitting method were carried out for the refinement process: the sampling space was formed by seven contiguous pixels from each side of the optic disc boundary. Since the LMS refinement used a piecewise function formed by two quadratic polynomials, each of them was treated separately with two LMS approaches: pixels falling in the optic disc region while the other LMS procedure was used outside the optic disc. The size of the LMS samples was reduced to only three single-pixels in either LMS refinement since that is the minimum number of data points required to fit a parabola. The re-estimated background on the optic disc edge was given by replacing its value with the average of the best two quadratic polynomials. Finally, small groups of connected pixels—less than three pixels in size—were removed as they were regarded noise.

Figure 4.17 shows the analysis of the vessel segmentation for some samples from the DRIVE database [110]. In the figure, the background extraction and segmented vessels are presented. The binary image containing the enhanced vessel networks was compared with the ground truth, in which the vessel networks were manually segmented by a human observer [110] (see Figure 4.18).

The estimated vessel segmentation was measured by comparing the resulting image with the ground truth. Tanimoto [28]—also known as Jaccard [20]—and Dice [23] similarity coefficients were used. For comparison purposes, in both similarity measures the ground truth image is represented by set A and the proposed segmentation method by set B. The Jaccard [20] similarity is given by the number of pixels in the intersection set divided by the number of pixels in the union set as shown in Equation 4.12.

$$J(A,B) = \frac{|A \cap B|}{|A \cup B|} \tag{4.12}$$

The Dice [23] similarity can be described as the ratio of twice the intersection set to the sum of the individual sets as shown in Equation 4.13; vertical bars represent the cardinality of a set or binary operations on these sets.

$$D(A,B) = \frac{2 * |A \cap B|}{|A| + |B|} \tag{4.13}$$

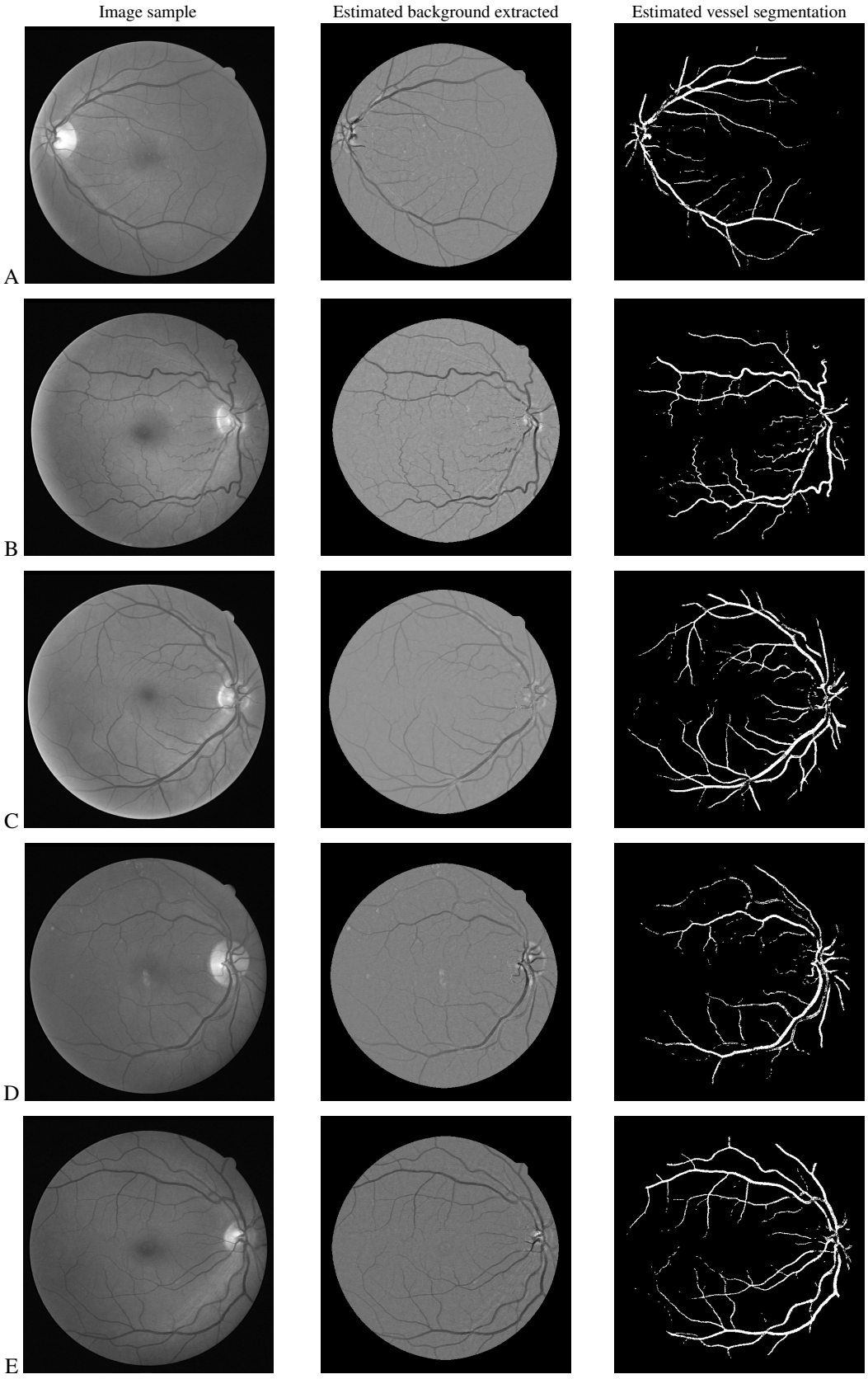

Figure 4.17: Background extraction and vessel segmentation, DRIVE retinal images database [110].

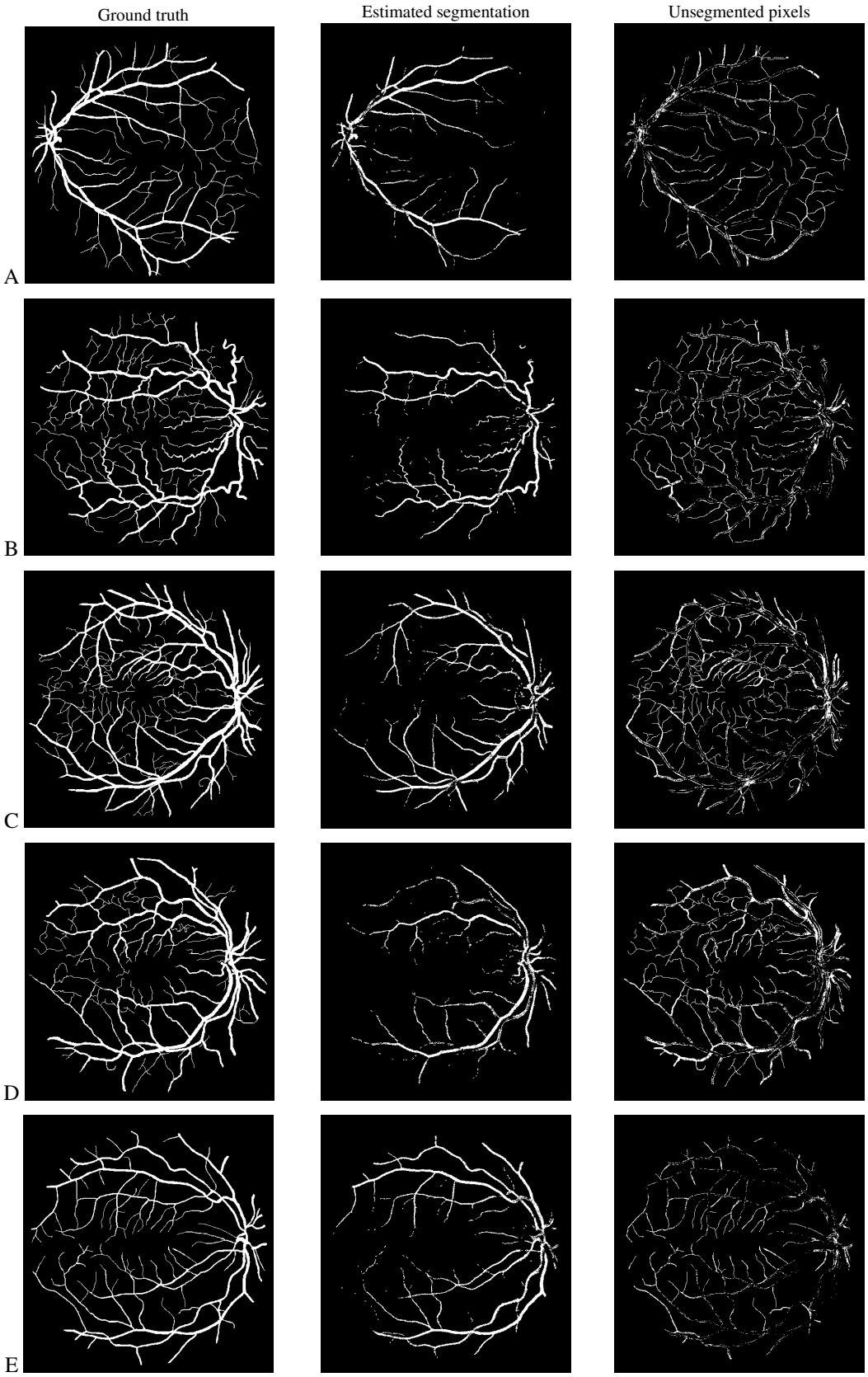

Figure 4.18: Comparison of estimated vessel segmentation and ground truth of images in Figure 4.17. From left to right: ground truth, estimated vessel segmentation and vessel pixels in the ground truth and not in the estimated segmentation.

The similarity measures used range between 0 and 1, where 0 indicates that A and B are completely different and 1 means that the match fully agrees. For instance, Jaccard yields a similarity of $1/3$ for two half-overlapping equally sized regions and Dice gives $1/2$. For a region fully encompassing another region of half its size, Jaccard yields $1/2$ and Dice $2/3$. This comparison indicates that the Dice measure weights the intersection area more heavily than Jaccard [124].

Table 4.3 shows the quantification of vessel pixels from the ground truth and the automated vessel segmentation of the samples in Figure 4.17. The density of vessel pixels was estimated from a region demarcated by an initial mask used to remove uninteresting pixels from the image. The completely dark region shown in the input images of Figure 4.17 illustrates the mask used to remove 'uninteresting' pixels from the image. The estimation of the Jaccard and Dice similarity measures is shown in Table 4.4.

Table 4.3: Quantification of vessel pixels in both ground truth and automated vessel segmentation for samples in Figure 4.18.

Image Sample	Region of interest	Ground truth (G)			Estimated vessel segmentation (E)		
		Background	Vessel	Density	Background	Vessel	Density
A	198,402	175,274	23,128	0.117	186,329	12,073	0.061
B	200,373	172,386	27,987	0.140	185,699	14,674	0.073
C	200,417	164,358	36,059	0.180	181,818	18,599	0.093
D	200,070	170,530	29,540	0.148	187,672	12,398	0.062
E	199,707	176,719	22,988	0.115	182,355	17,352	0.087

Table 4.4: Jaccard [20] and Dice [23] similarity coefficients of samples described in Table 4.3. $|G|$ and $|E|$ are the number of vessel pixels in the ground truth and the estimaged vessel segmentation.

Image sample	$\lvert G\rvert$	$\lvert E\rvert$	$\lvert G \cup E\rvert$	$\lvert G \cap E\rvert$	Jaccard	Dice
A	23,128	12,073	23,548	11,653	0.495	0.662
B	27,987	14,674	28,574	14,087	0.493	0.660
C	36,059	18,599	36,643	18,015	0.492	0.659
D	29,540	12,398	30,153	11,785	0.391	0.562
E	22,988	17,352	25,443	14,897	0.586	0.739

The Jaccard coefficient was severely affected by some factors. The intensity of vessel pixels in thin branches or bordering large ones, for instance, can disappear in the thresholding stage if their intensity is very similar to the estimated background. This occurs because the difference between the estimated background and the input

intensity can be so small that the Otsu threshold labels the pixels as background. In order to show the effect, the vessel pixels in the ground truth and not in the estimated segmentation are shown on the right column in Figure 4.18. Thin vessels and contour of big vessels are shown in the unsegmented-pixel image indicating that the ground truth encompasses the segmented vessel network.

As mentioned above, Dice [23] similarity more heavily weights the overlapping area than Jaccard [20]. Therefore, Dice coefficient is greater than Jaccard as shown in Table 4.4. Although a similarity coefficient greater than 0.7 indicates excellent overlapping agreement [7], the meaning of similarity is difficult to interpret. Nonetheless, this value can be used to compare the similarities between measured pairs [124].

4.6 Discussion

In this chapter, a local background estimation method based on LMS was proposed to extract the background and enhance the vessel networks in retinal images. This method aims to fit data to a plane approximating to the ideal background intensity and where this is not possible, a piecewise function is used. An improvement method to re-estimate the background near the optic disc boundaries was proposed since large contrast difference between pixels bordering the optic disc edge did not allow plane-fitting, as expected.

For the background re-estimation method, a piecewise function—formed by two quadratic polynomials—was used considering sets of pixels inside and out the optic-disc region independently. Vessel branches falling in the 1D-sampling-space can disappear in the thresholding process since the fitted polynomial can return small MMSE values. This led to a small difference in intensity between the input image and estimated background for which the thresholding method regarded those pixels as background. In addition, intensity attenuation of pixels from fine vessels and bordering big vessel branches allowed only a little enhancement after the background estimation. The thresholding method used clusters pixels into two groups: *true* vessels and its complement. Fine vessels and pixels bordering big vessels can be mislabelled by the thresholding method if the MMSE is small, showing a similar behaviour to the MMSE computed in background regions.

The images used in this chapter can be found in the DRIVE [110] database. They are stored in an 8-bit colour TIFF (Tagged Image File Format) format and were projected to grey level for analysis. The DRIVE ground truth appears to have been produced using a high resolution monitor with a bigger pixel intensity range. There are many fine vessels in the DRIVE ground truth for which we can see absolutely no evidence in the TIFF images, which alone produces a significant source of error. For an ideal vessel model represented by a cylindrical object, the contrast decreases towards the edge of the vessel. In addition, it is assumed that noise remains constant in the image. Giving the last two premises, the signal-to-noise ratio gets worse at the edges of vessels leading us to expect more detection of errors in the border-region of vessel structures. The same arguments hold for fine vessels which are expected to fragment more.

4.7 Conclusions

The proposed background extraction method yields a quantification of vessel pixels in a given image. This can be simplified as the *prior probability* that a pixel belongs to the vessel networks in a particular image. The proposed background extraction is based on a simple analysis of the neighbouring pixels to locally estimate the background behind vessel networks. Vessel pixels with little difference between their input intensities and the estimated background are usually misclassified as background by the thresholding method based on Otsu [87]. Pixels in fine vessels and bordering vessel branches usually present this condition. Since the thresholding method clusters pixels into two groups, the loss of bordering pixels can be interpreted as if its intensity was closer to the background than the intensity along the centreline of a large vessel, the latter, described as the best vesselness definition.

In order to cope with the loss of fine vessels and bordering pixels, a probabilistic labelling method is presented in Chapter 5. The aim of the labelling method is to estimate the *posterior probability* that a pixel belongs to a vessel. The estimation of that probability requires the prior probability is estimated using the proposed background extraction presented in this chapter. The probabilistic labelling method can be used with contextual approaches to make further analysis on a defined neighbourhood to

enhance pixels with weak probability but surrounded by strong evidence allowing a better vessel network segmentation.

Chapter 5
Probabilistic labelling of vessels

5.1 Introduction

In medical image analysis, desired objects can be described by their texture, shape and size among other features. For instance, blood vessels can appear at a range of diameters, size and contrast in retinal images and Magnetic Resonance Angiograms (MRAs). Blood vessels can be described as tubular structures. An ideal vessel model can be defined as a straight cylindrical object following a straight direction with constant diameter. In retinal imaging, a uniformly-filled tubular structure can be represented with a large contrast along the centreline with the contrast decreasing towards the structure walls. A synthetic image of a single straight vessel is shown in Figure 2.7 (p. 13).

The attenuation ratio is based on the 'ideal vessel' model used. Frangi [35], Sato [106] and Lorenz [73], for instance, defined this attenuation as a Gaussian-like function. These approaches use the Hessian matrix as local descriptor since it describes the maximum and minimum directional derivatives locally [44]. Sukanya[112], for instance, described some surface shapes by analysing eigenvalues and the local orientation. In [26, 35, 54, 72, 106, 121] authors estimate a 'vesselness' measure based on

the local curvature and direction using eigenvalues and eigenvectors. Some of these 'vesselness' measures were explained in Section 2.7 (p. 25).

The novel vessel-pixel labelling method presented in this chapter is based on a Bayesian approach. Unlike deterministic approaches [35, 73, 106], the proposed labelling method aims to estimate the probability that vessel-pixels are located along a vessel's structure by quantifying local and global features. Since blood vessels can be described as tubular structures, the Hessian matrix can be used as local a descriptor to estimate the probability that a local curvature fits an ideal vessel curvature.

As mentioned above, the ideal curvature is given by modelling local features along the centreline of a single, straight vessel. As a global feature, quantification of pixels along the vessel network is required to estimate the probability of selecting a vessel pixel. This feature is not a directly observable variable from computing the Hessian matrix. Thus, an estimation of vessel pixels in a whole image was carried out using the method described in Chapter 4. With the local and global features, Bayes' rule can then be used to estimate the local probability that a pixel belongs the centreline of a vessel. Bayes' rule is explained in Section 5.2; computation of its components leading to the posterior probability are fully described in the subsequent sections.

5.2 Bayes' rule

Bayesian analysis can be defined as an approach that allows making inferences from data using probability models based on observed data and prior knowledge. Bayes' rule was first suggested by Thomas Bayes $(c.1701 - 1761)$ and published in 1763 after his death [111]. Bayes's rule is a simple equation used to estimate conditional probabilities. This rule expresses the conditional probability—termed *posterior probability*—of an event A after B is observed in terms of prior knowledge of A, prior knowledge of B, and the conditional probability of B given A.

Since Bayes' rule is expressed in terms of probability relations, some axioms of probability theory are reviewed to derive Bayes' rule. In this work, the commonly used notation for the probability of an event A denoted by $P(A)$ is used. Let A and B

be two events, the probability that both A and B occur can be written as the probability that both B and A occur; this is a commutable estimation (see Equation 5.1).

$$P(A \textit{ and } B) = P(B \textit{ and } A) \tag{5.1}$$

The probability of a conjunction is defined as the probability of A being multiplied the probability of B given A (see Equation 5.2).

$$P(A \textit{ and } B) = P(A)P(B|A) \tag{5.2}$$

Since the operation in Equation 5.1 is commutable and by definition 5.2, it also yields:

$$P(B \textit{ and } A) = P(B)P(A|B) \tag{5.3}$$

In addition, since left half of the last two equations are equal to $P(A \textit{ and } B)$, it produces:

$$P(B)P(A|B) = P(A)P(B|A) \tag{5.4}$$

This means that there are two ways to estimate the probability of a conjunction. If $P(A)$ is known, then it is multiplied by the probability $P(B|A)$. Conversely, if $P(B)$ is known, it is multiplied by $P(A|B)$ [25]. Finally, if both halves in Equation 5.4 are divided by $P(B)$, it produces:

$$P(A|B) = \frac{P(A)P(B|A)}{P(B)} \tag{5.5}$$

Equation 5.5 is known as *Bayes' rule* that expresses the probability of A given B. This is equal to the probability of A, multiplied by the probability of B given A, divided by the probability of B. $P(A)$ is the probability of the hypothesis A and is termed the *prior probability* or just the *prior* since it can be estimated before knowing data B. The probability of the observed data B under the hypothesis A is denoted by $P(B|A)$ and termed the *likelihood*. The denominator $P(B)$ is the probability of the data B under any hypothesis, this is often termed the *normalising constant*, *marginal likelihood* or *evidence* [25, 111]. Finally, $P(A|B)$ is termed the *posterior probability* or just the *posterior* given by the probability of the hypothesis A after data B are observed.

Additional to the Bayes' rule derivation described above, an alternative notation can be formulated using some other assumptions:

$$P(B) = P(A \text{ and } B) + P(A^c \text{ and } B) \tag{5.6}$$

where A^c is the complementary event of A, often termed 'not A' and denoted by $\neg A$.

Following the conjunction definition 5.2, the probability $P(B)$ can be written as in Equation 5.7.

$$P(B) = P(A)P(B|A) + P(\neg A)P(B|\neg A) \tag{5.7}$$

An alternative Bayes' rule definition is shown in Equation 5.8 by replacing the denominator in Equation 5.5 by its equivalence in Equation 5.7.

$$P(A|B) = \frac{P(A)P(B|A)}{P(A)P(B|A) + P(\neg A)P(B|\neg A)} \tag{5.8}$$

A typical Bayesian analysis can be outlined by dividing it in the following a set of steps, like those suggested in [38]:

1. Set up a probability model for all observable and unobservable quantities in the problem. In this stage, the local and global features are used for the vessel-pixel labelling in Bayes' rule.
2. Estimate the *prior* distribution before the data are observed based on background information.
3. Estimate the *evidence* and *likelihood* based on the observable data.
4. Compute the posterior probability by combining steps 2 and 3.
5. Evaluate the fit of the model and implications of the resulting posterior probability.

As discussed in Section 5.1, eigenvalues from the Hessian matrix were used as a local descriptor for every analysed pixel to estimate the maximum probability of being along the vessel central section. This can be regarded as the event B in Bayes' rule. The labelling problem can be described as a two-class labelling problem: vessel (V) and background (B) pixels. Thus, the alternative Bayes' rule Equation 5.8 was used to

estimate the *posterior probability* and it can be written as:

$$P(V|\underline{\lambda}) = \frac{P(V)P(\underline{\lambda}|V)}{P(V)P(\underline{\lambda}|V) + P(B)P(\underline{\lambda}|B)} \tag{5.9}$$

where V is the desired *vessel* label, $\underline{\lambda}$ the local eigenvalues defined in Equation 5.10 and B—the complementary event of a vessel—denotes *background*. Note that B in Equation 5.8 has been replaced by $\underline{\lambda}$ and $\neg A$ by the literal B to refer to the local descriptor and Background pixels respectively.

$$\underline{\lambda} = (\lambda_1 \ \lambda_2)^T \tag{5.10}$$

Following the Bayesian analysis plan described above, the first task is the definition of a probability model that is given by Equation 5.9 where two labelling-classes were defined. Steps two and three focused on the estimation of the Bayes' rule components. Since the *evidence* has been extended, the denominator in Bayes' rule requires the likelihood estimation of both vessel and background classes. Estimation of the Bayes' rule components is described in the next sections and the *posterior* probability is detailed in Section 5.7

5.3 Prior-vessel probability

The probability of vessel pixels denoted by $P(V)$ can be estimated before obtaining the local features of each pixel for labelling. Since this is not a directly observable variable, an approximate vessel segmentation was carried out to estimate this prior from the image.

As a first approach, a vessel network segmentation was estimated using the background extraction method described in Chapter 4. The outcome is a binary image containing an approximation of the vessel network segmentation as shown in Figure 5.1. The estimated background is shown in Figure 5.1(b) that is subtracted from input image 5.1(a) and with some post-processing work the vessel network is segmented from the background (see Figure 5.1(c)).

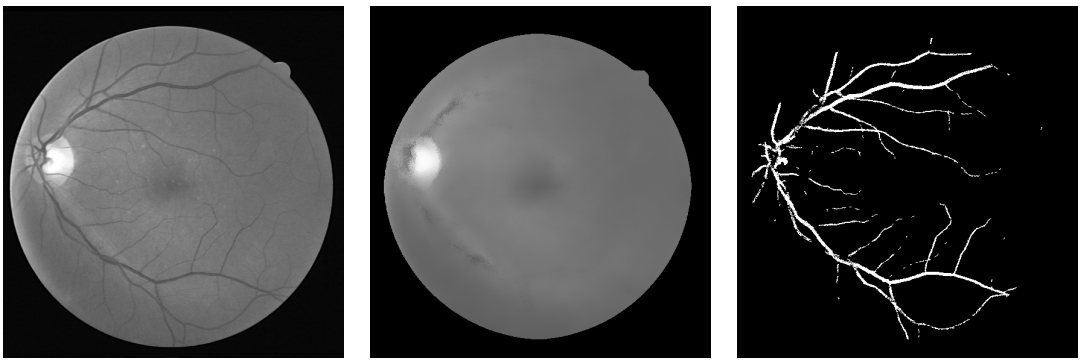

(a) **(b)** **(c)**

Figure 5.1: Vessel network segmentation using the background extraction approach described in Chapter 4. (a) Input image. (b) Estimated background. (c) Segmented vessel network by subtracting the estimated background and post-processing to compute a binary image.

Quantification of pixels in the segmented network produces an estimated distribution of vessel pixels that can be used as a probability measure. The prior probability $P(V)$ is then given by dividing the number of segmented vessel pixels (the binary image) by the number of pixels in the processed region from the image:

$$P(V) = \frac{A(Estimated\ vessel\ network)}{A(Region\ of\ interest)} \tag{5.11}$$

Note that the number of pixels in the analysed region is given by a initially defined mask for every processed image (see Figure 5.2).

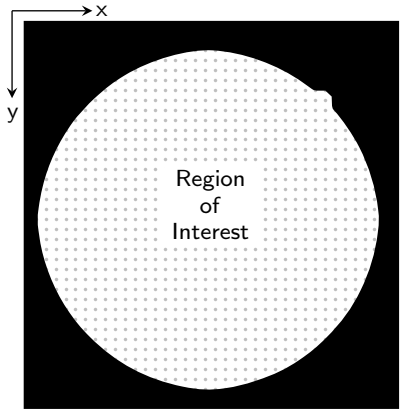

Figure 5.2: Processed Region of Interest (RoI) in an image.

Some image samples from the DRIVE [110] database are shown in Figure 5.3 (p. 81). The vessel network segmentation was based on the approach fully described in Chapter 4. Data analysis of the processed images is summarised in Table 5.1.

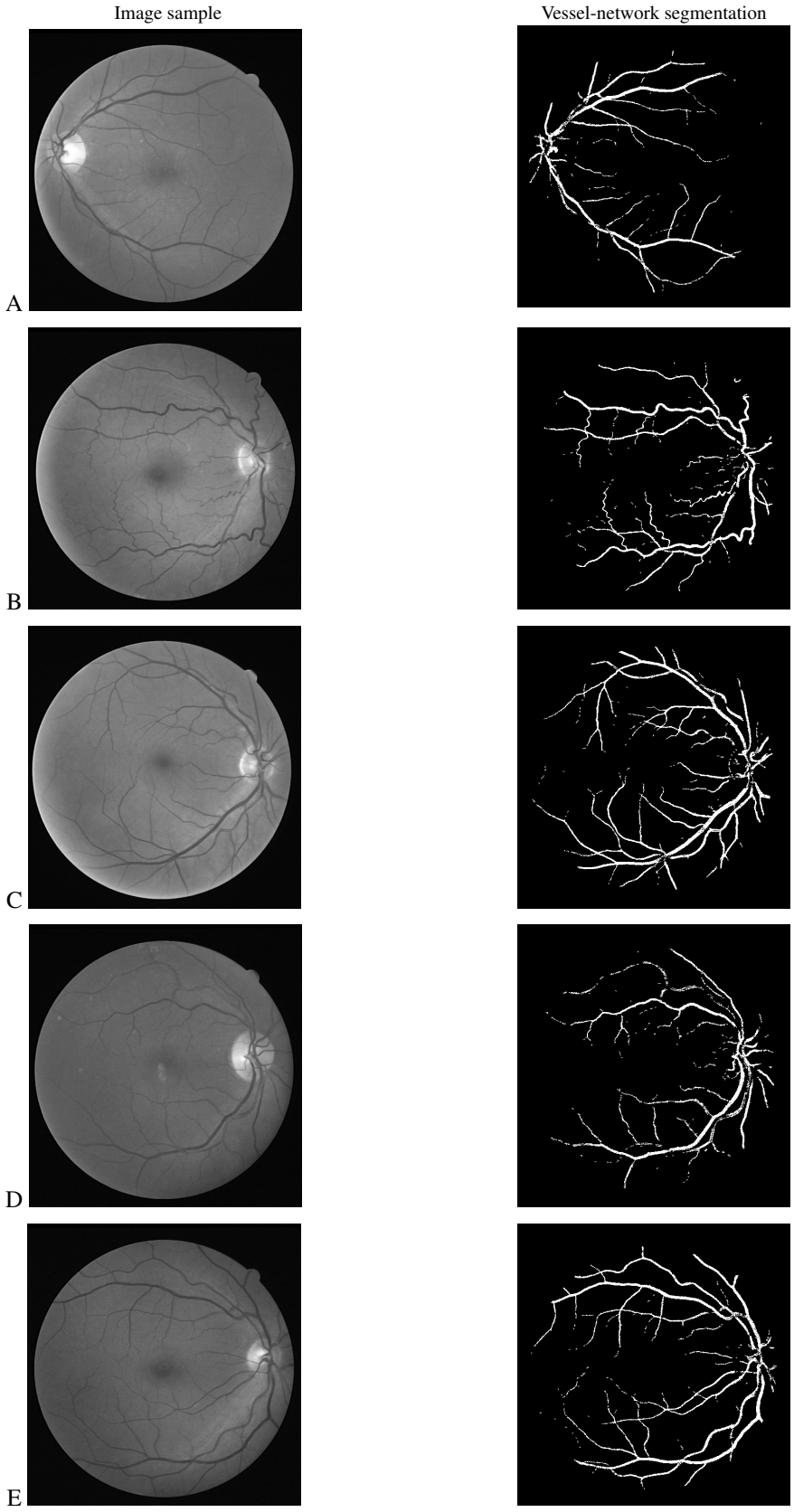

Figure 5.3: Estimated vessel network segmentation, DRIVE [110] database samples.

Table 5.1: Prior vessel pixel probability $P(V)$ estimation for images in Figure 5.3. Table shows the quantification of pixels in the processed region (Region of Interest) and the estimated vessel-network for the *prior* vessel probability estimation.

Image Sample	Region of interest	Estimated Vessel-Network Area	Estimated $P(V)$
A	198,402	12,073	0.061
B	200,373	14,674	0.073
C	200,417	18,599	0.093
D	200,070	12,398	0.062
E	199,707	17,352	0.087

5.4 Prior-background probability

As described in Section 5.2, the event A in the initial Bayes' rule (see Equation 5.8 on page 78) has two possible values: vessel or background pixel. These two classes are mutually exclusive. Therefore, the sum of their probability is 1. In Section 5.3, the prior probability of vessel pixels was estimated. Thus, the estimated background probability $P(B)$ for each treated image is given by solving Equation 5.12 for $P(B)$.

$$P(V)+P(B)=1 \tag{5.12}$$

A summary of the estimated probabilities $P(V)$ and $P(B)$ for the sample images used in Figure 5.3, is shown in Table 5.2.

Table 5.2: Estimated *prior* probabilities for some DRIVE [110] sample images. Table showing the *prior* vessel and background probability.

Image Sample	Estimated $P(V)$	Estimated $P(B)$
A	0.061	0.939
B	0.073	0.927
C	0.093	0.907
D	0.062	0.938
E	0.087	0.913

5.5 Vessel-likelihood

In general, a likelihood or conditional probability can be denoted as $P(b|A)$. Here, the definition aims to estimate the probability that observed data B has the value b

given the assumed parameter value A. This conditional probability is called likelihood of A since for a given parameter A, it estimates how likely are the data [111]. The relevance of the likelihood is that it analyses the distribution of the possibly observable values for an occurring event. When considering all possible values of A and B—in the conditional probability—the likelihood can be defined as a function [111]. In this manner, the likelihood allows us to describe how the probability of the event B changes when the event A has occurred. Likelihood is a Probability Density Function (PDF) since the estimated probability is a function of the observable variable $\underline{\lambda}$ given the fixed conditions on $\{V$ (vessel), B (background)$\}$.

The two likelihood estimations defined in Bayes' rule (see Equation 5.9 on page 79) were computed to describe the eigenvalue distribution for each class (*vessel*, *background*) over possible conditions in which vessels can appear. Their estimations are based on similar processes but vary in the observed data used. In Bayes' rule numerator, the vessel likelihood $P(\underline{\lambda}|V)$ is first defined; its estimation is described below. Estimation of the other likelihood—background $P(\underline{\lambda}|B)$—is detailed in Section 5.6 to complete the estimation of all components forming Bayes' rule.

The vessel likelihood $P(\underline{\lambda}|V)$ was estimated using a Monte Carlo simulation to describe the eigenvalue distribution for vessel pixels in synthetic images. Afterwards, the computed bank of eigenvalues were analysed to construct a probability density function. Since analysed images are in 2D, $\underline{\lambda}$ holds two eigenvalues. Thus, the PDF was defined as a normalised two-dimension histogram describing the probability of every pair $\underline{\lambda}$ given the vessel class. Settings used in the Monte Carlo simulation are detailed in the next section and the PDF computation in Section 5.5.2.

5.5.1 Monte Carlo simulation

A Monte Carlo trial yielded a pair of eigenvalues $\underline{\lambda}$ from some location in a synthetic image that represents a class of pixels—vessel or background. In this approach, eigenvalues from pixels falling in a synthetic vessel object were used for the vessel-likelihood estimation. A synthetic straight and uniformly filled cylinder was the model used to represent the ideal vessel, where the intensity profile across the vessel object was determined by the Beer-Lambert Law [19]. The synthetic image formation process

is detailed in Section 3.3.2 (p. 39). In order to take into account features from retinal images, the background intensity and noise power were computed from the estimated background.

In the vessel formation process, a maximum intensity projection is defined to create a uniform background from which, the intensity is attenuated generating a synthetic vessel. The maximum projection is given by the mean contrast computed from the estimated background. Thus, a Monte Carlo simulation can be performed after estimating the background, mean background contrast and noise power for a particular image. The background estimation process is detailed in Chapter 4. The mean contrast from the estimated background of some DRIVE [110] image samples is summarised in Table 5.3.

Table 5.3: Estimated mean grey-level and standard deviation of the estimated background.

Image Sample	RoI Area	Mean Grey-level	Standard Deviation	Image Sample	RoI Area	Mean Grey-level	Standard Deviation
21	198,402	119.622	16.931	31	200,408	110.174	27.832
22	200,373	102.426	13.623	32	197,792	118.423	13.228
23	200,843	119.627	20.208	33	200,436	120.865	15.914
24	200,417	119.924	11.339	34	199,293	100.232	42.498
25	200,070	89.746	12.218	35	200,357	90.479	18.058
26	197,945	63.807	9.099	36	199,924	95.287	16.156
27	200,504	113.405	18.430	37	199,897	97.574	18.794
28	200,037	116.843	13.950	38	199,000	128.063	14.417
29	200,028	71.800	13.748	39	200,173	92.353	9.433
30	199,965	58.338	9.519	40	199,707	75.961	10.473

As mentioned above, a Monte Carlo trial is formed by the eigenvalues $\underline{\lambda}$ belonging to a sample pixel from a vessel object. Samples were randomly selected from a space of size equal to the vessel diameter. Due to symmetry and simplicity, the sampling space was defined as a set of pixels normal to the vessel orientation. Figure 5.4 illustrates the sampling-space from which vessel-sample pixels were randomly selected and termed a Monte Carlo trial.

10,000 trials were computed using randomly-varying parameters when constructing synthetic vessels to integrate features that can be found in retinal images. Vessel diameter, for example, ranged over [1...15] pixel-units in a continuous domain to incorporate vessel diameters that can appear in low-resolution retinal images as shown in [75]. Vessel orientation was simulated by randomly rotating the image. Since

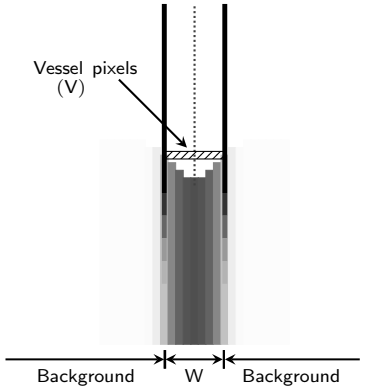

Figure 5.4: Vessel-pixel sampling space. The sampling space is delineated by W, where W is equal to synthetic vessel width.

a synthetic vessel was straight and, due to symmetry in the rotation process, the range of rotation was defined as $[0^\circ \ldots 45^\circ]$. Despite eigenvalues being invariant to rotation, this operation was carried out to approximate the pixellation effects when capturing an image. Finally, Gaussian-distributed noise was added to mimic the noise produced by the imaging device when capturing an image. The noise power was obtained from a prior analysis from retinal images as follows.

The proposed method aims to estimate the eventual thermal noise, which can be regarded as Gaussian noise, produced by the imaging device. A free-of-vessel patch can be used to estimate the noise power as suggested in [105]. Nonetheless, it is difficult to define a fixed size and location for the patch to be analysed due to the vessel distribution varying in images. Thus, the noise power was computed from the estimated background, and it is assumed to be approximated to the signal captured by the camera if there were no objects. Unlike selecting a single patch, the proposed method regarded all regions in the image; except that the estimated background will be low-pass filtered by the noise-power estimation process leading to—at some extent—an underestimation of the noise.

Standard deviation of noise was estimated with an algorithm due to Rank [96]. The algorithm is based on an iterative histogram analysis using a filtered version of the image, where difference operators were applied in vertical and horizontal directions [96]. The aim of the operators is to reduce the influence of the content. The estimated standard deviation of noise for the tested images is summarised in Table 5.4.

As described above, the mean background intensity and noise power estimation in conjunction with a set of random variables were used to setting up the Monte Carlo

Table 5.4: Estimated standard deviation σ of noise for images in the DRIVE [110] database.

Image Sample	Estimated σ noise	Image Sample	Estimated σ noise
21	2.609	31	2.713
22	2.551	32	2.472
23	3.344	33	2.655
24	2.842	34	4.717
25	2.353	35	3.055
26	2.512	36	2.946
27	2.719	37	3.729
28	2.800	38	2.597
29	2.666	39	2.540
30	2.350	40	2.535

simulations to estimate the vessel likelihood. For every image being treated, the Monte Carlo simulation parameters are estimated. Figure 5.5 shows synthetic-vessel-images generated by using the estimated mean background intensity and noise power.

Dispersion of the Monte Carlo trials is shown in Figure 5.6, where the x and y axes are given by the eigenvalues $\underline{\lambda}$. Eigenvalues are in ascending order based on its magnitude as suggested in [35].

5.5.2 Probability Density Function

A Probability Density Function (PDF) can be approximated with a normalised histogram. A histogram is a graphical representation of a set of counts x given by grouping a set of data N [111]. The sum of counts x equals the number of elements in a data set N, as it is only a distribution representation of N. Normalisation of the histogram yields the PDF; the area under the PDF equals to one. Figure 5.7 illustrates a histogram and PDF for a data set N, formed by 10,000 random values over a uniform distribution, divided into 20 bins.

The example in Figure 5.7 works for a single variable. A Monte Carlo trial is formed by two variables: eigenvalues (λ_1, λ_2), thus, the PDF can be approximated by combining two single PDFs in which bounds are given by the eigenvalue measures and

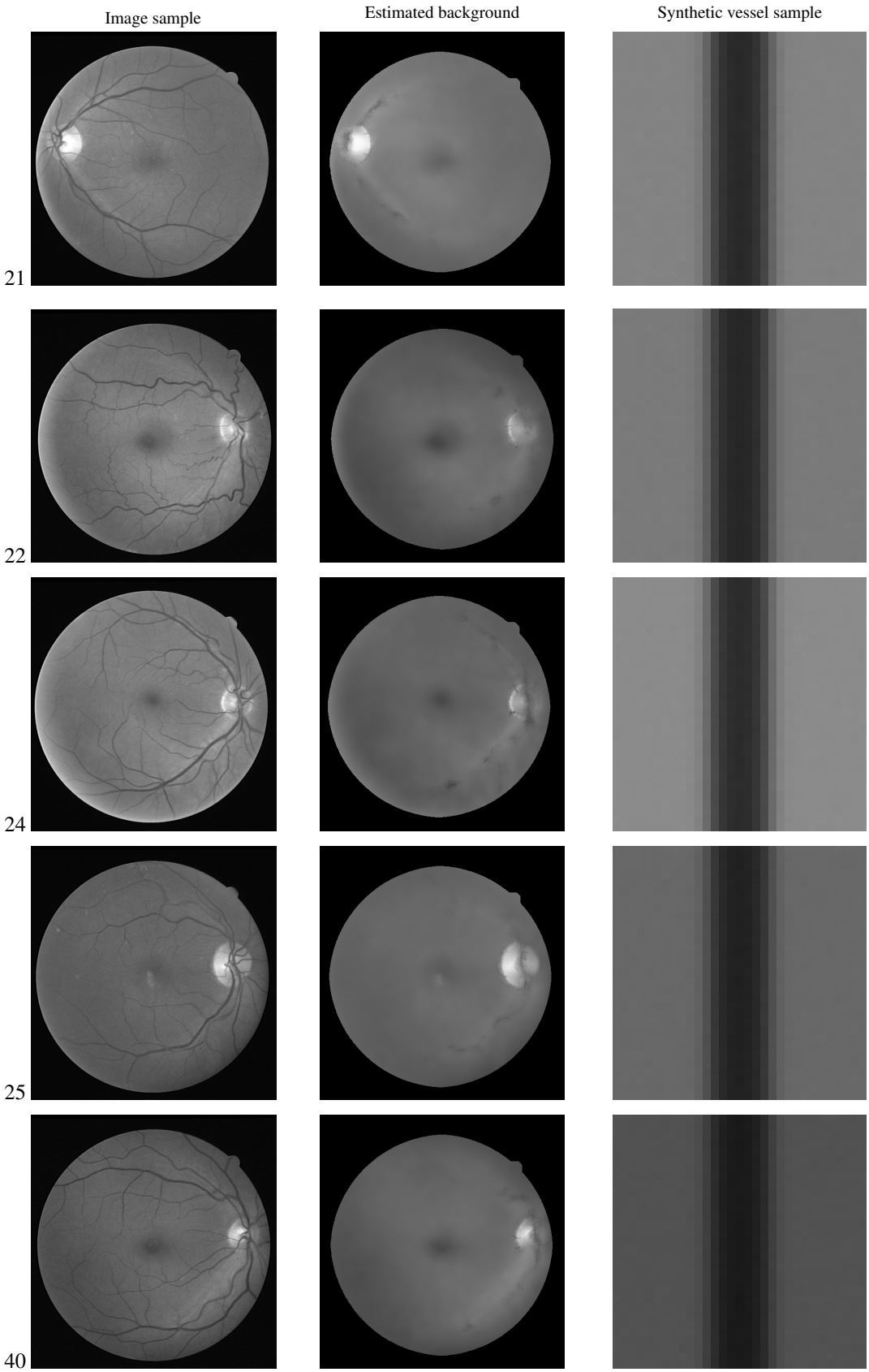

Figure 5.5: Synthetic vessel images. Uniform background defined by the mean background intensity (see Table 5.3); Gaussian-distributed noise was added using the standard deviation of noise presented in Table 5.4

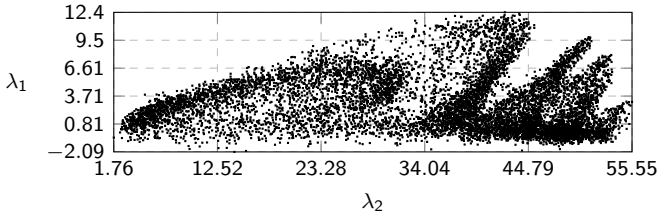

Figure 5.6: 10,000 *vessel* Monte Carlo trial dispersion. Eigenvalues are in ascending order $|\lambda_1| \leq |\lambda_2|$ as suggested in [35].

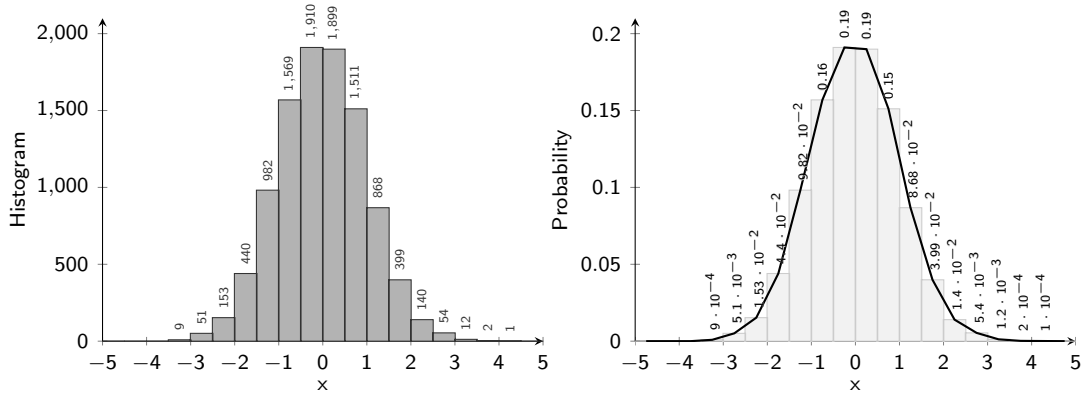

(a) **(b)**

Figure 5.7: Histogram and probability density representation. (a) Histogram of $N = 10,000$ random values with uniform distribution. The histogram was formed by grouping the values into x number of bins (20). Label at the top of a bin represents the counts in the bin. (b) Normalised histogram. This approximates the probability density function (PDF) [111]. Label at the top of greyed bins describes the normalised counts in the bin.

.

the number of bins can be independently defined. The proposed PDF was formed as follows.

For each eigenvalue, the minimum and maximum of the variate are used to divide the range into a number of intervals termed bins. The range of measured λ_1 values was divided into a set of y number of equally-sized bins and the range in λ_2 into x number of equally-sized bins; note that x and y are treated individually. Finally, the Monte Carlo trials falling within every pair of (x, y) bins were counted.

Normalisation of the counts yields a 2D-PDF. It can be seen as a normalised two-dimension histogram formed by vertical columns, where the height of each column mirrors the probability for a $\underline{\lambda}$ falling in a particular pair (λ_1, λ_2) bin. When the range of measured eigenvalues is grouped into a small number of bins, the histogram does not describe the distribution of data very well. Similarly, when the range of measurements is grouped into a large number of bins, the histogram may not give a good

sense of the data distribution. There is thus a trade-off between the number of bins which data are grouped in and the sense of the distribution of observations.

The Monte Carlo simulation described in Section 5.5.1 was analysed due to the computed PDF. The number of bins in which a variable was divided is independent from the other bin distributions. For instance, range values in λ_2 and λ_1 were divided into 50 equally-sized bins producing the two-dimension histogram shown in Figure5.8.

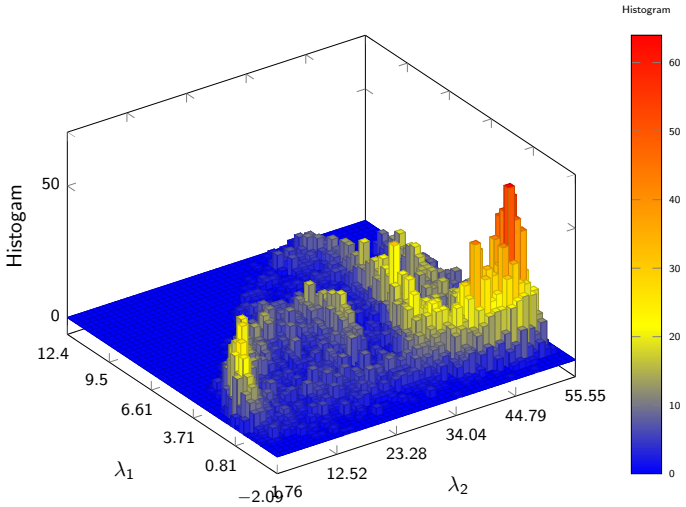

Figure 5.8: Monte Carlo-trials histogram for the vessel-likelihood estimation. Range of λ_1 and λ_2 measures are grouped into 50 equally-sized bins. Height of bars is equal to the number of trials falling within a (λ_2, λ_1) bin.

The counts in every cell of the histogram were divided by the number of accumulated trials in the histogram—10,000 Monte Carlo trials—to generate a normalised histogram which was taken as the PDF. The resulting PDF can be described as a map of probabilities where axes are given by the bins in which eigenvalues were grouped.

Figure 5.9 shows the PDF from the data plotted in Figure 5.8. The probability map can be used as the likelihood $P(\underline{\lambda}|V_C)$ in Bayes' rule.

Smoothing the probability density function

A smoothing process, based on a bi-triangular smoothing kernel, was applied to compute the vessel probability density function. The aim of this process is to generate a smoother probability density function, which may better mirror the distribution of the eigenvalue variates. The triangular distribution is a simple method that allows smoothing data sets.

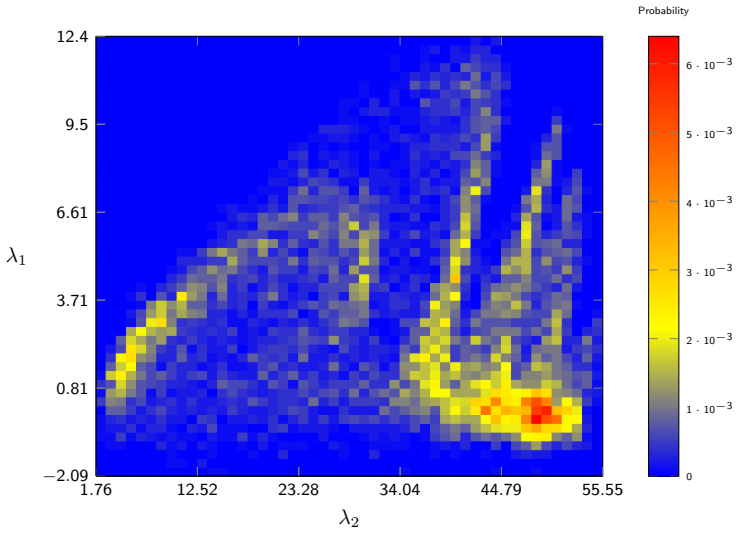

Figure 5.9: Vessel Probability Density Function (Normalised histogram in Figure 5.8). The sum of the entries (probabilities) is equal to One.

A triangular function principle was extended producing a pyramid-shape element to cope with the smoothing of the λ_1 and λ_2 variates. The length and width of the element is given by the bin size in the histogram, which is regarded as uniform along the axes. The volume under the pyramid is taken as one. The element is centrally placed on the (λ_1, λ_2) sample position and the partial volume of the pyramid covering the bin area is taken as the gain for that bin. In the ideal case, a sample falling at the central point of a bin produces a unit-gain for the bin since the pyramid matches the bin bounds. Nonetheless, when a sample is not centrally located within a bin, the pyramid element usually overlaps adjacent bins producing a sharing of the unit-gain. See Appendix A for details of the smoothing process.

The resulting smoothed probability probability function in Figure 5.9 is shown in Figure 5.10.

5.6 Background-likelihood

The background likelihood denoted by $P(\underline{\lambda}|P(B))$ in Bayes' rule denominator describes the eigenvalue distribution for the background-pixel class. In the synthetic images used, the intensity of the background is initially set as uniform based on the estimated background contrast and then, Gaussian-distributed noise is added to

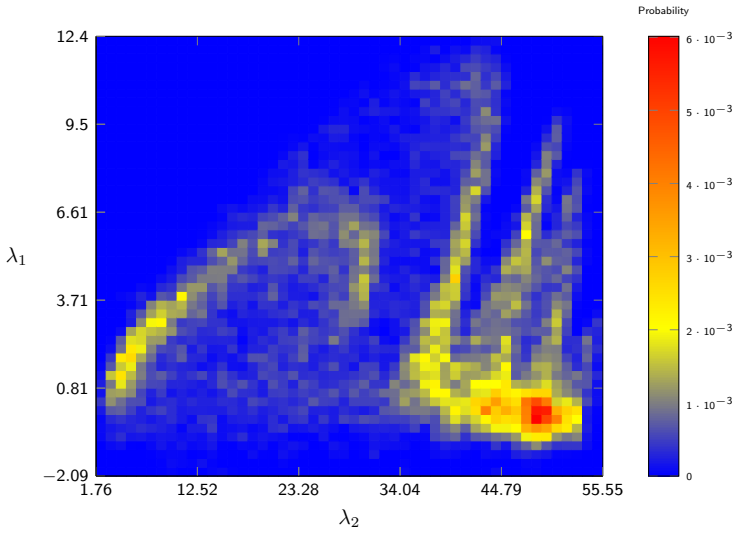

Figure 5.10: Smoothed vessel probability density function

mimic the thermal noised introduced by the imaging device when capturing an image. Background-pixel samples were generated to draw the eigenvalue dispersion that eventually yields the PDF. Similarly to the vessel likelihood estimation (Section 5.5), a Monte Carlo simulation was used to generate a set of background samples to estimate the likelihood $P(\underline{\lambda}|B)$. Randomly selected parameters were used to produce synthetic images with features similar to those found in retinal images. The Monte Carlo simulation settings are described in the next section and the PDF estimation in Section 5.6.2.

5.6.1 Monte Carlo simulation

A Monte Carlo simulation was implemented to analyse the dispersion of the estimated $\underline{\lambda}$ from a set of background-pixel samples. Synthetic vessel images were constructed using the method described in Section 3.3.2 (p. 39). The ideal background can be described as uniform contrast given the maximum projection defined for the treated image. The maximum projection is considered as the situation which light beams cross eye tissue with uniform light-absorption properties. For an image being treated, the maximum projection is taken as the mean contrast computed from the estimated background process. Gaussian-distributed noise of power σ is added to the background patch and finally, the resulting patch is randomly rotated as described in Section 3.3.2.

The process described above is valid for the estimation of an ideal background patch, with no vasculature structures. Pixels bordering vessel structures, however, are regarded as background but their intensity is affected by the transition from the vessel- to the background-like intensity value. This may not result in fair background-pixel samples being selected from a noisy background patch. In order to make the background class definition fairer, pixels from synthetic images containing a vessel structure were used. Background-pixel samples were selected from a delineated sampling space covering pixels bordering the synthetic vessel. Therefore, a Monte Carlo trial is formed by the eigenvalues $\underline{\lambda}$ belonging to a randomly selected pixel from a sampling space.

Rather than defining the sampling space as any pixel in the image except those falling within the vessel structure of width w, the sampling space was defined as a set of contiguous pixels normal to the vessel orientation and its length is given by

$$D = \frac{\overline{W} * (1 - P(V))}{P(V)} + \overline{W} \tag{5.13}$$

where $\overline{W}$ is the mean vessel width, and $P(V)$ is the *prior* vessel probability. The equation is valid for any $-w/2 \leq x \leq w/2$ where w is the known width of the synthetic vessel.

The rationale for using Equation 5.13 is to estimate the space based on features of the image. In the equation, the *prior* vessel probability excludes the vessel pixels as the estimated vessel-pixel area is regarded being formed by vessel structures of a mean width equal to $\overline{W}$, eight pixel-units in the tests. Figure 5.11 illustrates the sampling space from where background-pixel samples—Monte Carlo trials—are randomly selected.

The Monte Carlo simulation was based on the process implemented for the vessel-pixels described in Section 5.5.1. Random variates were used to generate 10,000 synthetic vessel images. Background samples were then selected from a delineated sampling space.

Dispersion of the Monte Carlo trials is shown in Figure 5.12 where the x and y axes are given by the eigenvalues $\underline{\lambda}$ measures. Eigenvalues are in ascending order due to its magnitude as suggested in [34].

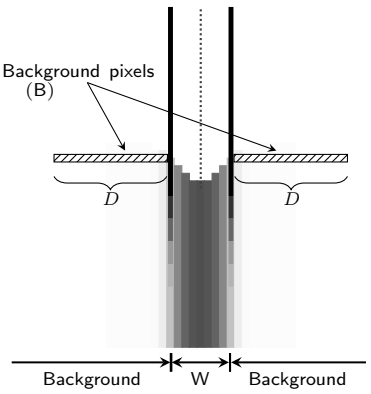

Figure 5.11: Background-pixel sampling space. The parameter D is used to estimate the size of the sampling space. Global features are used to exclude pixels falling within the vessel object.

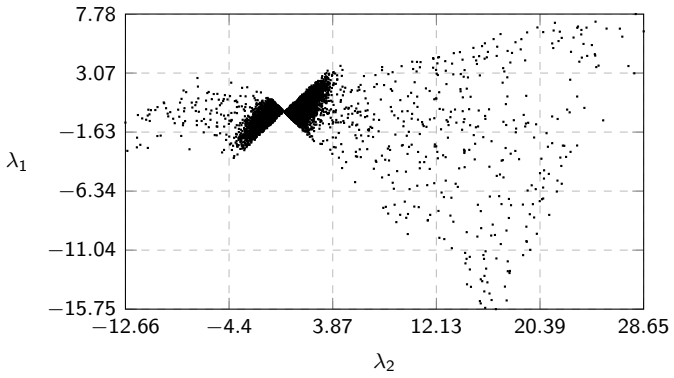

Figure 5.12: 10,000 *background* Monte Carlo trial dispersion. Eigenvalues are in ascending order $|\lambda_1| \leq |\lambda_2|$ as suggested in [35].

5.6.2 Probability Density Function

Monte Carlo trials from Section 5.6.1 were binned producing a 2D histogram. As described in Section 5.5.2, the range of eigenvalue measures were divided into a set of equally-sized segments termed bins. Eventually, every Monte Carlo trial $\underline{\lambda}$ was binned yielding a histogram. Figure 5.13 shows the histogram generated from binning the 10,000 Monte Carlo trials in the test using 50 equally-sized bins for both of the eigenvalue measures.

Normalisation of the histogram yields the PDF. Therefore, the counts in every cell of the histogram were divided by the number of the accumulated values in the histogram—10,000 trials in the test—producing the probability density function shown in Figure 5.14.

The accumulating method, however, was modified to produce a smoother histogram. Rather than increasing in 1 the value of the cell where a sample falls, the

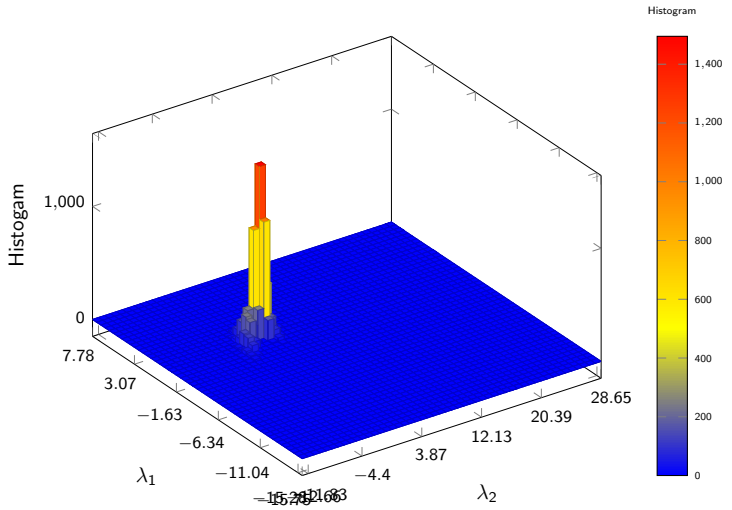

Figure 5.13: Monte Carlo-trials histogram for the background-likelihood estimation. Range of λ_1 and λ_2 measures are grouped into 50 equally-sized bins. Height of bars is equal to the number of trials falling within a (λ_2, λ_1) bin.

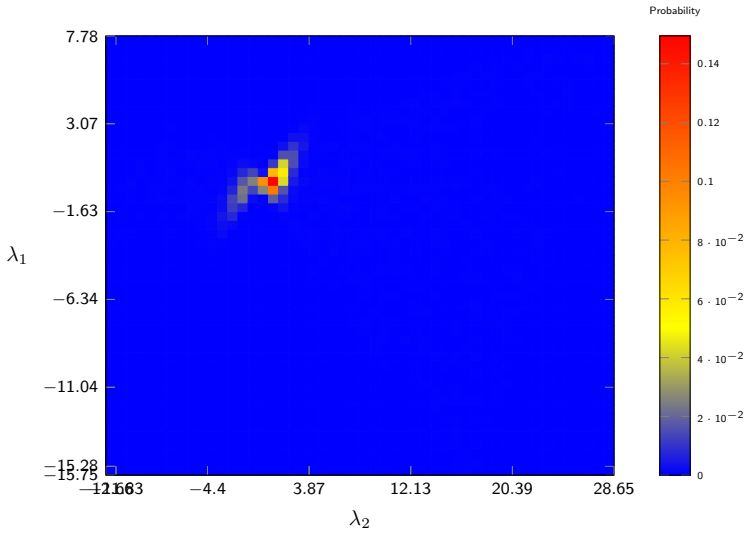

Figure 5.14: Vessel Probability Density Function (Normalised histogram in Figure 5.8). The sum of the entries (probabilities) is equal to One.

unit-entry is blurred using the method described in Section 5.5.2 yielding the smoother histogram shown in Figure 5.15.

5.7 Vessel posterior probability

Based on Bayes' rule outlined in Equation 5.9 (p. 79), prior probability and likelihood estimations for the classes under consideration are essential to estimate the posterior

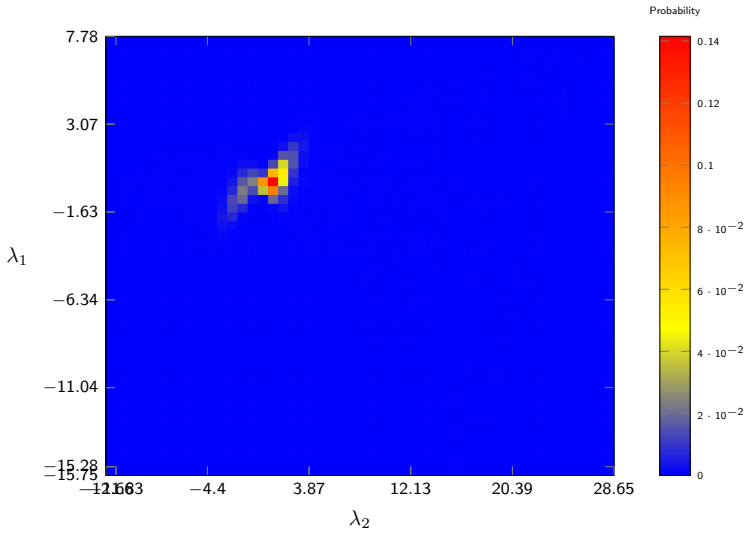

Figure 5.15: Smoothed background probability density function

probability. Vessel and non-vessel denoted as background are the two classes in the proposed Bayesian labelling approach.

The prior probability $P(V)$ is estimated using the background extraction method described in Chapter 4. The method estimates the vessel-pixel density by subtracting the estimated background from the initial image. Post processing work yields a segmented vessel-network approach represented by a binary image from where the normalised vessel-pixel density is estimated yielding the prior vessel probability $P(V)$. Since both classes are regarded as mutually exclusive, the prior background probability is defined as $1 - P(V)$.

Vessel- and background-likelihood estimations were described in Sections 5.5 and 5.6 using synthetic vessel images and Monte Carlo simulations. The process to estimate the likelihood is connected to the background estimation process due to the mean background contrast and noise estimations are essential to generate synthetic images.

Having all the prior probabilities and likelihoods calculated, the *posterior* vessel probability $P(V|\underline{\lambda})$ can be estimated by solving Baye's rule. The method used to locally estimate the posterior vessel probability as a labelling approach is described in the next section.

5.7.1 Retinal image normalisation

Unlike the studied vessel detectors in [35, 73, 106], we do not use the original image for the labelling. The initial image, which is the Green component of the RGB colour space, is normalised to reduce the light variation effect in the image. The normalised initial image is then used by the labelling method.

The normalisation method aims to correct contrast variation in the original image. The method uses the estimated background detailed in Chapter 4 which is based on statistical methods to estimate the contrast behind vessel structures by analysing neighbours. The normalised contrast is given by Equation 5.14 where $\mathscr{E}$ is a normalising ratio (see Equation 5.15) calculated from the estimated background contrast image.

$$N(x,y) = \mathscr{E} \cdot I(x,y) \tag{5.14}$$

$$\mathscr{E} = \frac{\overline{C}}{E(x,y)} \tag{5.15}$$

where $\overline{C}$ is the mean background contrast and $E(x,y)$ the local background estimate.

The ratio $\mathscr{E}$ aims to balance the contrast. It enhances the contrast when the difference between the mean contrast is bigger than the estimated local background contrast. Conversely, the ratio reduces the contrast when the mean is smaller than the locally estimated contrast. In Figure 5.16, a retinal image (the Green component only) and its normalised version are presented.

Histograms shown in Figures 5.16(c), (d) describe contrast variation in the images. Histograms are normalised for their comparison. Contrast distribution in the original image exhibits an asymmetrical behaviour. On the other hand, the normalised image presents a smoother behaviour. Even though the graph is clearly not bimodal, it can be decomposed into two Gaussians suggesting the distribution of vessel- and background-pixel contrast. Gaussian Mixture Model (GMM) was applied to fit two Gaussians to the histogram in the normalised image as shown in Figure 5.17.

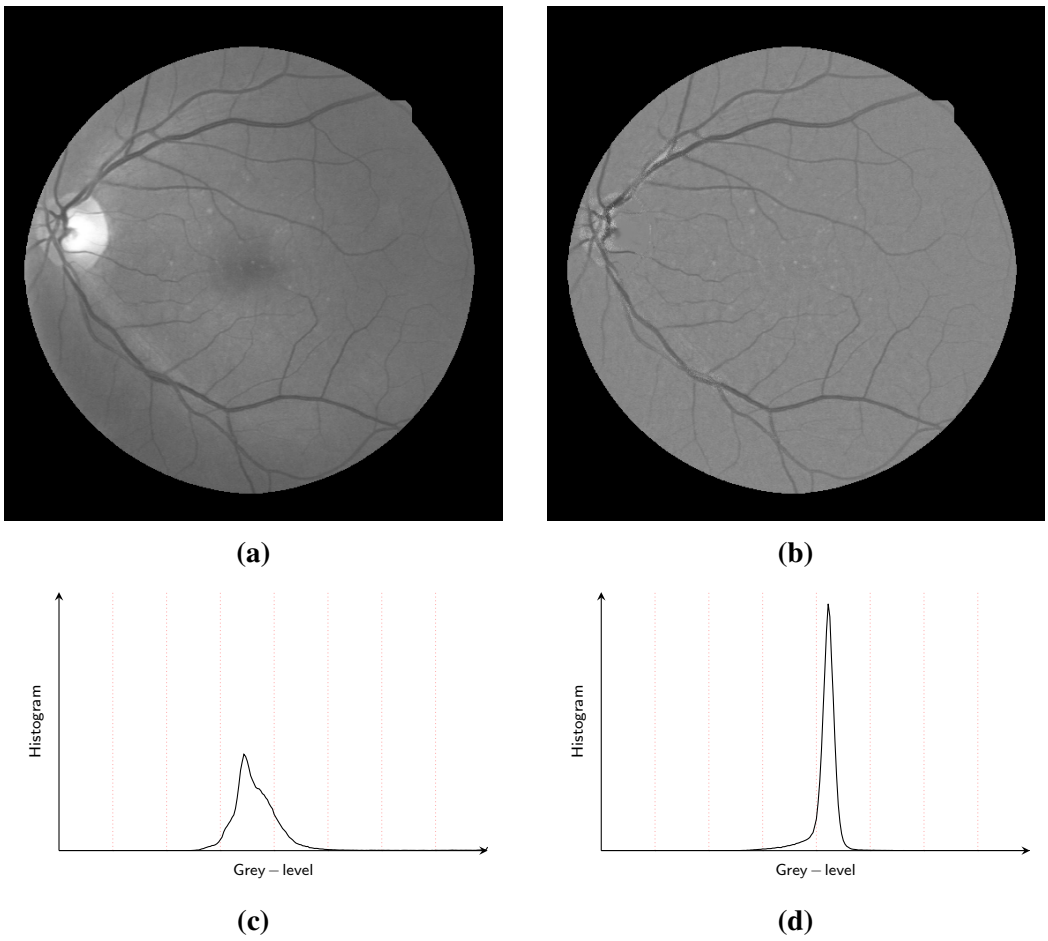

Figure 5.16: Retinal image normalisation, DRIVE [110] image sample: (a) Green component of the RGB colour space; (b) normalised image; and, (c), (d) normalised histogram.

.

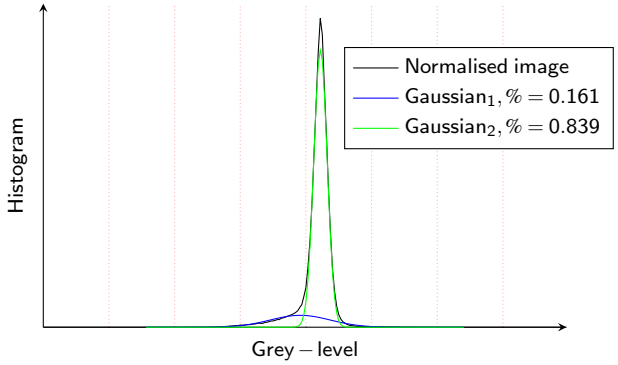

Figure 5.17: Gaussian decomposition for the normalised image histogram. The first Gaussian (plot in green) covers 0.839% of the Gaussian mixture model, and the second Gaussian (plot in blue) covers the 0.161% of the model.

5.8 Vessel-pixel labelling

The vessel-pixel labelling method is based on a Bayesian approach where the image being labelled is given by normalising the retinal image. Here, the normalisation process detailed in Section 5.7 is implemented to reduce contrast variation. As described in previous sections, components of Bayes' rule are calculated independently for the image being treated. The labelling process can be implemented after the components of Bayes' rule are calculated and the retinal image normalised.

The labelling method is based on the scale-space representation [66] to cope with the labelling of vessel structures at a range of diameters. The Hessian matrix of the scaled images is calculated; eigenvalues are placed in ascending order of their magnitude as suggested in [35]. Selection of eigenvalues across scales is based on the Frangi [35] criteria as follows. The Frangi [35] formula is applied to the eigenvalues and, following the Frangi criteria to select the best response across scales, the eigenvalues $\underline{\lambda}$ belonging to the best scale-response are selected by the labelling method. Eventually, the *posterior* vessel probability is calculated for the selected $\underline{\lambda}$ using Bayes' rule. The process is repeated to label all pixels in a given image.

Likelihood estimates can be described as lookup tables where eigenvalues are the input and the estimated probability for the provided pair (λ_1, λ_2) is the output. Therefore, *posterior* vessel estimates may vary due to the number of bins defined in the likelihood configuration. Large number of bins may produce small *posterior* probability estimates as the number of entries in the likelihood is spread out. Conversely, small number of bins may increase the *posterior* probability estimates where the likelihood presents large concentrations. There is thus a trade-off between the number of bins in the likelihood and the smoothness of the *posterior* probability estimates. The labelling produced by using two likelihood configurations is shown in Figure 5.18.

Posterior vessel estimates in Figure 5.18(b), where λ_1 and λ_2 were grouped into 150 bins over each of the ranges, seem to be higher than the estimates in Figure 5.18(b), where the likelihood configuration grouped the eigenvalues into 25 bins (5-bins over each eigenvalue's range). Note that this is a the visual effect produced when data are converted into an 8-bit image as probabilities are scaled into the range $[0...255]$ intensity values.

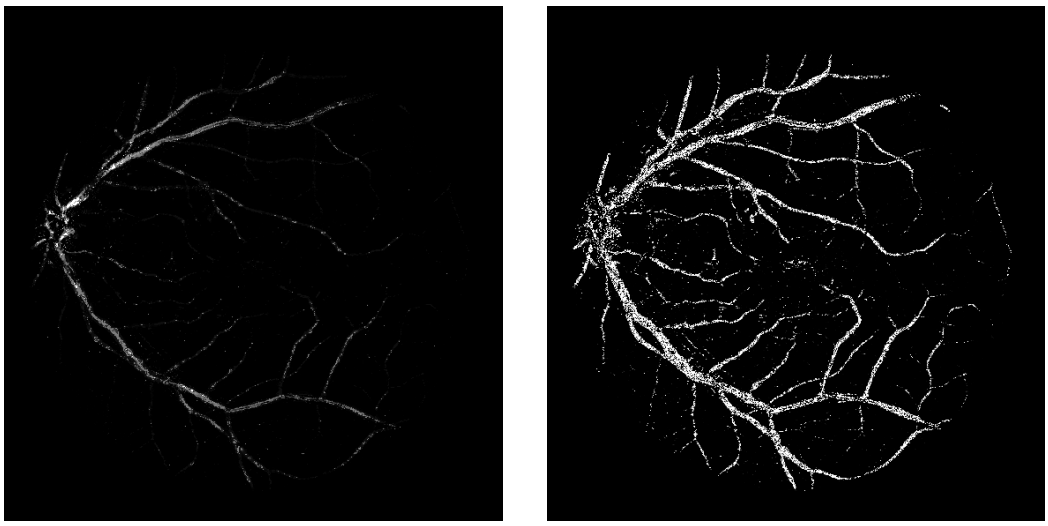

(a) **(b)**

Figure 5.18: Maximum *posterior* vessel probability using: (a) 5 bins in each of eigenvalue's range, and (b) 150 bins.

.

Bright similarity among the labelled pixels in Figure 5.18(b) suggests that the *posterior* estimates are also similar. Figure 5.18(a) shows brighter areas in big vessel structures suggesting the *posterior* vessel probability is higher in those regions which can be interpreted as having stronger 'vesselness'.

A quantitative analysis of the proposed Bayesian vessel-pixel labelling method is detailed in Section 5.9 to measure the performance of the proposed labelling method. Likelihood configurations were analysed due to the labelling performance and the best configuration was compared with the Frangi [35] vessel detector using receiver operating characteristic (ROC) plots.

5.9 Quantitative analysis of the labelling

Measures of overlap of labelled regions in an image and the ground truth, such as Jaccard and Dice coefficients, have been extensively used to evaluate segmentation algorithms in medical image analysis. We know the ground truth in the used retinal images is formed by a binary image where pixels within desired objects are labelled as 1 and the remaining pixels as 0. The proposed vessel-pixel labelling method uses the estimated vessel posterior probability to generate the resulting labelled image. Hence,

vessel-label estimates range between 0 and 1, being the lowest value taken as fully background and the highest value as vessel.

A method to compare the resulting labelled image with the ground truth is required to the measure the performance of the labelling method. Both images should be within the same domain for a fair comparison. A simple method is, converting the labelled image into a binary image and compute the agreed pixels to estimate an agreement measure. Image thresholding is a simple method to separate pixels by analysing their intensities using a threshold. The method aims to convert the labelled-image into a binary-image where intensities pixels above the selected threshold are set to 1—desired objects—and those below the threshold are set to 0—unwanted objects, usually background. Nonetheless, the problem exists in the method to select the threshold that best approximates the segmentation to the ground truth which eventually yields the best agreement.

Receiver Operating Characteristic (ROC) plot—a technique to visualise the performance of classifiers [32]—was used to measure the performance of the labelling by varying the threshold producing binary images that were compared with the ground truth. Having both images in the same domain (binary), the true positive (TPR) and false positive (FPR) rates were estimated to construct ROC curve. Estimation of the Area Under the Curve (AUC) yields a statistical measure for the ROC plot, which eventually was regarded as the performance. AUC is a fraction of the unit-square of the ROC plot, so it ranges between 0 and 1. As the ROC curve approximates the upper left corner (100% TPR, 100% FPR), the AUC approximates to 1—perfect classification—meaning better the performance.

ROC plots for the labelled images in Figure 5.18—using two configurations for the PDF estimation—are compared in Figure 5.19. In the figure, the performance using only 25-bins (5 bins for each eigenvalue's range of measures) to form the probability density function, exhibits a better performance than the second configuration (150 by 150 bins).

The number of thresholds used in the ROC plot is limited to the number of bins used in the PDF. This may produce a less continuous graph when the PDF is set up using fewer bins as shown in the blue graph in Figure 5.19.

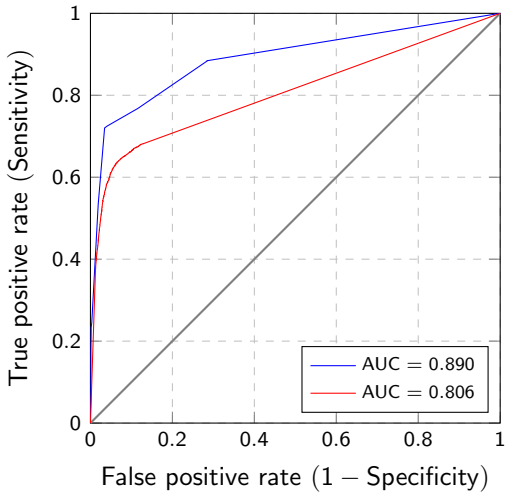

Figure 5.19: ROC plot for two configurations in the probability density function estimation. Graph in blue, 5 bins at the range of λ_1 measures and 5 bins at the range of λ_2 measures (AUC=0.890); and, graph in red, 150 bins in each of the eigenvalue measures (AUC=0.806).

The overall performance of the labelling was measured by varying the configuration of probability density function (PDF). The resulting AUC for each of the configurations is summarised in Figure 5.20. In the figure, axes are given by the number of bins used to group the measured eigenvalues ($[5, 25, 50, 75, 100, 125, 150, 175, 200]$), and the $z-axis$ mirrors the AUC obtained for every configuration. The computed AUCs varies from 0.75 to 0.90 in the analysed image.

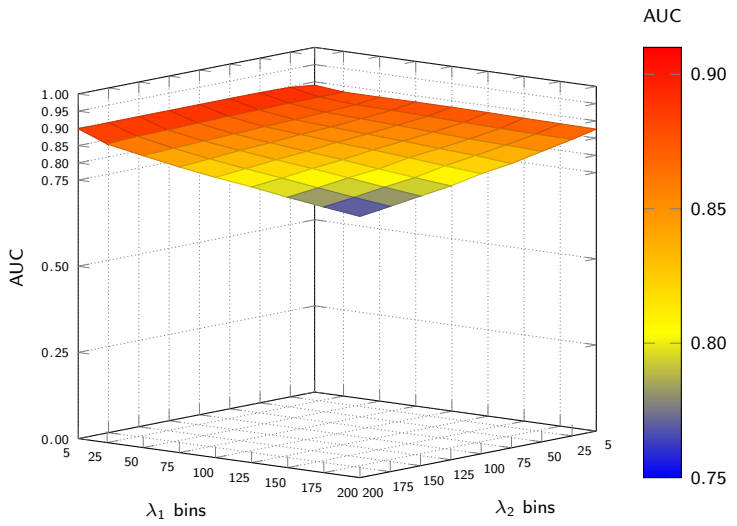

Figure 5.20: AUC summary for different initial configurations for the probability density function estimation.

Eigenvalues are in ascending order by their magnitude, so λ_1 measures are near zero. Thus, the range of λ_1 measures is usually small. The range of λ_2 measures is

larger since it describes the principal local curvature given by the vessel width which varies from 1 to 15-pixel units in the synthetic images. As shown in Figure 5.20, increasing the number of λ_1-bins severely reduces the AUC. On the other hand, the range of λ_2 measures allows—at some extent—a better distribution for a selected number of λ_1-bins. Better AUCs were computed using a reduced number of λ_1-bins.

The performance obtained using 5 λ_1-bins—the best λ_1 configuration—and varying the number of bins in λ_2 is summarised in Figure 5.21. As shown in the figure, there is a little to choose between the λ_2-bins from 50 to 150.

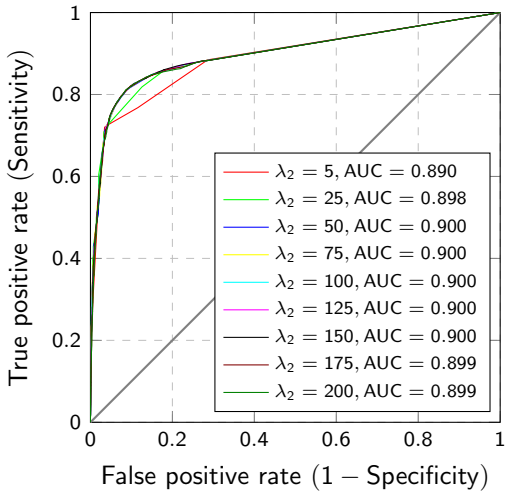

Figure 5.21: ROC plot for 5 bins in λ_1 measures and all λ_2-bin configurations.

The maximum AUC obtained was compared with the Frangi's [35] performance. In order to make the performance comparison fair, both methods used the normalised image as input. Computing of AUC was based on the ground truth to estimate the true positive and false positive rates used for ROC plots. The performance obtained with the proposed probabilistic labelling method was $AUC = 0.900$ while Frangi's method reached $AUC = 0.925$. ROC plots are shown in Figure 5.22.

It is important to review the resulting labelled images to judge the performance of the labelling methods. Analysis of the labelling outcomes, the normalised-input image and the ground truth can be used to support the measured performance AUC. The resulting labelled images for both, the proposed probabilistic labelling and Frangi's [35] method, are presented in Figure 5.23 (p. 104) for a sample image from the DRIVE [110] database. Analysis of the labelled images is discussed in the next section.

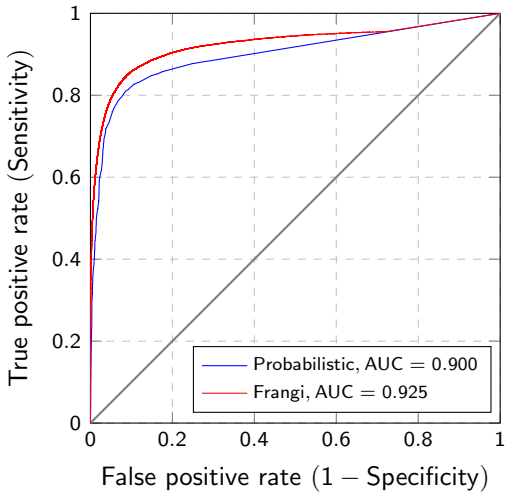

Figure 5.22: Proposed probabilistic labelling vs. Frangi [35] performance

5.10 Discussion

The proposed probabilistic vessel-pixel labelling method relies on prior probabilities estimations obtained from an initial analysis of the image and a model used to analyse the behaviour of selected local features. Firstly, an initial vessel-pixel density is estimated using a proposed background extraction method. The approach aims to estimate the contrast (background) of pixels behind vessel structures. A simple image-subtraction and global-threshold segmentation were used to separate the vessel structures from the estimated background yielding a basic vessel network segmentation. The global thresholding segmentation, however, reduces the number of vessel-pixels as pixels bordering vessel structures are usually classified as background rather than vessels. Intensities of vessel-bordering pixels are better approximated by the average background, so the global-thresholding misclassifies those pixels. Underestimating the *prior* vessel probability influences on the estimation of *posterior* vessel probabilities. Compensation for loss of bordering pixels may improve *posterior* estimates.

Secondly, the method used to estimate the likelihood is based on features from the image being treated. Mean contrast, and power-of-noise are some estimates influencing features of synthetic images which eventually produce the likelihood for a given image. Misestimating those values may propagate an underestimation to the posterior probabilities.

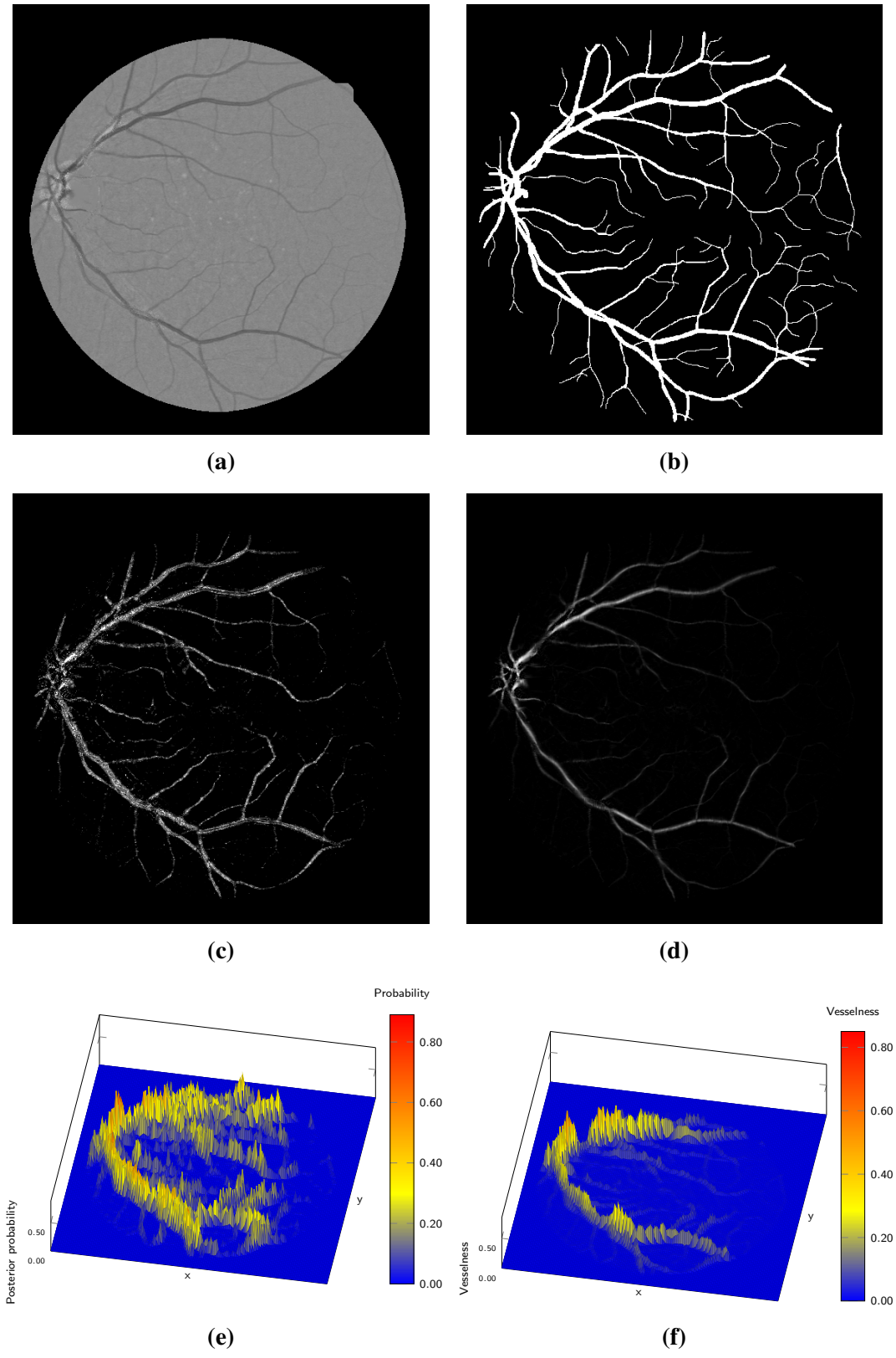

Figure 5.23: Comparative of labelling approaches: (a) Normalised-input image, (b) ground truth, (c) proposed probabilistic labelling, (d) Frangi [35], and (e), (f) 3D view of the resulting labelling.

The model used to produce synthetic images idealises vessels as cylindrical straight objects. We assumed that vessels lie in a plane and can be imaged normal to their longitudinal direction. Nonetheless, in reality, fundus eye photography image vessel structures uses light reflected by the retina which has a degree of concavity. In addition, it is highly likely that vessels will present orientation variations. These and other conditions such overlapping introduce a component to the 2D images that make the enhancement of vessel pixels difficult.

Configuration of the probability density function—termed likelihood—is another factor affecting accuracy of the *posterior* vessel estimates. Changes in the number of bins for each eigenvalue measure vary the *posterior* estimations. For a large number of bins, even though all vessel pixels were labelled, *posterior* probabilities are small that the overall performance drops to AUC=0.75, 1 being the perfect performance. Small numbers of bins in λ_1 exhibit a better performance. Results are fairly alike for the number of bins in λ_2 when combined with a reduced number of bins in λ_1.

5.11 Conclusions

Details of the proposed probabilistic vessel-pixel labelling was provided in this chapter. We used a physics-based model of the process by which the image of a vessel is formed. The model provides a framework to generate synthetic vessel images which were used to analyse low-level features with Monte Carlo simulations in order to enhance vessel structures in retinal images.

The proposed probabilistic labelling method relies on other estimated probabilities. Firstly, the *prior* vessel probability is estimated using a proposed background extraction method. Based on further analysis of a normalised-image's histogram, distributions of intensities were modelled by Gaussian distributions as vessel- and background-like pixels. The analysis suggests that the vessel-pixel density was underestimated by the initially used method. Secondly, light absorption coefficient is one of the parameters used to generate synthetic images to estimate the likelihood. Varying

the coefficient may produce more errors due to noise affecting the vessel pixels. Eventually, underestimation of probabilities is propagated to the *posterior* vessel probability estimates.

The proposed probabilistic labelling produced $AUC = 0.9$ being $AUC = 1$ the perfect performance. The meaning of the performance is difficult to interpret in medical image analysis since it is a statistical measure. It is well known, for instance, that some vessel detectors based on line-detection methods have problems with junctions and bifurcations, which can produce a qualitative low performance for some purposes in medicine. Nonetheless, this value can be used to compare with other approaches under similar conditions. Results were compared with Frangi [35], a much-used vessel detector algorithm, under the same criteria to form the resulting labelled image. Frangi's performance was $AUC = 0.925$. Even though our probabilistic labelling approach did not outperform Frangi in the experiments, in the next chapter some information suggesting future work may improve our results is detailed.

Chapter 6

Conclusions and future directions

In this thesis, we presented a novel vessel-pixel labelling based on Bayes' rule for enhancement of multi-scale vessel structures in eye fundus images. Unlike many current vessel detectors, our approach is based on a probabilistic approach to label pixels with the estimated probability of falling within the central section of a vessel structure. Our approach combines local low-level- and global- features to estimate the maximum posterior vessel probability.

In this chapter we summarise the main contributions of this work and discuss future work.

6.1 Contributions

First, we measured the performance of some much-used vessel detectors in order to select the one showing the best performance. The aim of the study was to select a vessel detector to fairly compare our probabilistic labelling method under the same conditions. Frangi [35] showed the best performance under constrained conditions. The resulting analysis yielded a conference paper publication.

Second, we proposed a local background estimation method based on statistical analysis of the intensities of neighbouring pixels. The method aimed at background contrast estimation by analysing randomly selected neighbour pixels, and the group of pixels showing the most uniform behaviour was selected to estimate the contrast. Even though the re-estimation carried out along the optic disc bounds was based on a manual method to locate the region, the background estimates were enhanced. Automated optic disc location is suggest and discussed in the next section.

Third, unlike many studied vessel detector approaches, we used the green component only, of the RGB colour space, from images in our experimentation. We formulated an image normalisation that reduced contrast variation across the image. The resulting normalised image was eventually used for the labelling.

Four, a solid physics-based model was proposed to generate synthetic images. The model mimics the process by which the image of a vessel is formed. The model was used to mirror the eye fundus imaging process, and assumes light absorption by eye tissue is uniform. Synthetic images were generated using variates such as noise and orientation to cover possible feature values in real images.

Five, the probabilistic method was fairly compared with Frangi vessel detector. Both approaches are based on multi-space image representation to cope with detection of vessels at a range of diameters, compute the Hessian matrix and use eigenvalues to describe the principal local curvature. Even though the performance of our approach was unable to outperform the Frangi detector, there are some suggestions discussed in the next section promising better results.

6.2 Future work

Our proposed vessel labelling approach is based on realistic models to generate synthetic images and probabilistic methods for using Bayes' rule as probabilistic approach. The overall performance achieved .9 out of 1. There are further refinements that can achieve improvements in some sections of the process to produce better labelling.

Analysis of the histogram of normalised images suggested that vessel-pixel density, taken as *prior* vessel probability, was underestimated. A more solid method than

the two-class global thresholding segmentation might better approximate the vessel density estimation if bordering pixels are weighted and classified as vessels.

An automated-optic-disc location method can be integrated into our approach to make the background estimation a human-interaction independent tool. Also, further analysis around the re-processed region can reduce fragmentation of vessels that follow orientation of the used scan-line to re-estimate the background contrast.

Tuning of the absorption coefficient, a parameter to generate synthetic vessel images, may vary the likelihood estimations. By decreasing the absorption coefficient, the signal is prone to being affected by noise. The number of trials used in Monte Carlo simulations can better describe vessel features—eigenvalues—due to the number of variates (such as power-of-noise and vessel diameter) to cover all possible values presented in real images.

The ground truth does not penalise light reflections produced along the central section of some main vascular structures. Our approach, however, labelled those pixels with smaller probability producing labelling of parallel narrow structures. This issue may represent a reduction on the quantitative performance.

Appendix A

2D-Histogram smoothing using a triangular distribution function

The triangular smooth is a smoothing algorithm based on a weighted smoothing function. The method replaces each point in the signal with the estimated value given by a triangular function covering an n adjacent points termed smooth width. Usually n is an odd number yielding a symmetrically balanced triangle function around the central point—the point to be replaced.

In 1D-dataset and three-point smooth denoted by $n = 3$, for instance, the estimated replacing value is given by $(Y_{-1} + 2Y_0 + Y_{+1})/4$, where Y_i is the response of the adjacent points. When the resulting value is equal to the original data, the smoothing results in a unit-gain smooth. In 1D, for instance, it can be described as a straight line, where the central- and adjacent-points have the same value. In the example described above, there is assumed x-axis intervals in the dataset being uniform allowing to preserve the triangular function symmetrically balanced.

The method can be extended to smooth 2D-data by combining triangular functions, where they can be dimensionally distinct one from the other. The smoothing

process remains valid by sliding the 2D-smoothing function over the data where the function is centrally placed on every cell in the 2D-data to estimate its replacing value.

The proposed histogram-smoothing method, however, does not intend to smooth the counts in the 2D-dataset of a histogram. The aim of the proposed method is, rather than increasing by 1 the bin's counts where a sample falls, the entry is blurred into the histogram by estimating the gain for both, the current- and the adjacent-bins.

A pyramid-shaped element is centrally located on the sample's position. Length and width of the element are given by the bin size where the sample falls. In the ideal but most-likely unrealistic case, if a sample falls at the central point of a bin the pyramid-shaped element matches the bin boundaries producing a unit-gain since the volume under the element is normalised and taken as 1.

If a sample does not fall at the central point of a bin, the pyramid element overlaps adjacent bins. The method then estimates the volume of the pyramid—gain—sharing with the adjacent bins. Eventually, the estimated gains are counted into their corresponding bins. Figure A.1(a) illustrates how the base of the pyramid element overlaps three adjacent bins. In the figure, the fraction of the pyramid falling into each of the overlapping regions denoted by $\{a,b,c,d\}$ contributes to the overlapped bin.

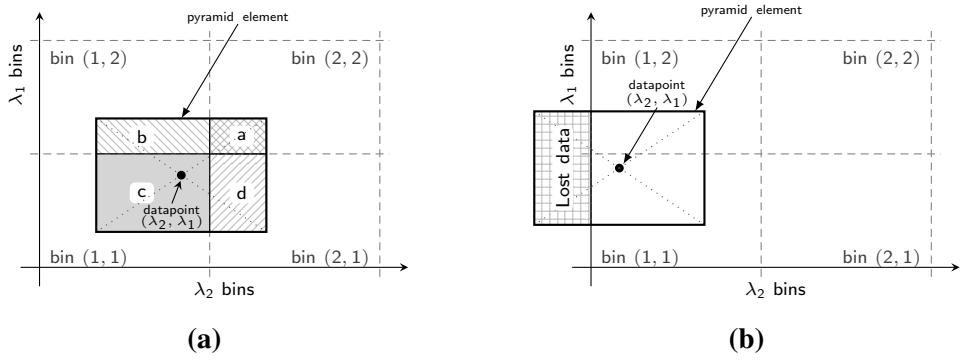

Figure A.1: Smoothing histogram entries. (a) The unit-gain of a sample (λ_2,λ_1) is shared with the adjacent bins overlapped by the pyramid element. The fraction volume of the pyramid falling within the regions a,b,c, and d contributes to their bins. (b) A sample (λ_2,λ_1) falling within the histogram bounds producing loss of fractional entries.

This method of distributing the unit-gain is also employed at the end of the histogram range such that a sample which falls within the histogram bounds may be partially accumulated into the histogram producing loss of fractional entries as shown in Figure A.1(b).

Bibliography

[1] Michael D. Abràmoff, Mona K. Garvin, and Milan Sonka. Retinal imaging and image analysis. *IEEE Reviews in Biomedical Engineering*, 3:169–208, 2010.

[2] Carla Agurto, Vinayak Joshi, Sheila Nemeth, Peter Soliz, and Simon Barriga. Detection of hypertensive retinopathy using vessel measurements and textural features. In *Proceedings of the 36th Annual International Conference of the IEEE Engineering in Medicine and Biology Society*, pages 5406–5409, August 2014.

[3] Edwin G. A. Aird. *An Introduction to Medical Physics*. William Heinemann Medical Books, 1975.

[4] Stephen R. Aylward, Julien Jomier, Sue Weeks, and Elizabeth Bullitt. Registration and analysis of vascular images. *International Journal of Computer Vision*, 55:123–138, 2003.

[5] Michelle L. Baker, Peter J. Hand, Jie Jin Wang, and Tien Y. Wong. Retinal signs and stroke: revisiting the link between the eye and brain. *Stroke*, 39(4):1371–1379, April 2008.

[6] Michelle L. Baker, Jie Jin Wang, Gerald Liew, Peter J. Hand, Deidre A. De Silva, Richard I. Lindley, Paul Mitchell, Meng-Cheong Wong, Elena Rochtchina, Tien Y. Wong, Joanna M. Wardlaw, Graeme J. Hankey, and Multi-Centre Retinal Stroke Study Group . Differential associations of cortical and subcortical cerebral atrophy with retinal vascular signs in patients with acute stroke. *Stroke*, 41(10):2143–2150, October 2010.

[7] John J. Bartko. Measurement and reliability: Statistical thinking considerations. *Schizophrenia Bulletin*, 17(3):483–489, 1991.

[8] Timothy J. Bennett and Chris J. Barry. Ophthalmic imaging today: an ophthalmic photographer's viewpoint – a review. *Clinical and Experimental Ophthalmology*, 37(1):2–13, 2009.

[9] Abhir Bhalerao, Sarabjot Singh Anand, and Ponnusamy Saravanan. Retinal fundus image constrast normalization using mixture of gaussians. In MB Matthews, editor, *42nd Asilomar Conference on Signals, Systems and Computers*, volume Volume 1-4, pages 647–650. IEEE Computer Society, 2008.

[10] Catey Bunce and Richard Wormald. Leading causes of certification for blindness and partial sight in England and Wales. *BioMed Central Public Health*, 6(58):1–7, October 2006.

[11] Catey Bunce, Wen Xing, and Richard Wormald. Causes of blind and partial sight certifications in England and Wales: April 2007–March 2008. *Eye*, 24(11):1692–1699, 2010.

[12] Ivo Buschmann and Wolfgang Schaper. The pathophysiology of the collateral circulation (arteriogenesis). *Journal of Pathology*, 190(3):338–42, 2000.

[13] Gerald J. Chader and Allen Taylor. Preface: The aging eye: Normal changes, age-related diseases, and sight-saving approaches. *Investigative Ophthalmology and Visual Science*, 54(14), 2013.

[14] Subhasis Chaudhuri, Shankar Chatterjee, Norman Katz, Mark Nelson, and Michael Goldbaum. Detection of blood vessels in retinal images using two-dimensional matched filters. *IEEE Transactions on Medical Imaging*, 8(3):263–269, 1989.

[15] Hongyu Y. Chen, Melissa M. Rogalski, and Jeffrey N. Anker. Advances in functional X-ray imaging techniques and contrast agents. *Physical Chemistry Chemical Physics*, 14(39):13469–13486, 2012.

[16] Ariel Choukroun and Vincent Charvillat. Bucketing techniques in robust regression for computer vision. In Josef Bigun and Tomas Gustavsson, editors, *Image Analysis*, volume 2749 of *Lecture Notes in Computer Science*, pages 609–616. Springer Berlin Heidelberg, 2003.

[17] Radim Chrástek, Matthias Wolf, Klaus Donath, Heinrich Niemann, Torsten Hothorn, Berthold Lausen, Robert Lämmer, Christian Y. Mardin, and Georg Michelson. Automated segmentation of the optic nerve head for diagnosis of glaucoma. *Medical Image Analysis*, 9(4):297–314, August 2005.

[18] Katy L. Cooper, Yang Meng, Susan Harnan, Sue E. Ward, Patrick Fitzgerald, Diana E. Papaioannou, Lynda Wyld, Christine Ingram, Iain D. Wilkinson, and Eleanor Lorenz. Positron emission tomography (PET) and magnetic resonance imaging (MRI) for the assessment of axillary lymph node metastases in early

breast cancer: systematic review and economic evaluation. *Health Technology Assessment*, 15(4):1–134, 2011.

[19] Arnold R. Cowen. Cardiovascular X-ray imaging: Physics, equipment and techniques. In Peter Lanzer, editor, *Catheter-Based Cardiovascular Interventions. A Knowledge-Based Approach*, pages 203–259. Springer, 2013.

[20] William R. Crum, Oscar Camara, and Derek L. G. Hill. Generalized overlap measures for evaluation and validation in medical image analysis. *IEEE Transactions on Medical Imaging*, 25(11):1451–1461, 2006.

[21] UK Department of Health. Ten things you need to know about long term conditions, April 2008.

[22] UK Government Department of Health. *Long Term Conditions Compendium of Information*. Department of Health, UK Government, third edition, May 2012.

[23] Lee R. Dice. Measures of the amount of ecologic association between species. *Ecology*, 26(3):297–302, 1945.

[24] Geoff Dougherty, Michael J. Johnson, and Matthew D. Wiers. Measurement of retinal vascular tortuosity and its application to retinal pathologies. *Medical and Biological Engineering and Computing*, 48(1):87–95, January 2010.

[25] Allen B. Downey. *Think Bayes: Bayesian Statistics Made Simple*. Green Tea Press, Needham, MA, USA, 2012.

[26] Klaus Drechsler and Cristina Oyarzun Laura. Comparison of vesselness functions for multiscale analysis of the liver vasculature. In *Proceedings of the 10th IEEE International Conference on Information Technology and Applications in Biomedicine*, pages 1–5, Corfu, Greece, 2010.

[27] Wolfgang Drexler and James G. Fujimoto. State-of-the-art retinal optical coherence tomography. *Progress in Retinal and Eye Research*, 27(1):45–88, 2008.

[28] Richard O. Duda and Peter E. Hart. *Pattern Classification and Scene Analysis*. John Willey and Sons, New York, USA, 1973.

[29] Oleksandr P. Dzyubak and Erik L. Ritman. Automation of Hessian-based tubularity measure response function in 3D biomedical images. *International Journal of Biomedical Imaging*, 2011(1):1–16, 2011.

[30] David Eberly, Robert Gardner, Bryan Morse, Stephen Pizer, and Christine Scharlach. Ridges for image analysis. *Journal of Mathematical Imaging and Vision*, 4(4):353–373, 1994.

[31] Robert H. Eikelboom, Kanagasingam Yogesan, Chris J. Barry, Ian J. Constable, Mei–Ling Tay–Kearney, Ludmila Jitskaia, and Philip H. House. Methods and limits of digital image compression of retinal images for telemedicine. *Investigative Ophthalmology and Visual Science*, 41(7):1916–1924, 2000.

[32] Tom Fawcett. An introduction to ROC analysis. *Pattern Recognition Letters*, 27(8):861–874, 2006.

[33] Samuele Fiorini, Lucia Ballerini, Emanuele Trucco, and Alfredo Ruggeri. Automatic generation of synthetic retinal fundus images. In *Proceedings of the 18th Medical Image Understanding and Analysis*, 2014.

[34] Martin A. Fischler and Robert C. Bolles. Random sample consensus: A paradigm for model fitting with applications to image analysis and automated cartography. *Communications of the Association for Computing Machinery (ACM)*, 24(6):381–395, June 1981.

[35] Alejandro F. Frangi, Wiro J. Niessen, Koen L. Vincken, and Max A. Viergever. Multiscale vessel enhancement filtering. In William Wells, Alan Colchester, and Scott Delp, editors, *Medical Image Computing and Computer-Assisted Intervention*, volume 1496 of *Lecture Notes in Computer Science*, pages 130–137, Cambridge, MA, USA, 1998. Springer Berlin Heidelberg.

[36] Muhammad Moazam Fraz, Sarah A. Barman, Paolo Remagnino, Andreas Hoppe, A. Basit, Bunyarit Uyyanonvara, Alicja R. Rudnicka, and Christopher G. Owen. An approach to localize the retinal blood vessels using bit planes and centerline detection. *Computer Methods and Programs in Biomedicine*, 108(2):600–616, 2012.

[37] Muhammad Moazam Fraz, Paolo Remagnino, Andreas Hoppe, Bunyarit Uyyanonvara, Alicja R. Rudnicka, Christopher G. Owen, and Sarah A. Barman. Blood vessel segmentation methodologies in retinal images – A survey. *Computer Methods and Programs in Biomedicine*, 108(1):407–433, 2012.

[38] Andrew Gelman, John B. Carlin, Hal S. Stern, and Donald B. Rubin. *Bayesian Data Analysis*. Texts in Statistical Science. Chapman and Hall/CRC, second edition, 2003.

[39] Andrea Giachetti, Lucia Ballerini, and Emanuele Trucco. Accurate and reliable segmentation of the optic disc in digital fundus images. *Journal of Medical Imaging*, 1(2):024001, 2014.

[40] Rafael C. Gonzalez and Richard E. Woods. *Digital Image Processing*. Prentice Hall, second edition, 2002.

[41] Ali Gooya, Hongen Liao, Kiyoshi Matsumiya, Ken Masamune, Yoshitaka Masutani, and Takeyoshi Dohi. A variational method for geometric regularization of vascular segmentation in medical images. *IEEE Transactions on Image Processing*, 17(8):1295–1312, August 2008.

[42] Boris I. Gramatikov. Modern technologies for retinal scanning and imaging: an introduction for the biomedical engineer. *BioMedical Engineering OnLine*, 13(1):1–35, 2014.

[43] Robert M. Haralick. Ridges and valleys on digital images. *Computer Vision, Graphics, and Image Processing*, 22(1):28–38, 1983.

[44] Robert M. Haralick, Layne T. Watson, and Thomas J. Laffey. The topographic primal sketch. *International Journal of Robotics Research*, 2(1):50–72, 1983.

[45] William E. Hart, Michael Goldbaum, Brad Côté, Paul Kube, and Mark R. Nelson. Measurement and classification of retinal vascular tortuosity. *International Journal of Medical Informatics*, 53(2-3):239–252, 1999.

[46] Michael R. Hee, Joseph A. Izatt, Eric A. Swanson, David Huang, Joel S. Schumun, Charles P. Lin, Carmen A. Puliafito, and James G. Fujimoto. Optical coherence tomography for ophthalmic imaging: new technique delivers micron-scale resolution. *IEEE Engineering in Medicine and Biology Magazine*, 14(1):67–76, 1995.

[47] Amanda D. Henderson, Beau B. Bruce, Nancy J. Newman, and Valérie Biousse. Hypertension-related eye abnormalities and the risk of stroke. *Reviews in Neurological Diseases*, 8(1–2):1–9, 2011.

[48] David Huang, Eric A. Swanson, Charles P. Lin, Joel S. Schuman, William G. Stinson, Warren Chang, Michael R. Hee, Thomas Flotte, Kenton Gregory, Carmen A. Puliafito, and James G. Fujimoto. Optical Coherence Tomography. *Science*, 254(5035):1178–1181, 1991.

[49] Yi-Jun Huang and Wei-Jun Liu. Robust estimation for the fundamental matrix based on LTS and bucketing. In *Proceedings of the International Conference on Wavelet Analysis and Pattern Recognition 2009*, pages 486–491, July 2009.

[50] Syed Tahir Hussain, Roy E. Smith, A. L. Clark, and Richard F. M. Wood. Blood flow in the lower limb after balloon angioplasty of the superficial femoral artery. *British Journal of Surgery*, 83(6):791–795, 1996.

[51] C. Richard Keeler. The ophthalmoscope in the lifetime of Hermann von Helmholtz. *Archives of Ophthalmology*, 120(2):194–201, 2002.

[52] Cemil Kirbas and Francis K.H. Quek. Vessel extraction techniques and algorithms: a survey. In *Proceedings of the 3rd IEEE Symposium on BioInformatics and BioEngineering*, pages 238–245, March 2003.

[53] Thomas M. Koller, Guido Gerig, Gábor J. Székely, and D. Dettwiler. Multiscale detection of curvilinear structures in 2-D and 3-D image data. In *Proceedings of the 5th International Conference on Computer Vision*, pages 864–869, Cambridge, MA, USA, 1995. IEEE.

[54] Karl Krissian, J. Ellsmere, K. Vosburgh, R. Kikinis, and C. F. Westin. Multiscale segmentation of the aorta in 3D ultrasound images. In *Proceedings of the 25th Annual International Conference of the IEEE Engineering in Medicine and Biology Society*, volume 1, pages 638–641, Cancun, Mexico, 2003.

[55] Karl Krissian, Grégoire Malandain, Nicholas Ayache, Régis Vaillant, and Yves Trousset. Model-based detection of tubular structures in 3D images. *Computer Vision and Image Understanding*, 80(2):130–171, 2000.

[56] Sehmi Kulwant. Red-free photography of the retina. *Journal of Audiovisual Media in Medicine*, 5(4):142–144, 1982.

[57] Antoine Lafuma, Antoine Brézin, Stefania Lopatriello, Klaus Hieke, Julia Hutchinson, Viviane Mimaud, and Gilles Berdeaux. Evaluation of non-medical costs associated with visual impairment in four European countries: France, Italy, Germany and the UK. *Pharmacoeconomics*, 24(2):193–205, 2006.

[58] Daniel T. Larose. *Data Mining Methods and Models*. Wiley-IEEE Press, 2006.

[59] Jung Yeop Lee and Sang Joon Lee. Murray's law and the bifurcation angle in the arterial micro-circulation system and their application to the design of microfluidics. *Microfluidics and Nanofluidics*, 8(1):85–95, 2009.

[60] Huiyi Li, Wynne Hsu, Mong Li Lee, and Hongyir Wang. A piecewise Gaussian model for profiling and differentiating retinal vessels. In *Proceedings of the International Conference on Image Processing 2003*, volume 1, pages 1069–72, September 2003.

[61] Qiang Li, Hitetaka Arimura, and Kunio Doi. Selective enhancement filters for lung nodules, intracranial aneurysms, and breast microcalcifications. *International Congress Series*, 1268(0):929–934, 2004. Proceedings of the 18th International Congress and Exhibition Computer Assisted Radiology and Surgery CARS.

[62] Qiang Li, S. Sone, and Kunio Doi. Selective enhancement filters for nodules, vessels, and airway walls in two- and three-dimensional CT scans. *Medical Physics*, 30(8):2040–2051, 2003.

[63] Qin Li, Jane You, and David Zhang. Vessel segmentation and width estimation in retinal images using multiscale production of matched filter responses. *Expert Systems with Applications*, 39(9):7600–7610, 2012.

[64] Tony Lindeberg. Scale-space for discrete signals. *IEEE Transactions on Pattern Analysis and Machine Intelligence*, 12(3):234–254, 1990.

[65] Tony Lindeberg. On scale selection for differential operators. In Kjell Arild Hgøda, Bjørn Braathen, and Karsten Heia, editors, *Proceedings of the 8th Scandinavian Conference on Image Analysis*, pages 857–866, Tromsø, Norway, 1993. NOBIM.

[66] Tony Lindeberg. *Scale-Space Theory in Computer Vision*. Kluwer Academic Publishers, Stockholm, Sweden, 1994.

[67] Tony Lindeberg. Edge detection and ridge detection with automatic scale selection. In *Proceedings of the IEEE Computer Society Conference on Computer Vision and Pattern Recognition 1996*, pages 465–470, San Francisco, CA, USA, 1996. IEEE Computer Society Press.

[68] Tony Lindeberg. Linear spatio-temporal scale-space. In Bart M. T. Haar Romeny, Luc Florack, Jan Koenderink, and Max Viergever, editors, *Proceedings of the 1st International Conference on Scale-Space Theory in Computer Vision*, volume 1252, pages 113–127, Utrecht, The Netherlands, 1997. Springer Berlin Heidelberg.

[69] Tony Lindeberg. Edge detection and ridge detection with automatic scale selection. *International Journal of Computer Vision*, 30(2):117–156, 1998.

[70] Tony Lindeberg and Bart. M. T. Haar Romeny. Linear scale-space: (i) basic theory and (ii) early visual operations. In Bart. M. T. Haar Romeny, editor, *Geometry-Driven Diffusion in Computer Vision*, volume 1 of *Computational Imaging and Vision*, pages 1–77. Kluwer Academic Publishers, Dordrecht, The Netherlands, 1994.

[71] C. J. Longland. The collateral circulation of the limb. *Annals of The Royal College of Surgeons of England*, 13(3):161–176, 1953.

[72] Cristian Lorenz, Ingwer C. Carlsen, Thorsten M. Buzug, Carola Fassnacht, and Jürgen Weese. A multi-scale line filter with automatic scale selection based on

the hessian matrix for medical image segmentation. In Bart M. T. Haar Romeny, Luc Florack, Jan Koenderink, and Max Viergever, editors, *Proceedings of the 1st International Conference on Scale-Space Theory in Computer Vision*, volume 1252, pages 152–163, Utrecht, The Netherlands, 1997. Springer Berlin Heidelberg.

[73] Cristian Lorenz, Ingwer C. Carlsen, Thorsten M. Buzug, Carola Fassnacht, and Jürgen Weese. Multi-scale line segmentation with automatic estimation of width, contrast and tangential direction in 2D and 3D medical images. In Jocelyne Troccaz, Eric Grimson, and Ralph Mösges, editors, *Proceedings of the 1st Joint Conference on Computer Vision, Virtual Reality and Robotics in Medicine and Medical Robotics and Computer-Assisted Surgery*, volume 1205, pages 233–242, Grenoble, France, 1997. Springer Berlin Heidelberg.

[74] Ramon Luengo-Fernandez, Jose Leal, Alastair Gray, Sophie Petersen, and Mike Rayner. Cost of cardiovascular diseases in the United Kingdom. *Heart*, 92(10):1384–1389, 2006.

[75] Carmen Alina Lupaşcu, Domenico Tegolo, and Emanuele Trucco. Accurate estimation of retinal vessel width using bagged decision trees and an extended multiresolution hermite model. *Medical Image Analysis*, 17(8):1164–1180, 2013.

[76] YingLiang Ma, Andy P. King, Nicolas Gogin, C. Aldo Rinaldi, Jaswinder Gill, Reza Razavi, and Kawal S. Rhode. Real-time respiratory motion correction for cardiac electrophysiology procedures using image-based coronary sinus catheter tracking. *Medical Image Computing and Computer-Assisted Intervention–MICCAI 2010*, 13(1):391–399, 2010.

[77] Vijay Mahadevan, Harihar Narasimha-Iyer, Badrinath Roysam, and Howard L. Tanenbaum. Robust model-based vasculature detection in noisy biomedical images. *IEEE Transactions on Information Technology in Biomedicine*, 8(3):360–376, 2004.

[78] Peter Meer, Doron Mintz, Azriel Rosenfeld, and Dong Yoon Kim. Robust regression methods for computer vision: A review. *International Journal of Computer Vision*, 6(1):59–70, April 1991.

[79] Isaac Chesar Michaelson and David Benezra. *Textbook of the Fundus of the Eye*. Churchill Livingstone, 1980.

[80] Darwin Minassian and Angela Reidy. Future sight loss UK 2: An epidemiological and economic model for sight loss in the decade 2010–2020. Technical report, Royal National Institute of Blind People, July 2009.

[81] National Institute for Health and Clinical Excellence. *Prevention of Cardiovascular Disease: Costing Report*. Department of Health, London, UK, 2010.

[82] Reza Nekovei and Ying Sun. Back-propagation network and its configuration for blood vessel detection in angiograms. *IEEE Transactions on Neural Networks*, 6(1):64–72, January 1995.

[83] Thanh T. Nguyen and Tien Y. Wong. Retinal vascular manifestations of metabolic disorders. *Trends in Endocrinology and Metabolism*, 17(7):262–268, September 2006.

[84] Meindert Niemeijer, Joes J. Staal, Bram van Ginneken, Marco Loog, and Michael D. Abràmoff. Comparative study of retinal vessel segmentation methods on a new publicly available database. In J. Michael Fitzpatrick and Milan Sonka, editors, *Medical Imaging*, volume 5370, pages 648–656. SPIE, 2004.

[85] Maciej M. Orkisz, Christine Bresson, Isabelle E. Magnin, Olivier Champin, and Philippe C. Douek. Improved vessel visualization in MR angiography by nonlinear anisotropic filtering. *Magnetic Resonance in Medicine*, 37(6):914–919, 1997.

[86] Alireza Osareh, Majid Mirmehdi, Barry Thomas, and Richard Markham. Comparison of colour spaces for optic disc localisation in retinal images. In *Proceedings of the 16th International Conference on Pattern Recognition*, volume 1, pages 743–746, 2002.

[87] Nobuyuki Otsu. A threshold selection method from gray-level histograms. *IEEE Transactions on Systems, Man and Cybernetics*, 9(1):62–66, January 1979.

[88] Christopher G. Owen, Zakariya Jarrar, Richard Wormald, Derek G. Cook, Astrid E. Fletcher, and Alicja R. Rudnicka. The estimated prevalence and incidence of late stage age related macular degeneration in the UK. *British Journal of Ophthalmology*, 96(5):752–756, May 2012.

[89] Sarah L. Owens. Indocyanine green angiography. *British Journal of Ophthalmology*, 80(3):263–266, March 1996.

[90] Niall Patton, Tariq Aslam, Thomas Macgillivray, Alison Pattie, Ian J. Deary, and Baljean Dhillon. Retinal vascular image analysis as a potential screening tool for cerebrovascular disease: a rationale based on homology between cerebral and retinal microvasculatures. *Journal of Anatomy*, 206(4):319–348, April 2005.

[91] John M. S. Pearce. The ophthalmoscope: Helmholtz's Augenspiegel. *European Neurology*, 61(4):244–249, 2009.

[92] Edward Sylvester Perkins, Peter J. Hansell, and Ronald J. Marsh. *An Atlas of Diseases of the Eye*. Churchill Livingstone, 1986.

[93] Oleg Pomerantzeff, Robert H. Webb, and Francois C. Delori. Image formation in fundus cameras. *Investigative Ophthalmology and Visual Science*, 18(6):630–637, June 1979.

[94] Xiaoning N. Qian, Matthew P. Brennan, Donald P. Dione, Wawrzyniec L. Dobrucki, Marcel P. Jackowski, Christopher K. Breuer, Albert J. Sinusas, and Xenophon Papademetris. A non-parametric vessel detection method for complex vascular structures. *Medical Image Analysis*, 13(1):49–61, 2009.

[95] Javad Rahebi and Fırat Hardalaç. Retinal blood vessel segmentation with neural network by using gray-level co-occurrence matrix-based features. *Journal of Medical Systems*, 38(8):85, August 2014.

[96] Klaus Rank, Markus Lendl, and Rolf Unbehauen. Estimation of image noise variance. *IEE Proceedings - Vision, Image and Signal Processing*, 146(2):80–84, August 1999.

[97] Elisa Ricci and Renzo Perfetti. Retinal blood vessel segmentation using line operators and support vector classification. *IEEE Transactions on Medical Imaging*, 26(10):1357–1365, October 2007.

[98] Ralf Ritter. *Arteriogenesis*, volume 17, chapter Collateral Circulation in Clinical Practice, pages 353–358. Springer US, Boston, MA, USA, 2004.

[99] Nicola Roper, Sunni R. Patel, and Clare O'Donnell. Signs of stroke in the retina. *Optometry in Practice*, 13(1):9–18, 2012.

[100] Peter J. Rousseeuw. Least median of squares regression. *Journal of the American statistical association*, 79(388):871–880, 1984.

[101] Sohini Roychowdhury, Dara D. Koozekanani, and Keshab K. Parhi. Iterative vessel segmentation of fundus images. *IEEE Transactions on Biomedical Engineering*, 62(7):1738–1749, July 2015.

[102] Patrick J. Saine. Focusing the fundus camera: a clinical approach. *Journal of Ophthalmic Photography*, 14(1):7–24, 1992.

[103] Patrick J. Saine and Marshall E. Tyler. *Ophthalmic Photography: Retinal Photography, Angiography, and Electronic Imaging*. Butterworth-Heinemann, second edition, 2002.

[104] Sameh A. Salem, Nancy M. Salem, and Asoke K. Nandi. Segmentation of retinal blood vessels using a novel clustering algorithm (RACAL) with a partial supervision strategy. *Medical and Biological Engineering and Computing*, 45(3):261–273, 2007.

[105] Yoshinobu Sato, Takahiro Araki, Masayuki Hanayama, Hiroaki Naito, and Shinichi Tamura. A viewpoint determination system for stenosis diagnosis and quantification in coronary angiographic image acquisition. *IEEE Transactions on Medical Imaging*, 17:121–137, 1998.

[106] Yoshinobu Sato, Shin Nakajima, Hideki Atsumi, Thomas Koller, Guido Gerig, Shigeyuki Yoshida, and Ron Kikinis. 3D multi-scale line filter for segmentation and visualization of curvilinear structures in medical images. In Jocelyne Troccaz, Eric Grimson, and Ralph Mösges, editors, *Proceedings of the 1st Joint Conference on Computer Vision, Virtual Reality and Robotics in Medicine and Medical Robotics and Computer-Assisted Surgery*, volume 1205, pages 213–222, Grenoble, France, 1997. Springer Berlin Heidelberg.

[107] Abraham Savitzky and Marcel J. E. Golay. Smoothing and differentiation of data by simplified least squares procedures. *Analytical Chemistry*, 36(8):1627–1639, 1964.

[108] Linda G. Shapiro and George Stockman. *Computer Vision*. Prentice Hall PTR, Upper Saddle River, NJ, USA, first edition, 2001.

[109] Daniel Paredes Soto, Philip Chan, and Peter Rockett. Performance comparison of low-level vessel detection algorithms for segmentation of X-ray angiograms. In Xianghua Xie, editor, *Proceedings of the 16th Conference on Medical Image Understanding and Analysis*, pages 173–178, Swansea, United Kingdom, 2012.

[110] Joes Staal, Michael D. Abràmoff, Meindert Niemeijer, Max A. Viergever, and Bram van Ginneken. Ridge-based vessel segmentation in color images of the retina. *IEEE Transactions on Medical Imaging*, 23(4):501–509, April 2004.

[111] James V. Stone. *Bayes' Rule: A Tutorial Introduction to Bayesian Analysis*. Sebtel Press, first edition, 2013.

[112] Phongsuphap Sukanya, Ryo Takamatsu, and Makoto Sato. A new operator for image structure analysis. In P. Delogne, editor, *Proceedings of the International Conference on Image Processing 1996*, volume 3, pages 615–618, Lausanne, Switzerland, 1996. IEEE.

[113] Phan Tran Ho Truc, Mohammad Aurangzeb U. Khan, Young-Koo Lee, Sungyoung Lee, and Tae-Seong Kim. Vessel enhancement filter using directional filter bank. *Computer Vision and Image Understanding*, 113(1):101–112, 2009.

[114] L. Wang, A. Bhalerao, and R. Wilson. Analysis of retinal vasculature using a multiresolution hermite model. *IEEE Transactions on Medical Imaging*, 26(2):137–152, February 2007.

[115] Daniel Welfer, Jacob Scharcanski, Cleyson M. Kitamura, Melissa M. Dal Pizzol, Laura W.B. Ludwig, and Diane Ruschel Marinho. Segmentation of the optic disk in color eye fundus images using an adaptive morphological approach. *Computers in Biology and Medicine*, 40(2):124–137, 2010.

[116] Onno Wink, Wiro J. Niessen, and Max A. Viergever. Multiscale vessel tracking. *IEEE Transactions on Medical Imaging*, 23(1):130–133, 2004.

[117] Maciej Wojtkowski, Vivek Srinivasan, James G. Fujimoto, Tony Ko, Joel S. Schuman, Andrzej Kowalczyk, and Jay S. Duker. Three-dimensional retinal imaging with high-speed ultrahigh-resolution optical coherence tomography. *Ophthalmology*, 112(10):1734–1746, October 2005.

[118] Tien Yin Wong and Paul Mitchell. The eye in hypertension. *Lancet*, 369(9559):425–435, February 2007.

[119] Lili Xu and Shuqian Luo. A novel method for blood vessel detection from retinal images. *BioMedical Engineering OnLine*, 9(1):14:1–10, 2010.

[120] Loren G. Yamamoto. Using JPEG image compression to facilitate telemedicine. *The American Journal of Emergency Medicine*, 13(1):55–57, 1995.

[121] Yuan Yuan and Albert C. S. Chung. Multi-scale model-based vessel enhancement using local line integrals. In *Proceedings of the 30th Annual International Conference of the IEEE Engineering in Medicine and Biology Society*, pages 2225–2228, Vancouver, British Columbia, Canada, 2008. IEEE.

[122] Zhengyou Zhang. Parameter estimation techniques: A tutorial with application to conic fitting. *Image and Vision Computing*, 15(1):59–76, 1997.

[123] R. Eugene Zierler and David S. Sumner. Arterial physiology. In Jack L. Cronenwett and K. Wayne Johnston, editors, *Rutherford's Vascular Surgery*, volume 1, chapter 9, pages 131–149. Saunders, seventh edition, 2010.

[124] Alex P. Zijdenbos, Benoit M. Dawant, Richard A. Margolin, and Andrew C. Palmer. Morphometric analysis of white matter lesions in MR images: method

and validation. *IEEE Transactions on Medical Imaging*, 13(4):716–724, December 1994.

[125] Hooshiar Zolfagharnasab and Ahmad Reza Naghsh-Nilchi. Cauchy based matched filter for retinal vessels detection. *Journal of Medical Signals and Sensors*, 4(1):1–9, January 2014.